Structure and Cross Section Data of Neutron-Rich N~20 Nuclei Produced in Fragmentation and Few-Nucleon Knockout Reactions

by

Elena Rodriguez-Vieitez

B.S. (University of Santiago de Compostela, Spain) 1994
M.S. (University of Utah, USA) 1998

A dissertation submitted in partial satisfaction of the requirements for the degree of

Doctor of Philosophy

in

Engineering – Nuclear Engineering

in the

Graduate Division

of the

University of California, Berkeley

Committee in charge:

Professor Stanley G. Prussin, Chair
Professor Jasmina L. Vujic
Professor Joseph Cerny

Fall 2007

Structure and Cross Section Data of Neutron-Rich N~20 Nuclei
Produced in Fragmentation and Few-Nucleon Knockout Reactions

by Elena Rodriguez-Vieitez

Abstract

Structure and Cross Section Data of Neutron-Rich N~20 Nuclei
Produced in Fragmentation and Few-Nucleon Knockout Reactions

by

Elena Rodriguez-Vieitez

Doctor of Philosophy in Engineering – Nuclear Engineering

University of California, Berkeley

Professor Stanley G. Prussin, Chair

Neutron-rich nuclei in the "island of inversion" display ground-state deformation despite proximity to the N=20 conventional magic number. In this thesis, $^{28-30}$Ne were produced by few-nucleon knockout of ~90-MeV/A $^{30-32}$Mg and ^{29}Na beams originated by fragmentation of 140-MeV/A ^{48}Ca at the National Superconducting Cyclotron Laboratory. The low-lying $^{28-30}$Ne structures were determined through measurements of prompt single-γ and γ-γ coincidences by the Segmented Germanium Array (SeGA), where high transverse segmentation provided the Doppler correction necessary to achieve good energy resolution.

The $^{28-30}$Ne level schemes were compared with shell-model calculations: (a) OXBASH using the USD-A interaction, restricted to "sd-shell" 0p0h (0-particle-0-hole) "normal" configurations, and (b) a Monte-Carlo Shell-Model (MCSM) code using the SDPF-M interaction, including promotion of neutrons (2p2h "intruder" configurations) across a reduced N=20 gap. A dominance of intruder configurations is believed to explain ground-state deformation. New data on $^{28-30}$Ne excited states were used to test shell-model predictions at the transition to the island of inversion. MCSM with the SDPF-M

interaction provided good overall description of the data and improved predictive power compared with USD-A.

The ^{28}Ne structure consisted of a cascade of three consecutive transitions. The measured $4_1^+ \rightarrow 2_1^+$ 1707(7)-keV and $2_1^+ \rightarrow 0_1^+$ 1306(4)-keV γ rays confirmed literature data, and γ-γ coincidences for an observed 891(5)-keV (proposed $4_2^+ \rightarrow 4_1^+$) transition ruled out published data assigning $0_2^+ \rightarrow 2_1^+$ to this transition. While data conformed better to SDPF-M (predicting ~50-50% 0p0h-2p2h ground-state configuration), discrepancies exist: the low-lying 2.2-MeV 0_2^+ predicted by SDPF-M remains unobserved, and ^{28}Ne contains a new isolated 1127(4)-keV transition not explained by SDPF-M.

The $^{29\text{-}30}$Ne structures (~100% 2p2h ground-state configurations predicted by SDPF-M) showed significantly better fit to SDPF-M than USD-A. In ^{30}Ne, a low-energy $2_1^+ \rightarrow 0_1^+$ 792(4)-keV transition confirmed literature data, suggesting large deformation, and a new $4_1^+ \rightarrow 2_1^+$ 1443(11)-keV transition provided the first observed 4_1^+ state in the island of inversion.

Measured few-nucleon knockout cross-sections of 0.2-14 mb agree with literature. These data show experimental-to-theoretical one-proton knockout cross-section ratios of ~0.5-0.7. An observed ~0.25 experimental-to-theoretical cross-section ratio in two-proton knockout was lower than ~0.5 reported in literature. We attribute this reduction to differences in the neutron wave functions between initial and final nuclei.

Professor Stanley G. Prussin
Dissertation Committee Chair

To my whole family who has supported me all along,

and especially to my parents, Juan Bautista and Nieves

Table of Contents

List of Figures

List of Tables

Acknowledgements

I would like to express my sincere gratitude to Professor Stan Prussin, who guided this thesis, for his continuous supervision and discussion of ideas, as well as his personal advice during my graduate studies. I am in gratitude to Professors Joe Cerny and Jasmina Vujic for agreeing to be in my committee, reading this manuscript, and all their helpful suggestions.

This thesis would have been impossible without the lead and continuous support of Dr. Paul Fallon, my research supervisor at the Nuclear Structure Group, Lawrence Berkeley National Lab (LBNL), who guided all aspects of this work including the experiment proposals at the National Superconducting Cyclotron Lab (NSCL) at Michigan State University (MSU), coordination with MSU scientists, data analysis and interpretation, and helping with all my writing. I am indebted to the uncommon opportunity of learning from first-rate scientists at the Nuclear Structure Group, which has helped me develop as a scientist and my future career. I am also grateful for essential theoretical and data analysis and interpretation from Augusto Macchiavelli, and for discussion of ideas with Mathis Wiedeking, I-Yang Lee, and Rod Clark, who assisted this work with many insightful comments. I am indebted to Mathis' collaboration during experimental runs, and for his help with data analysis, shell-model calculations, calibrations and discussion of ideas. Thanks to Mario Cromaz for invaluable help in setting up the data acquisition software at the lab among many other computer-related questions. This research also benefited from numerous group discussions including Frank

Stephens, Marie Deleplanque, David Ward, Martina Descovich, and John Pavan. I especially appreciate the help of David Ward for his patience during my beginnings in gamma-ray spectroscopy analysis.

The experiments (E03053 and E05122) in this thesis were carried out at the NSCL (MSU), which is funded by the National Science Foundation under cooperative agreement PHY06-06007. I especially thank Thomas Glasmacher and Alexandra Gade for their guidance regarding the experimental planning and data interpretation, and all the incredibly hard-working and talented scientists who collaborated during beam time and who offered advice and help in the subsequent months of data analysis, including Daniel Bazin, Chris Campbell, Jon Cook, Dan C. Dinca, Wil Mueller, Ken Yoneda, Dirk Weisshaar, and Russ Terry. I also thank Mauricio Portillo for help with LISE calculations, Ron Fox for support using SpecTcl, and Raman Anantaraman for coordinating our collaboration, as well as the remaining operations staff at the MSU cyclotron. Shell-model calculations were provided by Takaharu Otsuka and Yutaka Utsuno, and reaction-model calculations by Jeff Tostevin and Alex Brown.

During the course of my studies, I also had the opportunity to participate in several experiments at the 88"-cyclotron (LBNL), supported by the U.S. Department of Energy under contract number DE-AC02-05CH11231. I thank all the research scientists and staff at the cyclotron for their warm and supportive collaboration, and especially to Eddie Browne for his helpful advice and friendship during the last part of my thesis writing.

The completion of this thesis was greatly made possible thanks to the support from my friends in Berkeley and the International House, especially Edith García, Ilse Ruiz, Jesús Solís, Lionel Prost, Behrang Mohit and Karel Pravda, as well as all the graduate

students in Prof. Prussin's group who heard my talks many times over and provided valuable feedback and advice. I appreciate Lisa Zemelman's assistance with my numerous questions and paperwork at the Nuclear Engineering department. I am also indebted to the support from my long-time friends María Suarez and Pilar Sanchez.

I greatly appreciate Anders Hedman who has inspired my life and encouraged me, and for his much patience and love.

Finally I am indebted to my family in Spain, to whom I felt very close all these years. I would like to especially thank my parents Juan Bautista and Nieves, my brother Juan Bautista, and my sisters Nieves and Raquel, and the rest of my family: Andrés, Emilia, Isabel, Toño, Emiliana, Pepe, Inés, Mucha, and all my cousins. I also had the invariable support of my grandmother Nieves Golpe and of María and Lola Golpe, who cared so much about our family and they surely are proud of my accomplishment, as well as my late grandparents Arturo Vieitez, Juan Bautista Rodriguez and Dorinda Casal. In the difficult moments, it was the unconditional support of my family which allowed me to continue, and to them this thesis is dedicated.

Elena Rodriguez-Vieitez

Berkeley, California

November 2007

Chapter 1

Physics Motivation and Objectives

1.1 The Structure of Atomic Nuclei

The nucleus is located at the center of the atom occupying only ~10^{-15} of its volume but concentrating virtually all of its mass (more than 99.9%) over a length scale on the order of one to ten fermi (1 fm = 10^{-15} m). Nuclei can be regarded as non-relativistic (NR) quantum systems of neutrons and protons (nucleons) interacting by three types of forces: strong, electromagnetic, and weak. The dominant interaction is the short-range strong nucleon-nucleon force, governed by the NR Schrödinger equation. The intensity of the strong force is to a good approximation independent of the types of nucleons involved (neutrons, protons, or neutron-proton pairs).

The chart of nuclei (Fig. 1.1) contains the combinations of numbers of protons (Z) and neutrons (N) expected to exist as bound entities as predicted by current nuclear structure models. For Z below ~92, while the strong nuclear force is responsible for the binding of nuclei, when there is an excess of either neutrons (N) or protons (Z) the weak nuclear force causes nuclear decay by β emission (that is, electron or positron emission) or electron capture. Only around 300 nuclear species in the chart are stable against β decay or electron capture, and can be found in nature. Nuclei in this "valley of stability" contain approximately equal amounts of N and Z for mass number $A \leq 40$ (where A = N + Z); for increasingly heavier nuclei, an increasing excess of neutrons is necessary to

overcome the Coulomb repulsion between the protons. It is estimated that there are around 7,000 unstable nuclei, of which more than half have not yet been studied experimentally [Bro01].

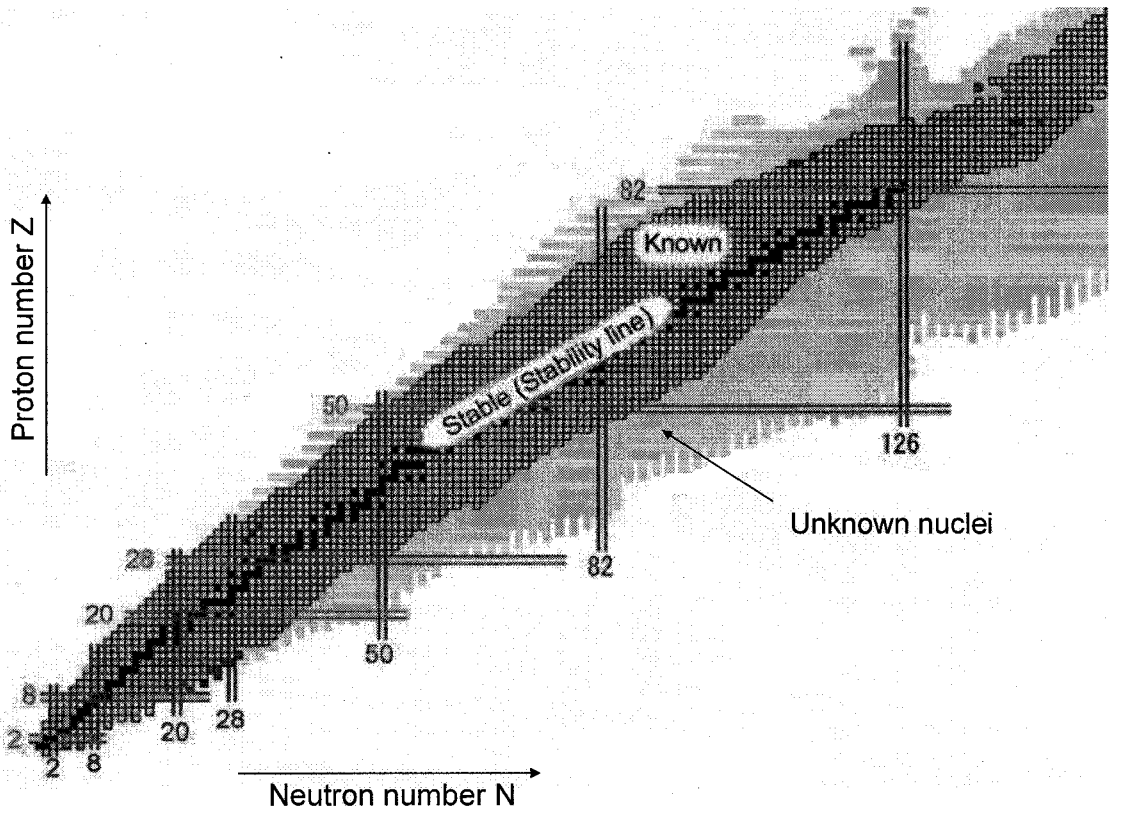

Figure 1.1 **The chart of nuclei.** There are around 300 stable nuclei (black squares) forming the "stability line". Unstable nuclei in dark gray areas around the stability line have been studied experimentally. Nuclei in light grey areas remain to be experimentally investigated, adapted from [Uts07].

Since the discovery of the nucleus in 1911 by Rutherford [Rut11], significant efforts have been directed at studying its structure. It was soon observed that the separation energies of a neutron or a proton, S(n) or S(p), did not vary smoothly with changes in N and Z, respectively; instead, they showed dips near certain numbers, which were termed "magic numbers". Mayer and Jensen were the first to propose the "shell model" of the nucleus [May49, May55] where nucleons move independently of each other under the

influence of a common average or mean field. Mayer *et al.* also proposed the addition of a spin-orbit term in the potential (by similitude with the electronic shell structure in atoms) [May49, Hax49] that takes into account a strong interaction between the orbital angular momentum and the spin of each moving nucleon. With the addition of the spin-orbit term the nuclear shell model became especially successful as it was able to correctly predict the location of the experimentally-known magic numbers, at 2, 8, 20, 28, 50, 82, etc. The spin-orbit effect in nuclei turned out to be much stronger than that in atoms. Even though many nuclear models have been developed since, the shell model has remained one of the most successful and is a standard against which other models are tested.

1.2 Exotic Neutron-Rich Nuclei and the "Island of Inversion"

In recent years the focus of experimental nuclear structure research has shifted away from the well-known valley of stability and into lesser-known regions towards the proton and neutron drip lines (where the proton and neutron separation energies become zero, respectively). The term "exotic nuclei" generally refers to nuclei at extreme conditions such as high angular momentum, high temperature, or (e.g., in this work) to the case of extreme proton-to-neutron ratios. It has been a common practice in nuclear structure research to study nuclei under different types of extreme conditions and it has often been the case that new types of nuclear behavior are observed in such studies: as an example, rotational deformations under high angular momentum. It is thus reasonable to also expect new phenomena at extreme values of the proton-to-neutron ratio.

Exotic neutron-rich nuclei (the subject of this study) are interesting for a variety of reasons. For example, even though they are not naturally present on Earth, they existed at earlier times during the evolution of the universe and are constantly produced and consumed in the life cycle of stars (stellar nucleosynthesis). A knowledge of the structure and reaction probabilities of these nuclei is needed to improve theoretical models in cosmology and astrophysics, and therefore to understand the synthesis of matter in the universe. Data on exotic nuclei are also useful to improve theoretical models of nuclear reactions that will ultimately contribute to a range of applications. Some engineering applications include advanced nuclear reactor designs that will be more efficient and proliferation-resistant, waste transmutation (a process to convert nuclear waste into a stable or less radioactive form), detection of radioactive materials for security purposes, or production of unstable isotopes of medical interest. As an example, nuclear waste transmutation generates a multitude of intermediate short-lived neutron-rich isotopes and modeling this process would greatly benefit from more accurate reaction data.

Until recently (~20 or 30 years ago) experimental nuclear physics facilities were designed to conduct nuclear reactions involving stable beams and targets only; as a result, it was not possible to produce and study very neutron-rich species. The study of exotic short-lived species has been facilitated by the operation of radioactive-beam facilities, such as the National Superconducting National Laboratory (NSCL) at Michigan State University (MSU), where we conducted our research, and other laboratories worldwide such as RIKEN (Japan), GANIL (France), GSI (Germany), etc.

From a nuclear structure point of view, neutron-rich nuclei provide new and valuable insights because until only recently, nuclear structure models were tested only against

data near stability. The recent experimental observation of new phenomena in neutron-rich nuclei (such as neutron skins and halos [Tan85, Han95]) suggests that the conventional nuclear models that worked well near stability cannot be easily extrapolated to regions with large proton-to-neutron asymmetries.

Both stable and exotic nuclei may display so-called collective effects, which are deviations from the independent-particle model predictions due to correlations (also called residual or effective interactions) between nucleons that are beyond the mean field. New collective phenomena such as the interplay of deformation, rotation and pairing in the presence of weak binding have been observed in neutron-rich nuclei [Yam04]. Neutron-rich nuclei have also been observed to display changes in the location of magic numbers with respect to the conventional shell model [War04, Jan05] and increased binding of nuclei at or near the drip lines. Recent experimental and theoretical investigations support the idea of a weakening of certain "conventional" magic numbers such as N = 20 [War90, Fuk92, Mot95] and N = 28 [Soh02], and possible emergence of new ones (N = 14, 16) [Oza00].

This thesis is focused on the study of a light neutron-rich region called the "island of inversion" [War90]. This region – believed to be centered around Z ~ 11 and N ~ 20 for neutron-rich isotopes of neon, sodium and magnesium (Fig. 1.2) – is characterized by nuclei with strongly deformed ground states despite their nucleon number being near the conventional N = 20 magic number. One of the first evidences of this anomalous behavior was the measurement of higher-than-expected binding energies in ^{31,32}Na [Thi75]. Different theoretical approaches have been directed to understanding the origin of these deformed ground states and the possible loss of magicity of N = 20.

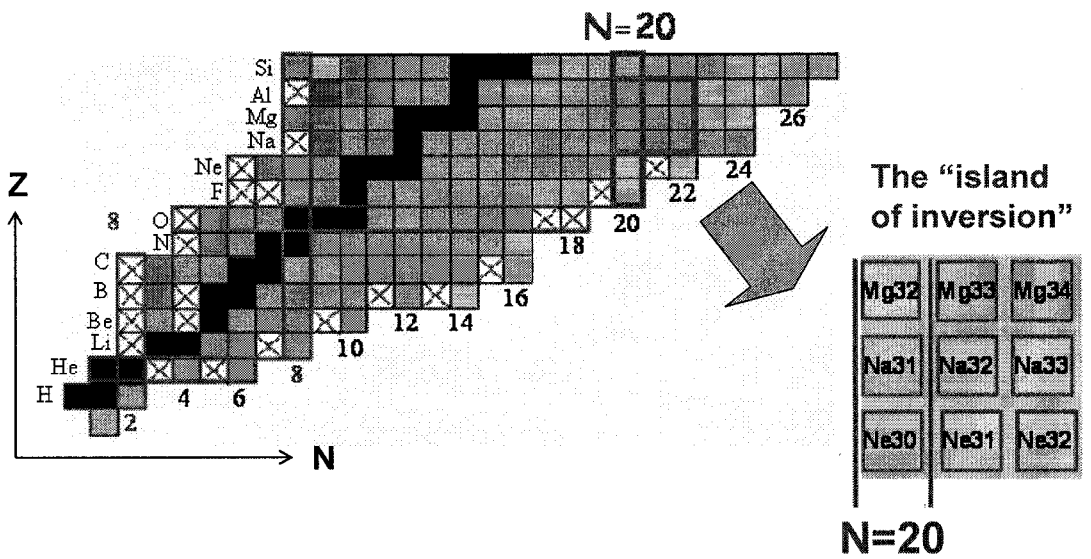

Figure 1.2 **The "island of inversion".** A region of light neutron-rich nuclei around N ~ 20 and A ~ 30. The horizontal axis is the neutron number N and the vertical axis the proton number Z. The crossed squares correspond to nuclei that are unbound, adapted from [Uts07].

The experimental nuclear structure data in this thesis were mainly interpreted within the framework of shell-model calculations based on two types of residual or effective interactions: USD-A [Wil84, Bro07a] and SDPF-M [Uts99, Uts05, Uts07] (Chapter 2). The shell-model calculation using the SDPF-M interaction is a Monte Carlo Shell Model (MCSM) code. These two types of shell-model calculations differ mainly in their model spaces or number of single-particle orbitals in which valence neutrons (those outside of a ^{16}O inert core) are allowed to reside: the sd shell ($1d_{5/2}$, $2s_{1/2}$ and $1d_{3/2}$) in the case of the USD-A interaction, and the sd shell plus two orbits of the pf shell ($1f_{7/2}$ and $2p_{3/2}$) in the SDPF-M interaction (Fig. 1.3).

The effective interaction used in the SDPF-M calculations is fundamentally based on a strong proton-neutron component that affects the valence protons in the $1d_{5/2}$ and the valence neutrons in the $1d_{3/2}$ (Fig. 1.3), as will be addressed in Chapter 2.

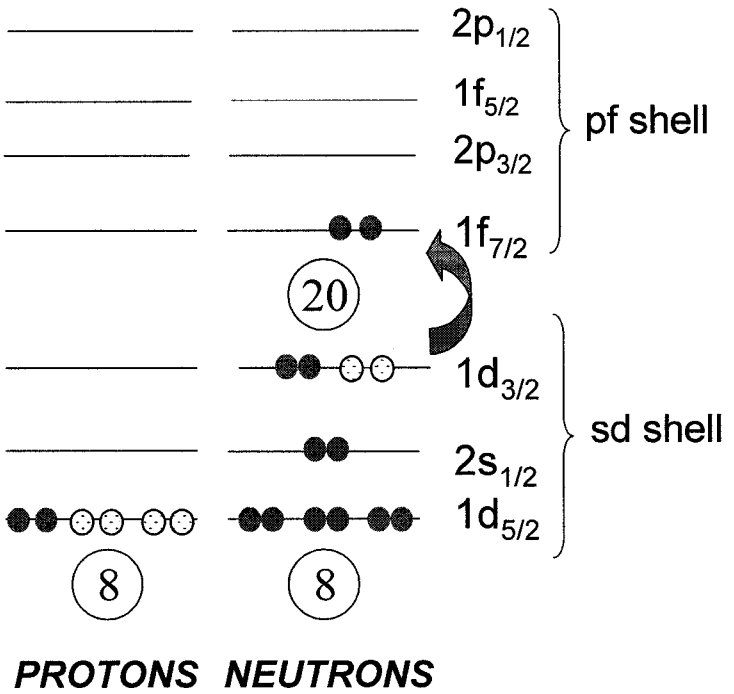

Figure 1.3 Schematic diagram of independent-particle orbitals occupied by protons and neutrons in ^{30}Ne, representing a two-particle – two-hole (2p2h) excitation across the N = 20 shell gap.

The basic assumption is that, as protons are removed from the proton (π) $1d_{5/2}$ orbital in the N = 20 neutron-rich isotones when moving from ^{34}Si (Z = 14) to ^{30}Ne (Z = 10), this proton-neutron force gets reduced, resulting in an energy increase of the neutron (ν) $1d_{3/2}$ level, and therefore a reduction in the N = 20 shell gap (with a simultaneous increase in the N = 16 gap). An additional attractive interaction between the $1d_{5/2}$ protons and the $1f_{7/2}$ neutrons is thought to contribute to the weakening of the N = 20 shell gap. The reduction in the N = 20 gap promotes increased population of the pf shell by pairs of neutrons (excited by pair scattering). The SDPF-M calculations predict that in the "island of inversion" region nuclei exhibit a shape coexistence phenomenon where "normal" spherical configurations, also called 0p0h (0-particle – 0-hole), in which nucleons reside

in the sd shell only, coexist with "intruder" deformed configurations in which a pair of neutrons is promoted across the N = 20 shell gap into the pf shell (2p2h configurations). A deformed ground state occurs when the energy of the "intruder" configuration becomes lower than that of the "normal" configuration. The reduction in the N = 20 shell gap is thus one of the factors causing the observed intruder-dominated deformed ground states in the "island of inversion" region.

1.3 Thesis Objectives and Approach

This thesis concerns the light neutron-rich $^{28\text{-}30}$Ne isotopes, which are located near or within the island of inversion. The objective of this research is to analyze and interpret new structure data in $^{28\text{-}30}$Ne with the ultimate goal of understanding the structural changes taking place at the transition to the island of inversion. According to shell-model calculations, the transition is thought to be caused by increasingly larger "intruder" configurations in the ground state, which is manifested by a shape evolution from spherical to different degrees of deformation in the ground state.

The experimental structure data will be compared with USD-A and SDPF-M shell-model calculations (Chapter 2) and the cross section data to reaction theory predictions (Chapter 3).

The $^{28\text{-}30}$Ne neutron-rich nuclei were produced in one- and two-proton knockout reactions, a direct-type mechanism [Han03] which – combined with in-beam γ-ray spectroscopy data – provides information on the single-particle structure of these nuclei.

Alternative experimental approaches to study neutron-rich nuclei, as reported in the literature, include intermediate-energy Coulomb excitation [Gla98] and inelastic

scattering [Yan03]; these mechanisms are able to populate one or at most two excited nuclear states, although they can be used to measure the transition probability to the first excited state and therefore provide information on the degree of collectivity (Chapter 2) of these exotic nuclei. Fragmentation and knockout reactions, on the other hand, are known to populate a variety of excited states [Mor98, Pod06]. A number of fragmentation/knockout experiments to study the island of inversion have been carried out during the last few decades, using a variety of scintillator and germanium γ-ray detectors. In our study, a high-resolution segmented germanium detector array (SeGA) [Mue01] provided high-quality spectroscopic data, which allowed the identification of previously unknown γ-ray transitions.

The predicted modified level ordering caused by the monopole interaction and the presence of intruder states is expected to give rise to different modes of nuclear collective excitations (rotational and/or vibrational). While the evidence for intruder ground states is well established, more research is needed to clarify where the transition from normal to deformed intruder ground states occurs, and what the nature of the observed collectivity is.

Mapping the border to the island of inversion and determining the intruder content of the ground and excited nuclear states constitute an important test of modern shell-model codes and nucleon-nucleon interactions far from stability, and can be used to improve the predictive power of shell-model calculations in the neutron-rich region.

Chapter 2

Nuclear Structure Theory

A variety of nuclear structure models has been proposed and developed since the 1930s. These models fundamentally differ in their conception of the nucleus, pictured between two extremes of independent-particle and collective behavior. In the first extreme, nucleons are treated as moving independently of each other under an average field generated by the nucleus as a whole. Two of the independent-particle models are the spherical shell model [May55] where the field is spherically symmetric (Section 2.2), and the Nilsson model, first proposed in 1955 [Cas00a (Ch. 8)], where the field is non-spherical or deformed (Section 2.4). Collective models (Section 2.3) treat the nucleus as a macroscopic entity and do not describe specific motions of individual nucleons. Section 2.1 defines a number of nuclear properties that will be referred to throughout the chapter.

The first nuclear model proposed, by Niels Bohr in 1935 [Boh36], was the collective (mainly classical) liquid-drop model (LDM). The semi-empirical mass formula of Weizsäcker, derived from the LDM, expresses the nuclear mass as a sum of several classical terms (volume, surface, Coulomb, etc.) plus two terms taking into account quantum-mechanical effects: the pairing and the asymmetry terms. In particular, the pairing term contributes to an increased nuclear binding when the nucleus contains a greater number of pairs of nucleons of the same type; the asymmetry term provides a decreased nuclear binding when there is a large excess of either protons or neutrons.

Additional work based on the LDM led to a more sophisticated collective model generally referred to as the "collective model of A. Bohr and B. R. Mottelson" and developed in the 1950s [Boh75], where the excited states of the liquid-drop nucleus are mathematically described as vibrations and rotations of the nucleus as a whole [Cas00a (Ch. 6)].

A given nucleus can be described simultaneously in both independent-particle and collective frameworks, where one or the other limiting description dominates the nuclear behavior depending on properties such as the total mass, the numbers of protons and neutrons, the total angular momentum (also called "spin"), and the excitation energy, among others.

2.1 Nuclear Properties

2.1.1 Electromagnetic Moments

Since nuclei contain distributions of electric charges and currents, they give rise to electric and magnetic fields, which can be mathematically expanded in terms of electric and magnetic multipoles. A given nuclear state is characterized by specific values of the electric and magnetic multipole moments. The dipole, quadrupole, octupole, etc., multipole moments correspond to order L = 1, 2, 3, etc., respectively. In the experimental γ-ray energy range of interest (< 3 MeV) the only significant moments are the electric quadrupole (E2) moment, which is associated with the $1/r^4$ term of the electric field, and the magnetic dipole (M1) moment, which corresponds to the $1/r^3$ term of the magnetic field [Kra88].

Each electromagnetic multipole moment has a parity relative to the emitting center; if, when changing $\mathbf{r} \rightarrow \mathbf{-r}$, the sign of the multipole operator is the same (opposite), then the parity is positive (negative). The parity of electric moments is $(-1)^L$ and that of the magnetic moments is $(-1)^{L+1}$ so that the E2 (L = 2) and M1 (L = 1) moments both have positive parity.

The magnetic dipole moment $\boldsymbol{\mu}$ in a classical picture is generated by the circular motion of a charged particle of mass m with an angular momentum $\boldsymbol{\ell} = \mathbf{r} \times m\mathbf{v}$, where $\mathbf{v}$ is the linear velocity tangent to the loop. The magnitude of $\boldsymbol{\mu}$ is the product of the current intensity times the area described by the circular motion and its direction is the same as $\boldsymbol{\ell}$ so that, classically, $\boldsymbol{\mu}$ is calculated to be $(e/2m)\,\boldsymbol{\ell}$.

The corresponding quantum-mechanical expression for $\boldsymbol{\mu}$ is related to the total (orbital plus intrinsic spin) angular momentum of the nucleus, **I**, also called "spin" of the nucleus. The quantum-mechanical expression for the magnitude of $\boldsymbol{\mu}$ (μ) is formally obtained by calculating the expectation value of the z component of the magnetic dipole operator $\boldsymbol{\mu}$, evaluated for the nuclear substate in which the projection of **I** is maximum, that is, for M = +I, where I is the nuclear spin quantum number. In the nucleus the magnetic dipole moment μ arises from both the orbiting charged particles (protons) and the intrinsic spins of the nucleons, which generate their own intrinsic magnetic field. The magnetic dipole moment of the nucleus is given by [Cas90]:

$$\mu = g \frac{e\hbar}{2m_p} I = g\, I\, \mu_N \qquad (2.1)$$

where g is the gyromagnetic factor, which is 2 for elementary particles such as the electron but which takes different values for nucleons and nuclei, and μ_N is the nuclear magneton equal to $e\hbar/2m_p$ where m_p is the mass of the proton.

The electric quadrupole moment (Q) is proportional to the deviation of a nuclear charge distribution from spherical symmetry. We assume the nucleus to be axially symmetric with respect to a body-fixed axis z. The electric quadrupole moment is obtained by evaluating the electric quadrupole operator $3z^2 - r^2 = r^2(3\cos^2\theta - 1)$ in a state in which the projection m_j of the total angular momentum j of the odd particle on the symmetry axis of the nucleus takes its maximum value, that is, $m_j = +j$. With these assumptions, the expectation value of Q of a nucleus containing Z charges is given by Eq. 2.2, where the integral is expressed as a function of the nuclear volume element $d\upsilon$ (expressed in spherical coordinates r, θ, and ϕ) and the wave functions ψ_i of the protons:

$$< Q > = \sum_{i=1}^{Z} \int_{\text{nucleus}} \psi_i^* r^2 (3\cos^2\theta - 1)\psi_i d\upsilon \qquad (2.2)$$

Because of symmetry properties of the nuclear wave functions, it is not possible to observe Q values for states with spin $I < 1$. For example, the ground states of even-even nuclei can be deformed but their Q cannot be measured because their spin is 0^+.

Available experimental measurements of Q values across the nuclear chart, assuming that nuclei are axially symmetry about the z axis, show that: (1) Q values are small near magic numbers, and (2) the great majority of nuclei have positive Q values, that is, they are "prolate" (the charge distribution extends mainly along the z axis). Oblate nuclei ($Q < 0$) are those for which the charge distribution extends throughout the xy plane perpendicular to the z symmetry axis.

When Q is calculated in the reference frame where the nucleus is at rest, it is called the intrinsic quadrupole moment, Q_0, which is the value commonly tabulated in the literature.

2.1.2 Nuclear Excited States and Decay Transition Probabilities

An important property of nuclear excited states is their decay or transition probability T_{fi} (s^{-1}) from an initial state with total angular momentum I_i to a final state I_f. The decay most commonly proceeds by emission of electromagnetic radiation of multipole order L, i.e., by emission of a γ ray of total angular momentum L under the condition expressed in Eq. 2.3:

$$|I_i - I_f| \leq L_\gamma \leq I_i + I_f \tag{2.3}$$

Since the intrinsic spin of the photon is $1\hbar$, transitions from 0^+ to 0^+ states are forbidden to decay through single γ-ray emission (but can decay instead by internal conversion). Due to conservation of parity: $\pi_f\pi_\gamma = \pi_i$. The parity of transition of multipole order L is $\pi_E = (-1)^L$ for an electric transition, and $\pi_M = (-1)^{L+1}$ when the transition is of magnetic character.

The quantum-mechanical first-order perturbation theory provides a method to calculate the transition probability, T_{fi} (s^{-1}), given a knowledge of the initial and final state wave functions and a certain perturbation potential which causes the transition. In the electromagnetic decay of a nuclear state, the perturbation potential is given by the electric or magnetic multipole transition operator, $M_{\lambda L}$, where λ corresponds to either an electric (E) or magnetic (M) transition and L is the transition multipole order. The method is referred to as the Fermi's Golden Rule (Eq. 2.4). In Eq. 2.4, $M_{\lambda L}(i \rightarrow f)$ represents the expectation value of the $M_{\lambda L}$ transition operator evaluated between the initial (i) and final (f) states (Eq. 2.5):

$$T_{fi}(s^{-1}) = \frac{2\pi}{\hbar} \left| M_{\lambda L}(i \rightarrow f) \right|^2 \rho(E_f) \tag{2.4}$$

$$M_{\lambda L}(i \rightarrow f) = \int \psi_f^{*} \; M_{\lambda L} \; \psi_i \, d\upsilon \qquad (2.5)$$

In Eq. 2.4, $\rho(E_f)$ is the density of continuum states into which the photon can be emitted (in units of number of states per unit energy, i.e., MeV^{-1}); a larger density of final states leads to an increased transition probability. The factor $2\pi/\hbar$ has units of $MeV^{-1}s^{-1}$, and $|M_{\lambda L}(i \rightarrow f)|^2$ has units of MeV^2.

The multipole transition operator, $M_{\lambda L}$, is further related to the so-called "reduced transition probability" or "transition strength", $B(\lambda L)$, as expressed in Eq. 2.6:

$$B(\lambda L;\, I_i \rightarrow I_f) = \frac{1}{2I_i + 1} \; |< I_f \,\|\, M_{\lambda L} \,\|\, I_i >|^2 \qquad (2.6)$$

From the definition in Eq. 2.6 it is straightforward to obtain Eq. 2.7, which relates the $B(\lambda L)$ of the $I_i \rightarrow I_f$ transition to the $B(\lambda L)$ of the reversed one, $I_f \rightarrow I_i$:

$$B(\lambda L;\, I_f \rightarrow I_i) = \frac{2I_i + 1}{2I_f + 1} \, B(\lambda L;\, I_i \rightarrow I_f) \qquad (2.7)$$

Equation 2.8 [Boh75] is an expression relating the transition probability T_{fi} to its transition strength, $B(\lambda L)$, where λ labels an electric (E) or magnetic (M) transition, and L is the transition multipole order. In this research, where the γ-ray energies are below 3 MeV, the only significantly intense transitions are those of E2 or M1 character, with transition strength units of e^2fm^4 and μ_N^2, respectively. As explained in Chapter 6, we used calculated B(E2) and B(M1) values and experimental γ-ray transition energies, E_γ (in MeV), as well as assumed spin assignments of the experimental levels, to estimate transition probabilities of excited states using Eq. 2.8, where I_i and I_f are the total angular momenta of the initial and final states, respectively.

$$T_{fi}(\lambda L; I_i \rightarrow I_f) = \frac{1}{4\pi\varepsilon_o} \; \frac{8\pi(L+1)}{\hbar L[(2L+1)!!]^2} \left(\frac{E_\gamma}{\hbar c}\right)^{2L+1} B(\lambda L; I_i \rightarrow I_f) \qquad (2.8)$$

The numerical values of several constants included in Eq. 2.8 are as follows:

$$\frac{1}{4\pi\varepsilon_o} = 1.44 \text{ MeV - fm / e}^2 \tag{2.9}$$

$$\hbar = 6.58 \times 10^{-22} \text{ MeV} - \text{s} \tag{2.10}$$

$$\hbar c = 197.329 \text{ MeV} - \text{fm} \tag{2.11}$$

In Eq. 2.8, the B(λL) depends on a matrix element which contains the wave functions of only the initial and final nuclear states, and no dependence on the wave function of the photon. The photon characteristics are included in the factors preceding the B(λL), which are mathematically derived using the "long wavelength approximation" for the emitted photon, using a crude estimate of the radial wave function matrix element.

Finally, the mean partial lifetime of the state i undergoing a transition to state f, τ_{fi} (in seconds), is calculated as the inverse of T_{fi} (s^{-1}), and the corresponding partial half-life of the state i decaying to state f is obtained as $t_{1/2,fi} = (\ln 2)\ \tau_{fi} = 0.693\ \tau_{fi}$.

2.2 The Spherical Shell Model and Shell-Model Calculations

Near stability, nuclei have been successfully explained since the 1950s by the spherical shell model [May49, Hax49, May55] based on the independent movement of nucleons under a common average spherical potential. In the shell model, protons and neutrons occupy discrete energy levels forming particularly stable spherical structures at certain "magic" numbers of protons and/or neutrons. This model works particularly well for light nuclei, for nuclei with numbers of nucleons that are close to the magic ones, and at low excitation energies. The analytical form of the potential as a function of r (the distance between each nucleon and the center of mass of the nucleus) is not known

exactly; several empirical models for the potential have been proposed, the most common of which are the Woods-Saxon (WS) and the Harmonic Oscillator (HO), in Eqs. 2.12 and 2.13, respectively. The WS potential is a reasonable estimate of the radial charge distribution of the nucleus, and the HO potential is an approximation that is valid for very light nuclei at low excitation energy.

$$V_{WS}(r) = -V_0 \frac{1}{1+\exp\left(\frac{r-R}{a}\right)} \tag{2.12}$$

$$V_{HO}(r) = -V_o + kr^2 \tag{2.13}$$

In the expression for V_{WS} (r), R is the nuclear radius where $R = r_0 A^{1/3}$ with $r_0 \sim 1.2$ to 1.25 fm and a ~ 0.5 to 0.6 fm is the nuclear diffuseness parameter. In both WS and HO potentials, V_0 is on the order of 40-50 MeV. The WS potential is roughly constant in the center of the nucleus, rapidly approaching zero for r ~ 1-2 fm (consistent with the nuclear force being a short-range interaction). The HO potential diverges for distances above the nuclear radius (1-2 fm), but it satisfactorily models nuclear matter at distances below and up to the nuclear radius. The HO potential has the advantage of being easier to manipulate mathematically. Both WS and HO models correctly predict the magic numbers at 2, 8 and 20, but fail above 20. The addition of a spin-orbit potential (Eq. 2.14) between the intrinsic spin of the nucleon (**s**) and its own angular momentum (**ℓ**) [May49, May55] allowed the successful prediction of the experimentally-observed magic numbers at 2, 8, 20, 28, 50, etc.

The spin-orbit potential is given by:

$$V_{so} = f_{so}(r)\,\vec{s}\cdot\vec{\ell} \tag{2.14}$$

A complete shell-model description of the nucleus however involves the contribution from an average central potential (such as those in Eqs. 2.12 and 2.13) plus additional terms due to extra nucleon-nucleon interactions beyond the average potential. The derivation of this complete shell-model description starts by defining the full Hamiltonian of the A-nucleon system (Eq. 2.15), which includes all the two-body nucleon-nucleon potentials, $V_{ij}(r_{ij})$, where $r_{ij} = | \mathbf{r}_i - \mathbf{r}_j |$ is the distance between nucleons i and j, and ignores three-body interactions.

$$H = \sum_{i=1}^{A} \frac{p_i^2}{2m} + \sum_{i<j=1}^{A} V_{ij}(r_{ij}) \tag{2.15}$$

Ignoring third- and higher-order interactions among nucleons is an approximation that works best for the case of fewer valence particles [Bro01]. As more valence particles are added, the effect of higher-order interactions starts to be more significant, but they are excluded from shell-model calculations due to computational limitations. Shell-model codes including three-body forces are currently under development.

The non-relativistic (NR) Schrödinger equation with this Hamiltonian (Eq. 2.15) is not analytically solvable for three or more nucleons, and the problem can only be approached numerically. An additional complication is the fact that the nucleon-nucleon potentials V_{ij} are not known exactly. The approach of the single-particle shell model is to separate the sum of the V_{ij} potentials into two parts: one that is spherically-symmetric (the sum of independent-particle potentials $V_C(r_i)$ where r_i is the distance from nucleon i to the center of mass of the nucleus) and a remaining residual term V_{res} which is small compared with the rest of the Hamiltonian and is treated as a perturbation in first-order perturbation theory (Eq. 2.16):

$$H = \sum_{i=1}^{A}\left(\frac{p_i^{\,2}}{2m} + V_C(r_i)\right) + \left(\sum_{i<j=1}^{A} V_{ij}(r_{ij}) - \sum_{i=1}^{A} V_C(r_i)\right) = (H_0) + (V_{res}) \qquad (2.16)$$

The solution of the H_0 Hamiltonian is a number of independent-particle energy levels corresponding to the case where the nucleons are completely independent of each other, and V_C usually takes the form of either V_{WS} or V_{HO} above (Eqs. 2.12, 2.13). The resulting independent-particle energy levels and magic numbers are represented in Fig. 2.1 for a relatively low excitation energy range.

The application of the residual potential V_{res} in first-order perturbation theory has the effect of accounting for the interactions or "correlations" between nucleons beyond the spherically-symmetric potential. Different shell-model calculations use different forms of the residual interaction, which is caused by pairing, short- and long-range proton-neutron interactions, etc.; an extensive review on residual interactions was given in [Bro01]. The residual interactions are phenomenological and therefore derived from available nuclear structure experimental data. A given shell-model calculation provides a set of effective (spherical) single-particle energies (ESPE's), which are the single-particle energies modified by the presence of residual interactions [Ots01a].

Elements of a Shell-Model Calculation

The elements of a shell-model calculation are:

(1) A choice of "model space", or the number of independent-particle orbitals where valence nucleons (those located outside of an "inert" or closed-shell core) are allowed to reside. A "partition" is defined as a specific distribution of the valence nucleons (n_v) in the valence orbitals composing the model space. The most accurate results are expected when the model space is as large as possible. A "full" or "complete" shell-model

calculation takes into account all possible partitions (or configurations) in the model space, while a "truncated" shell-model calculation imposes a limit on the number of partitions that are considered; this imposition is due to limited computational resources.

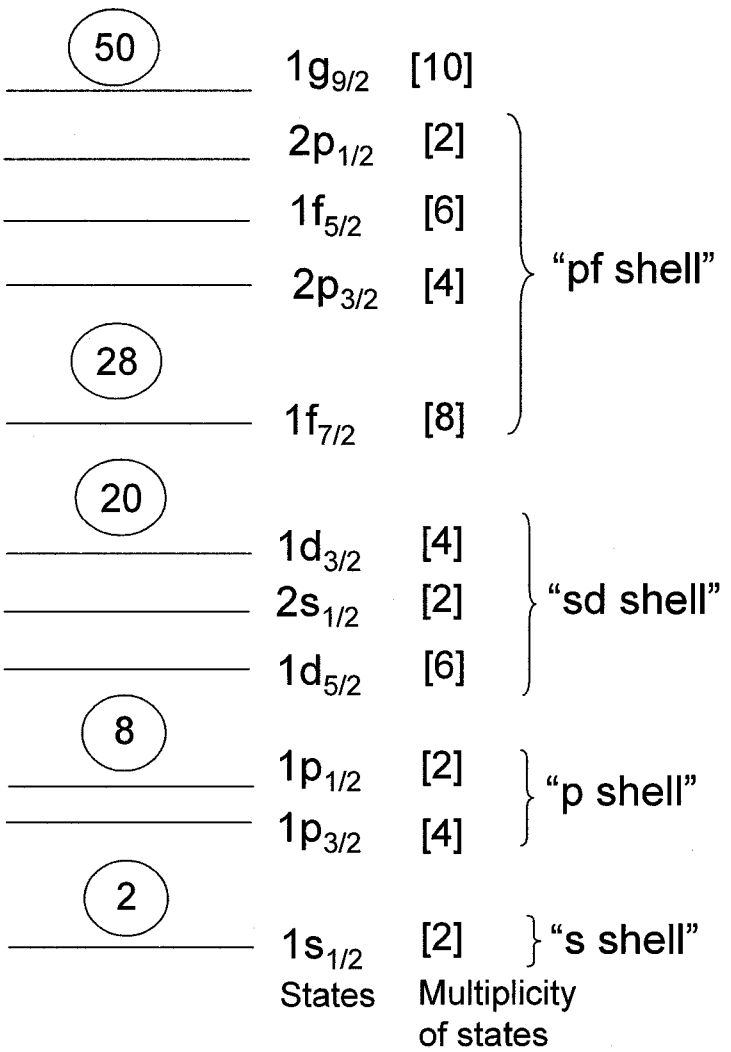

Figure 2.1 Schematic diagram (not to scale) of the independent-particle shell-model states for neutrons, indicating the locations of the magic numbers and the multiplicity (maximum occupancy) of states.

(2) A set of values for the single-particle energies (SPEs) given by the independent-particle shell model, that is, by an inert core described by a mean field [Bro01], e.g., a Woods-Saxon or a Harmonic Oscillator potential.

(3) The residual or effective interaction(s), V, used to generate two-body matrix elements (TBMEs) between pairs of valence nucleons. The TBMEs have the form: $\langle j_1 j_2 \mid V \mid j_1' j_2' \rangle_{JT}$, for all possible combinations of j_i orbitals in the model space. J is the magnitude of the total angular momentum from the coupling of the nucleon j_i angular momenta and T is the total isospin of the pair of nucleons. The z-component of isospin of a nucleus, T_z, is defined as $(N - Z) / 2$. From T_z, the isospin quantum number T can take the values $T = -T_z, -T_z + 1, \ldots, 0, \ldots +T_z$. The isospin of a pair of nucleons is thus $T = 0$ or 1. The number of TBMEs is also restricted to the limited number of allowed partitions or configurations given by the specific truncation method chosen.

A given shell-model calculation starts by selecting a certain model space, a set of values for SPEs, and a set of TBMEs using the appropriate residual interactions. The calculation then proceeds by diagonalizing the Hamiltonian matrix thus obtaining the corresponding "effective single-particle energies" (ESPEs).

The experimental data in this thesis were compared with two types of shell-model calculations: (1) those where the model space was restricted to the sd shell, especially the case using the "universal" SD (USD) interaction, and (2) those calculations where the model space included orbitals in the sd and pf shells, focusing on calculations applying the so-called SDPF-M interaction.

sd-Shell Calculations

The most widely used sd-shell interaction is the USD, or "universal" SD interaction [Wil84], where the first eight protons and eight neutrons are confined to the s and p shells, forming an inert core of ^{16}O. The remaining (Z – 8) and (N – 8) valence nucleons are distributed anywhere in the sd shell, which is composed of the $1d_{5/2}$, $2s_{1/2}$, and $1d_{3/2}$ orbitals located below the N = 20 shell gap (Fig. 2.1). Configurations where valence protons and neutrons are confined to sd-shell orbitals are called "normal" configurations. The USD interaction was developed by finding a unique set of TBMEs that fitted a large volume of experimental data on sd-shell nuclei, hence its name "universal".

The computer code OXBASH [Bro88] is used to implement calculations using the USD interaction. The calculations involve the three single-particle energies (SPEs) in the sd shell, and all possible (63) TBMEs in the sd shell, of the form $\langle j_1 j_2 \mid V \mid j_1' j_2' \rangle$. OXBASH is said to perform a full shell-model calculation, since it takes into account all possible configurations in the model space. A comparison between experimental data and predictions by OXBASH showed [Wil80] that the USD interaction alone was not able to predict the experimentally observed high binding energies of $^{30,31}Na$ and $^{31,32}Mg$, the first experimental indication of an anomalous region later called the "island of inversion".

sdpf-Shell Calculations

An sdpf-shell calculation involves four types of TBMEs [Bro01]:

(A) $\langle sd, sd \mid V \mid sd, sd \rangle$

(B) $\langle pf, pf \mid V \mid pf, pf \rangle$

(C) $\langle sd, pf \mid V \mid sd, pf \rangle$

(D) $< sd, sd \mid V \mid pf, pf >$

The TBMEs are calculated separately for protons and neutrons. A given TBME represents "pair scattering" of a pair of protons or neutrons. For example, in the case of TBMEs for neutrons, the "cross-shell" term C represents the scattering of a neutron originally located in a certain orbital of the sd shell to another orbital in the same sd shell, and the scattering of the second neutron from a position in the pf shell to another position in the same pf shell. The "off-diagonal" term D represents the case where a neutron in the sd shell scatters into the pf shell and another neutron in the sd shell scatters also into the pf shell.

Early sdpf-Shell Calculations

The first model that included orbitals other than those in the sd shell alone [Wat81] allowed the excitation of neutrons to the $1f_{7/2}$ orbital. This model assumes, like that using the USD interaction, an inert core of ^{16}O. The valence protons are allowed to reside only in the $1d_{5/2}$ orbital. The valence neutrons first fill the $1d_{5/2}$ and the $2s_{1/2}$ orbitals and then up to four valence neutrons are allowed to cross the N = 20 shell gap and be located in the $1f_{7/2}$ orbital. This model found that the N = 18 ^{29}Na and ^{30}Mg are equally well described by the USD alone or by a model including the $1f_{7/2}$ orbital. The inclusion of the $1f_{7/2}$ orbital was found to be significant only for $N \geq 19$. For example, for the N = 19 ^{30}Na and ^{31}Mg isotopes, the model including the $1f_{7/2}$ orbital [Wat81] made better predictions for the binding energies than OXBASH (using the USD interaction). The structures of the N = 20 ^{31}Na and ^{32}Mg isotopes were found to be dominated by the $(1d_{3/2})^{-2}(1f_{7/2})^2$ 2p2h

(2-particle – 2-hole) configuration, and the predictions for the binding energies in the N = 20 nuclei were better using this model [Wat81] than using the USD interaction.

One of the first models incorporating two orbitals ($1f_{7/2}$ and $2p_{3/2}$) out of the four in the pf shell was that of Poves and Retamosa [Pov87, Pov94]. In their model the inert core is ^{16}O and the (Z – 8) valence protons are confined to the $1d_{5/2}$ orbital, while the (N – 8) valence neutrons are located either in the sd shell or in two of the orbitals of the pf shell: $1f_{7/2}$ or $2p_{3/2}$. Their shell-model truncation allows only for excitation of up to two neutrons (2p2h configuration) from the $1d_{3/2}$ to the $1f_{7/2}$. According to this shell-model calculation, the low-energy spectra of Ne, Na and Mg are predicted to be dominated by 2p2h configurations for nuclei with $N \geq 20$ and $Z \leq 12$, suggesting a transition from spherical to deformed ground states happening at N = 20. The model predicts a 2p2h configuration of the ground state equal to 6%, 11% and 80% (the remainder being the percentage of 0p0h configuration) for ^{28}Ne, ^{29}Ne, and ^{30}Ne, respectively. The model also predicts ground-state 2p2h configurations of 5% and 77% for ^{30}Mg and ^{32}Mg, respectively. Predicted energy levels of N = 20 ^{30}Ne and ^{32}Mg are suggested to fit rotational spectra [Pov94]. The conclusion of these calculations is that the dominance of "intruder" (2p2h) configurations causes deformation, and that the onset of deformation takes place at N = 20 for $Z \leq 12$ neutron-rich nuclei, in agreement with earlier models [Wat81].

The "Island of Inversion" sdpf-Shell Calculation

An improvement beyond the above-mentioned models was proposed by Warburton *et al.* [War90] in a paper which introduced the concept of the "island of inversion",

proposed to be centered at Z = 11 and N = 21. The model incorporates all three orbitals in the sd shell ($1d_{5/2}$, $2s_{1/2}$, and $1d_{3/2}$) and all four orbitals in the pf shell ($1f_{7/2}$, $2p_{3/2}$, $1f_{5/2}$, and $2p_{1/2}$), and the Hamiltonian is called WBMB (developed by Warburton, Becker, Millener and Brown). The shell-model calculation is truncated so that valence protons are only allowed in the $1d_{5/2}$ orbital, excitations to the pf shell are only allowed for neutrons (and not for protons), and neutron holes are formed only in the $1d_{3/2}$ orbital. Different types of TBMEs use different interactions. For type A, the interaction used is the USD [Wil84], for type B, the interaction used is the so-called FPMG pf-shell interaction which assumes a ^{40}Ca inert core and includes 195 TBMEs for the four levels in the pf shell. The cross-shell (C) and the off-diagonal (D) TBMEs are calculated from a Millener-Kurath potential. Calculations of energies of the 0p0h and 2p2h configurations yield E(2p2h) < E(0p0h) for nine nuclei centered around Z = 11 and N= 21; this region is identified as the "island of inversion" where the ground states are expected to be dominated by intruder (2p2h) configurations. These results are consistent with previous shell-model calculations [Pov87, Pov04].

In this "island of inversion" model, the only isotopes calculated to belong to the island are a group of nine isotopes with N ≥ 20, centered around ^{32}Na. As we will see, there is some recent experimental evidence that the dominance of intruder configurations starts at N < 20. The following shell-model calculation (MCSM with the SDPF-M interaction) was developed in an attempt to fit these new experimental data and thus account for the seemingly larger "island of inversion" region.

Monte Carlo Shell-Model Calculations (MCSM) and the SDPF-M Interaction

Recently developed large-scale shell-model calculations [Fuk92, Ots01a, Ots01b, Ots04, Uts99, Uts01, Uts05, Uts07] are collectively referred to as Monte Carlo Shell-Model Calculations (MCSM), which use an sdpf-shell interaction called SDPF-M.

MCSM differs from earlier sdpf-shell calculations in the following:

(a) MCSM uses a valence (or model) space where both valence protons and neutrons are allowed to reside in any orbital of the sd shell and the $1f_{7/2}$ and $2p_{3/2}$ orbitals of the pf shell; the inert core is ^{16}O.

(b) All configurations in the valence space are allowed, that is, the shell-model calculation is complete (no truncations). In particular, MCSM allows the promotion of any number of valence neutrons (usually one, two or four) up to the maximum filling of the two lower orbitals the pf shell, leaving the same number of holes in the sd shell, resulting in the so-called "intruder" configurations (1p1h, 2p2h, 4p4h, etc.).

(c) MCSM uses a computational procedure called the Quantum Monte Carlo Diagonalization (QMCD) method [Ots01b], which is appropriate for solving the large-scale Hamiltonian of this model.

(d) MCSM uses the following TBMEs: for type A, the USD interaction; for type B, the Kuo-Brown renormalized G matrix; for C and D, the Millener-Kurath interaction.

(e) The effective or residual interaction in MCSM includes a strong "spin-isosopin monopole term" (Eq. 2.17), which is assumed to dominate the structure of the light N ~ 20 neutron-rich nuclei. The monopole term includes parameters than can be adjusted so that the shell-model calculation fits a range of available nuclear structure experimental

data. The monopole interaction (Eq. 2.17) is particularly strong between neutrons and protons and between spin-orbit partners, that is, levels with the same ℓ but with j taking the values $j_> = \ell + 1/2$ and $j_< = \ell - ½$. In the neutron-rich N ~ 20 region a strong monopole interaction is assumed to exist between the $1d_{5/2}$(proton) – $1d_{3/2}$(neutron) levels.

$$V_{\sigma\tau} = f_{\sigma\tau}(r_{12})\,(\boldsymbol{\sigma}_1 \cdot \boldsymbol{\sigma}_2)\,(\boldsymbol{\tau}_1 \cdot \boldsymbol{\tau}_2) \qquad (2.17)$$

In Eq. 2.17, $\boldsymbol{\sigma}_1$ and $\boldsymbol{\sigma}_2$ are the spin operators, $\boldsymbol{\tau}_1$ and $\boldsymbol{\tau}_2$ are the isospin operators, and r_{12} is the distance between nucleons 1 and 2. Details on the application of this interaction in the MCSM shell-model calculations can be found in [Ots01a].

The idea of the proton-neutron interaction as a significant contributor to deformation is not new however. In [Fed77, Fed79] the short-range proton-neutron (p-n) interaction was presented as a cause of deformation not only in light neutron-rich nuclei but across the nuclear chart. An example is given where ^{20}Ne (with two valence protons and two valence neutrons outside a ^{16}O inert core) has a rotational spectrum while ^{20}O (with four valence neutrons) is spherical; the rotational deformation in ^{20}Ne was attributed to the p-n interaction.

Predictions of MCSM for the N ~ 20 Neutron-Rich Region

In the N ~ 20 neutron-rich nuclei the strong monopole interaction (Eq. 2.17) between the $1d_{5/2}$ protons and the $1d_{3/2}$ neutrons is proposed as a unified explanation of the so-called "shell evolution" [Ots01b, Ots04]: the dramatic change in the extent of the N = 20 shell gap in the N = 20 isotones when moving from ^{40}Ca to ^{30}Ne as predicted by MCSM calculations (Fig. 2.2(b)). This calculated "shell evolution" is contrasted with the virtually

constant N = 20 shell gap (~5 MeV) predicted by the independent-particle shell model, as well as by other shell-model calculations which do not take the proton-neutron interaction into account (Fig. 2.2(a)).

According to the MCSM calculations in Fig. 2.2 (b), while the N = 20 shell gap is ~6 MeV in ^{40}Ca (Z = 20), it gets reduced to ~3 MeV in ^{32}Mg (Z = 12) and ~2 MeV in ^{30}Ne (Z = 10). The reduction in the N = 20 shell gap (with the simultaneous increase in the N = 16 gap) is most significant when moving from Z = 14 to Z = 10 at constant N = 20 (^{34}Si to ^{30}Ne) due to the steep slope of the $1d_{3/2}$ neutron orbital, resulting in a closer approach between the neutron $1d_{3/2}$ and $1f_{7/2}$ levels. The steep slope of the $1d_{3/2}$ neutron orbital between Z = 14 and Z = 10 can be understood as due to the removal of the protons located in the $d_{5/2}$ proton orbital so that the effective interaction between the $\pi d_{5/2}$ and the $\nu d_{3/2}$ gets reduced and the $d_{3/2}$ neutrons become less bound. The resulting weakening of the N ~ 20 shell gap in turn favors the promotion of pairs of neutrons to the pf shell (leaving pairs of holes in the sd shell). Additional correlations between the $1d_{5/2}$ protons and the $1f_{7/2}$ and $2p_{3/2}$ neutrons contribute to the additional binding of these neutron-rich nuclei.

Figure 2.2 compares the predicted evolution of the N = 20 shell gap in the N = 20 isotones from ^{40}Ca to ^{28}O, calculated by two different shell-model codes: OXBASH with the WBMB interaction (Fig. 2.2(a), [War90]) and MCSM with the SDPF-M interaction (Fig. 2.2(b), [Uts99, Ots01a]); the latter calculation includes a strong proton-neutron interaction, while the first does not. While the calculations with the SDPF-M interaction show a dramatic reduction of the N = 20 gap when moving from Z = 20 to Z = 10 in the N = 20 isotones, the calculations using the WBMB interaction [War90] show only a

moderate decrease of the shell gap from ~7 MeV in ^{40}Ca to ~5.5 MeV in ^{30}Ne. According to [War90], the decrease in the N = 20 shell gap between the sd and the pf shells contributes to but it is not the primary cause of the inversion (intruder dominance of the ground state). The model by [War90] predicts that the island of inversion region is restricted to only nine nuclei centered around ^{32}Na. However, more recent experiments on nuclei located at the transition to the island of inversion show that the island of inversion includes also nuclei with N < 20. The MCSM model with the SDPF-M interaction instead is able to predict inversion in nuclei with N < 20; the better comparison of the MCSM predictions with experimental data is suggested to be due to the drastic reduction in the N = 20 shell gap, or "shell evolution. The reduction in the N = 20 shell gap is attributed to the strong effect of the proton-neutron interaction, an effect that was not included in models such as [War90] and many other earlier shell-model calculations.

Often, the normal (0p0h) and intruder (2p2h) configurations predicted by calculations using the SDPF-M interaction are close in energy, giving rise to a shape coexistence behavior: a coexistence of spherical and deformed ground states. Deformations may include rotational and/or vibrational modes.

Figure 2.3 shows the composition of the ground states of the N = 20 isotones [Uts01] predicted by MCSM. While the 2p2h configuration is dominant in ^{31}Na and ^{32}Mg, the strong mixing of 4p4h is evident in ^{29}F and ^{30}Ne. The dominance of the 2p2h configuration in ^{31}Na and ^{32}Mg compared to ^{29}F and ^{30}Ne is consistent with a large static quadrupole deformation which brings down a deformed (Nilsson-like) orbit from the pf shell and increases the energy of a deformed orbit from the sd shell. The large 4p4h probability in ^{29}F and ^{30}Ne is due to the reduced effective shell gap for neutrons.

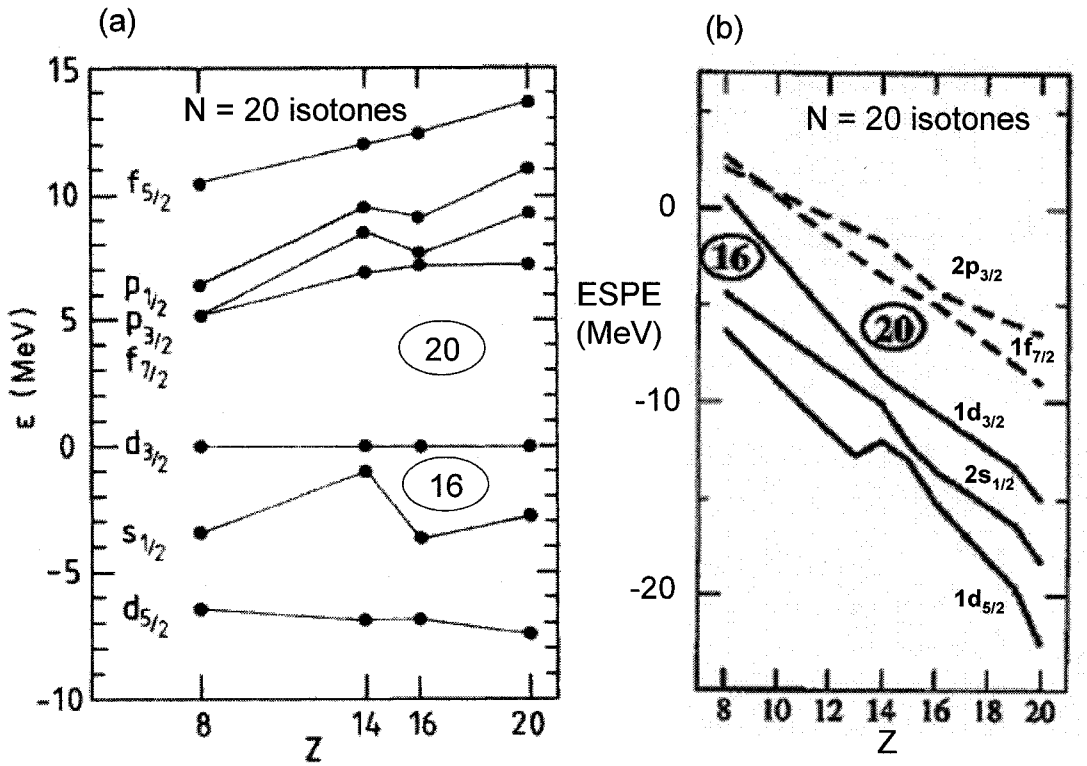

Figure 2.2 **Evolution of the N = 20 shell gap with Z in N = 20 isotones from ^{40}Ca (Z = 20) to ^{28}O (Z = 8), predicted by shell-model calculations using the OXBASH code with the WBMB interaction and the MCSM code with the SDPF-M interaction.** (a) Effective single particle energies (ESPEs) of neutrons relative to the ESPE of the neutron $1d_{3/2}$ orbital, calculated by OXBASH with the WBMB interaction (adapted from [War90]), (b) ESPEs of neutrons calculated by MCSM with the SPDF-M interaction (adapted from [Uts99, Ots01a]).

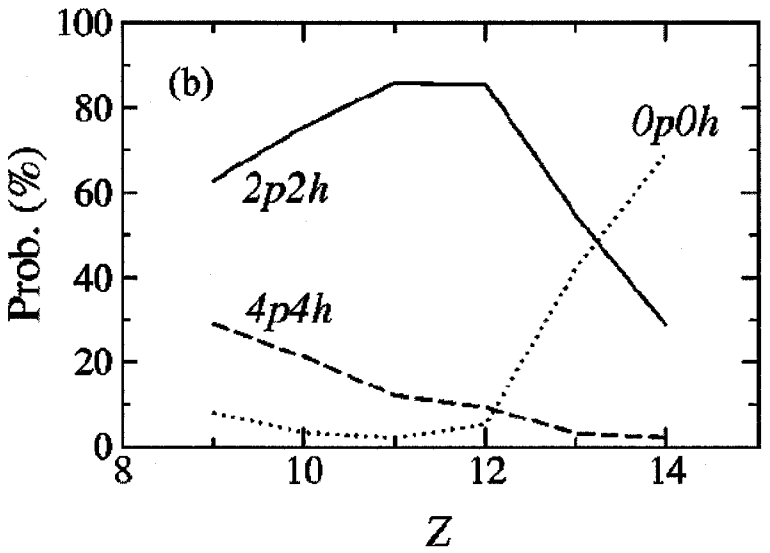

Figure 2.3 **Calculated (MCSM) ground-state composition of N = 20 isotones in terms of normal (0p0h) and intruder (2p2h and 4p4h) configurations, adapted from [Uts01].**

Predictions of MCSM for the Neutron-Rich Neons

MCSM calculations [Uts99] provide values for the $E(2_1^+)$, $E(4_1^+)$ and B(E2) in neutron-rich Ne isotopes (Figs. 2.4 and 2.5), of interest in this study. Decreasing values of excitation energies and increasing values of B(E2) predicted by MCSM show the increase in deformation of the neutron-rich neons as neutrons are added, starting from ^{26}Ne (N = 16) and showing a maximum deformation expected for ^{32}Ne (N = 22).

While earlier sdpf-shell calculations such as [Pov87, Pov94] predicted that intruder configurations would start to dominate the ground-state wave functions at N = 20, MCSM calculations [Uts99] predict that the intruder dominance in the ground state is already significant at N = 19. MCSM also shows discrepancies with earlier models regarding the structure of ^{28}Ne (N = 18). In the island of inversion model [War90] ^{28}Ne was classified as a "normal" nucleus, while in MCSM [Uts99] ^{28}Ne has a mixed 50-50% normal-intruder configuration in the ground state, so that ^{28}Ne is likely to be at the border

of the island of inversion. Experimental data on the neutron-rich neons, and especially on N = 18 ^{28}Ne, constitute a key measurement to test current shell-model predictions and the transition to the island of inversion.

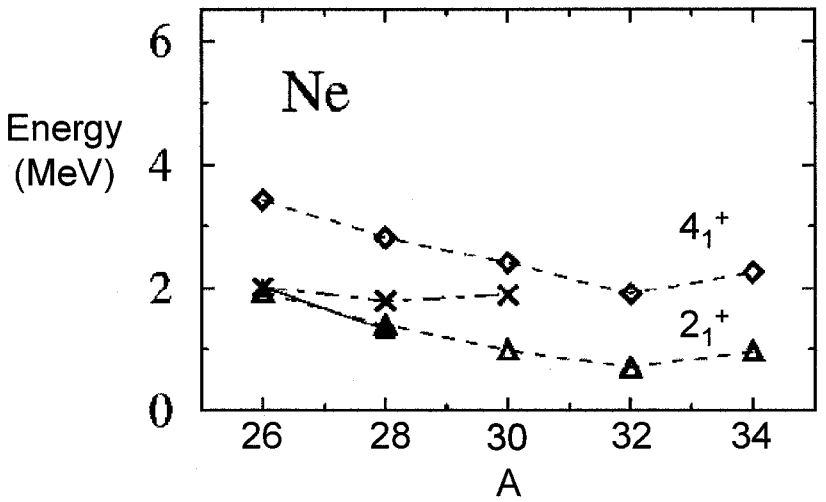

Figure 2.4 Predictions for the E(2_1^+) and E(4_1^+) energies (MeV) in neutron-rich neons, adapted from [Uts99]. The open triangles and diamonds are the 2_1^+ and 4_1^+ energies, respectively, calculated using the SDPF-M interaction. The filled triangles are experimental 2_1^+ energies. The crosses represent 2_1^+ energies calculated by the sd-shell model.

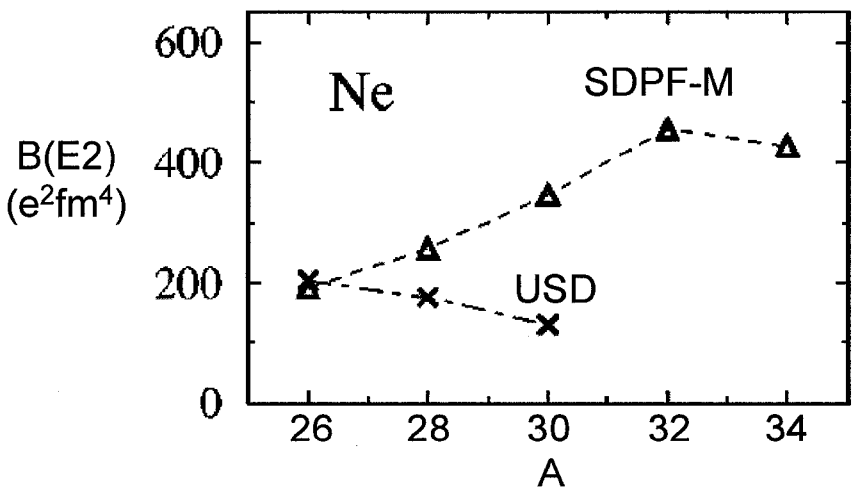

Figure 2.5 Predictions for the B(E2) values (e^2fm^4) in neutron-rich neons, adapted from [Uts99]. The open triangles mean values calculated with the SDPF-M interaction, while the crosses were obtained using the sd-shell model.

2.3 Collective Models and Collective Phenomena

The independent-particle shell model works best when there are only a few valence nucleons outside an inert or closed-shell inner core. When the number of valence particles increases, the experimentally-observed excited states of the nucleus are located at energies lower than predicted by the "pure" independent-particle model. The first excited state of even-even nuclei is almost always a 2_1^+; a low energy of the 2_1^+ state, $E(2_1^+)$, is a sign of collectivity in the nucleus. An intuitive explanation for the low $E(2_1^+)$ is offered by assuming that this state is the result of the collective interaction of a large number of nucleons: not only the valence nucleons but also those located in inner lower-energy shells.

Several nuclear properties are used as indicators of collective phenomena, in particular: the energy $E(2_1^+)$, the ratio of $E(4_1^+)/E(2_1^+)$, the magnetic dipole moment of the 2_1^+ state $\mu(2_1^+)$ in units of μ_N, and the electric quadrupole moment of the 2_1^+ state $Q(2_1^+)$ in barns, as well as transition strengths such as $B(E2; 0_1^+(g.s.) \rightarrow 2_1^+)$ and B(M1) values. From some of these magnitudes it is possible to derive other parameters that are a measure of the degree of collectivity of the nucleus, specifically the intrinsic quadrupole moment Q_0 and the deformation parameter β (Section 2.3.2).

2.3.1 Vibrational and Rotational Collective Excitations

$E(2_1^+)$ decreases for increasing A, except for discontinuities near closed shells. The ratio of $E(4_1^+)/E(2_1^+)$ has values between two extremes: ~2, characteristic of vibrational excitations around a spherical equilibrium shape (most frequent for nuclei with $A < 150$),

and ~ 3.3, characteristic of rotational excitations above a non-spherical equilibrium shape (most frequent for nuclei with $150 < A < 190$ and $A > 230$ [Kra88]).

Vibrational Excitations

Vibrational excitations are described by the Bohr and Mottelson model [Boh75]. Equation 2.18 introduces a time-dependent radius as a function of a number of parameters, where R_o is the radius of the spherical equilibrium shape. Only quadrupole vibrations are considered here, as they are the most common types of vibrations observed in nuclei. The expression for the temporal variation of the radius, restricted to quadrupole vibrations so that $\mu = 0, \pm1, \pm2$, is given by:

$$R(\theta,\phi,t) = R_o\left(1+\sum_{\mu=-2}^{+2}\alpha_\mu(t)\,Y_{2\mu}(\theta,\phi)\right) \tag{2.18}$$

The quantities α_μ ($\mu = 0, \pm1, \pm2$) in Eqs 2.19-2.21 are called deformation parameters. If one or more of the α_μ parameters are $\neq 0$ the nucleus is deformed; otherwise it is spherical. Deformation in nuclei is commonly expressed as a function of the Bohr variables, β and γ, which are related to the α_μ coefficients by the following expressions:

$$\alpha_o = \beta\cos\gamma \tag{2.19}$$

$$\alpha_2 = \alpha_{-2} = \frac{1}{\sqrt{2}}\beta\sin\gamma \tag{2.20}$$

$$\alpha_1 = \alpha_{-1} = 0 \tag{2.21}$$

The vibrational spectra can then be classified according to the values of β and γ, and vibrations are many times referred to as β- and γ-type. Since the excitations are of the quadrupole type, the β value is also referred to as β_2 (β and β_2 are used interchangeably).

Quadrupole vibrational excitations are characterized by the spherical harmonics of order two, $Y_{2\mu}(\theta,\varphi)$. Lower- and higher-order harmonics are not taken into account, as dipole modes do not give rise to vibrational excitations at low excitation energies, while higher-order vibrations (octupole, etc.) are not relevant for light nuclei.

Quadrupole vibrations of spherical nuclei are characterized by $\beta = \beta_{equil} = 0$, and any value of γ. In the limit of pure unperturbed quadrupole vibrations, the lowest vibrational states are equally separated in energy, equal to a phonon or quantum of vibrational energy ε. The energy of each vibrational state n is then $E = \varepsilon n$, and each vibrational state contains a series of vibrational multiplets of different I value (for $n = 0$, $I^{\pi} = 0^{+}$; for $n = 1$, $I^{\pi} = 2^{+}$; for $n = 2$, $I^{\pi} = 0^{+}, 2^{+}, 4^{+}$ (coupling of two phonons with $I^{\pi} = 2^{+}$ each); for $n = 3$, $I^{\pi} = 0^{+}, 2^{+}, 3^{+}, 4^{+}, 6^{+}$ (coupling of three phonons with $I^{\pi} = 2^{+}$ each); etc. The individual members of a multiplet have exactly the same energy in the extreme limit of pure unperturbed quadrupole vibrations. Quadrupole vibrations carry two units of angular momentum and can be of two types: $K = 0$ and $K = 2$. $K = 0$ are known as β vibrations: the vibration is aligned along the symmetry axis and therefore preserves axial symmetry. The $K = 2$ model is called a γ vibration and represents a dynamic time-dependent excursion from axial symmetry.

Rotational Excitations

Rotations take place on the basis of a deformed nucleus, that is, a nucleus having a permanent quadrupole deformation in its ground state, assumed cylindrical.

As the ground-state shape of the nucleus is cylindrical, the spherical harmonics in Eq. 2.18 depend only on θ, i.e., $Y_{2\mu}(\cos\theta)$. Restricting to the case of an axially symmetric

deformation characterized by a constant equilibrium deformation $\beta_{equil} \neq 0$, there are two types of rotations, depending on whether $\gamma = 0^o$, or γ can take any value (γ instability). In the case of $\gamma = 0^o$, the rotational spectra consist of a series of energy levels, called bands, connected by large electric quadrupole (E2) transitions. Within each band, the excitation energies are given by Eq. 2.22, which is the quantum-mechanical version of the energies of a body undergoing classical rotations:

$$E = \frac{\hbar^2}{2\zeta} I(I+1) \tag{2.22}$$

In Eq. 2.22, ζ is the moment of inertia of the nucleus about its symmetry axis z, and I is the total angular momentum, or spin, of a given excited state. In even-even nuclei, the band built on the ground state is composed of levels with $I^{\pi} = 0^+, 2^+, 4^+$, etc.; levels are connected by greatly enhanced probabilities for electric quadrupole (E2) transitions.

Nuclei never behave like rigid rotors, but instead the experimental moments of inertia are lower than the predictions assuming a rigid rotor.

2.3.2 Deformation Parameters

Assuming that the excited 2_1^+ state of a nucleus fits the rotational model, an expression has been derived [Boh75] that allows relating the intrinsic quadrupole moment Q_0 to the reduced transition probability B(E2; $0_1^+ \rightarrow 2_1^+$), as expressed in Eq. 2.23, where e is the electronic charge:

$$B(E2; 0_1^+ \rightarrow 2_1^+) = \frac{5}{16\pi} e^2 Q_0^2 \tag{2.23}$$

Also within the rotational model, the intrinsic quadrupole moment Q_0 is to first order directly proportional to the quadrupole deformation parameter β_2 (Eq. 2.24):

$$Q_0 = \frac{3}{\sqrt{5\pi}} Z R^2 \beta_2 \tag{2.24}$$

Combining Eqs. 2.23 and 2.24, the quadrupole deformation parameter can be expressed as:

$$\beta_2 = \frac{4\pi}{3} \frac{\sqrt{B(E2\uparrow)}}{ZeR^2} \tag{2.25}$$

where B(E2↑) is the transition strength B(E2; $0_1^+ \rightarrow 2_1^+$). In Eqs. 2.18, 2.24 and 2.25, R represents the radius of the equivalent spherically-shaped nucleus of the same volume.

2.4 The Nilsson Model

The Nilsson model can be considered a single-particle shell model where the potential has been modified to be deformed rather than spherical, and was proposed to account for properties of deformed nuclei whose structures are not near closed-shell behavior. While the spherical potential did not allow for a distinction in the energies of different magnetic substates of a given orbit ℓ, this degeneracy is broken in the deformed potential of the Nilsson model. The Nilsson potential is that of a harmonic oscillator where the oscillator frequencies are different along the three Cartesian coordinates. If the potential is cylindrical and the symmetry axis is z, there are two different oscillator frequencies: $\omega_x = \omega_y$ and ω_z. Once the Hamiltonian is solved, the eigenvalues can be written:

$$E(N, n_z) = \hbar\omega_x(N-n_z+1) + \hbar\omega_z(n_z+1/2) \tag{2.26}$$

where $N = n_x + n_y + n_z$

In addition, spin-orbit and other terms can be added to the Nilsson model in a way similar to the case of the spherical shell model.

Resulting level sequences are called Nilsson diagrams, such as the one in Fig. 2.6, which is valid for neutrons or protons where $N(Z) \leq 50$. The abscissa, ε_2, is a deformation parameter (sometimes also denoted δ) that takes a positive (negative) value when the nucleus is prolate (oblate), and which is related to the quadrupole deformation parameter β_2 by Eq. 2.27:

$$\varepsilon_2 = 0.946\, \beta_2 \tag{2.27}$$

Each of the levels in the Nilsson diagram (Fig. 2.6) is labeled with the four numbers Ω [N n_z Λ] where Ω is the z-component (along the nuclear symmetry axis) of the angular momentum quantum number for that state, N and n_z are the quantum numbers in Eq. 2.26, and Λ is a quantum number representing the z-component of orbital angular momentum ℓ. The total angular momentum j of each orbital (unlike in the spherical shell model) is not a good quantum number any more; the number ℓ is also not a good quantum number in the Nilsson model. For zero deformation all the levels corresponding to the same j are degenerate. As deformation increases, the ordering of the energies also changes, even leading to the crossing of the original levels. The Nilsson diagram in Fig. 2.6 offers a possible explanation for the reduced N = 20 shell gap corresponding to a prolate deformation of the neutron-rich nuclei as will be further addressed in the discussion of the results (Chapter 6).

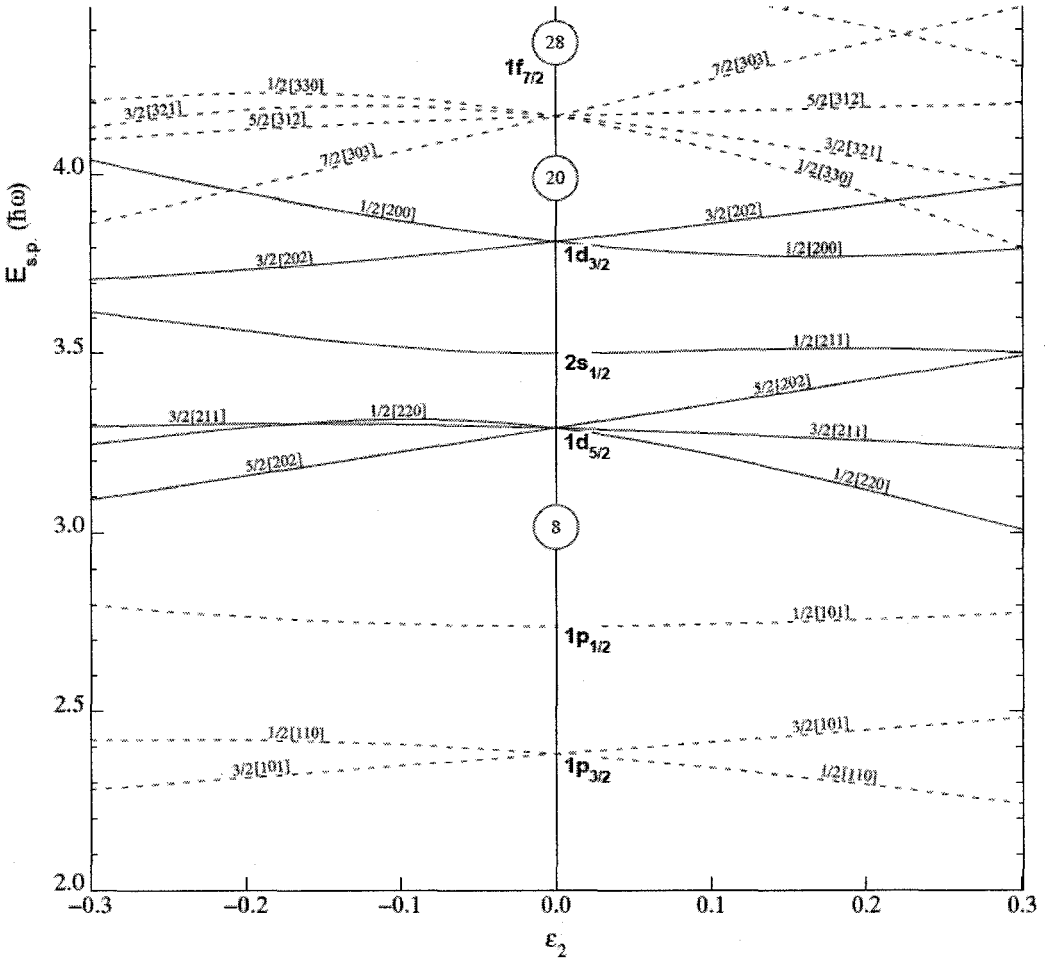

Figure 2.6 Nilsson diagram for Z or N ≤ 50 representing the single-particle levels as a function of the deformation parameter ε_2.

Chapter 3

Fragmentation and Few-Nucleon Knockout Reaction Theory

Since pioneering work three decades ago [Sym79], fragmentation [Mor98, Pod06] and few-nucleon knockout reactions [Han03] have increasingly been used as tools to produce and study neutron-rich nuclei. As more energetic and intense beams become available at facilities such as NSCL, RIKEN, GANIL, etc., it is possible to study nuclei with ever increasing neutron excesses. Neutron-rich nuclei have also been obtained in β-decay experiments, although this technique is limited by the fact that the β-decay parent of a desired neutron-rich product is often unbound [Ree99]. Other reactions such as Coulomb excitation [Gla98] and inelastic scattering [Yan03] are used to study excited states of neutron-rich beams.

In this thesis, fragmentation (Section 3.1) and few-nucleon knockout reactions (Section 3.2) were used to produce and study N ~ 20 neutron-rich isotopes. Fragmentation of a "primary" ^{48}Ca beam was used to produce "secondary" neutron-rich beams, which subsequently underwent few-nucleon knockout reactions to produce and study neutron-rich N ~ 20 neon isotopes.

Nuclear reactions can be generically written A(a,b)B, where A is the target, a the projectile, b an outgoing particle, and B a recoiling residue into which the target is transformed. When a and b are the same particle (and therefore A and B the same nucleus), the reaction is called scattering: elastic if B and b are in their ground states so

that the system's kinetic energy is conserved (only the trajectories and individual kinetic energies of the particles vary), and inelastic when part of the kinetic energy of the reactants A and a is converted into excitation energy of B and/or b. Scattering reactions are caused by both the strong and the Coulomb forces of the nucleus. In particular, inelastic scattering is used to populate and study excited states; an example from the neutron-rich region is the proton inelastic scattering of ^{30}Ne incident on a liquid hydrogen target [Yan03]. Coulomb excitation is caused by only the electromagnetic interaction between projectile and target resulting in the target gaining excitation energy. Coulomb excitation of even-even neutron-rich targets has been employed to populate their first excited states and to measure the corresponding reduced transition probability, B(E2; $0_1^+ \rightarrow 2_1^+$), thereby providing information on their collectivity [Gla98]. Coulomb excitation experiments are performed at relatively low beam energies, typically less than ~80% of the Coulomb barrier, in order to avoid contributions from the strong force.

Both fragmentation and knockout are types of "direct reactions". Direct reactions take place at high beam energies so that the time for the projectile to traverse a dimension equal to the nuclear diameter is much smaller than the nuclear period, defined as the time for a nucleon to describe a nuclear orbit (equal to ~10^{-22} s for a nucleus of A ~ 30 and typical nucleon kinetic energy of ~30 MeV). For an incident beam energy > 100 MeV/A, the time to traverse the nuclear diameter is < 10^{-23} s and thus the interaction time is short compared to the characteristic nuclear period.

Because of the large incident energy and short interaction time, in a direct reaction the projectile's deBroglie wavelength is small enough that it becomes more likely for the projectile to interact with a nucleon-sized object rather than with the nucleus as a whole

or many nucleons [Kra88 (p. 419), Sat83, Sat90]. As a consequence, direct reactions involve only a few nucleons, while the rest of the nucleons behave as passive spectators. Direct reactions also have a high probability to be peripheral.

3.1 Production of Neutron-Rich Nuclei by Fragmentation

Fragmentation, as it is referred to in this work, is a nuclear reaction where a heavy projectile above the energy of ~50 MeV/A collides peripherally with a light target nucleus [Mor98]. Fragmentation is described in terms of a "participant-spectator" model [Wes76]. The projectile-target overlapping region disintegrates into its constituent nucleons and the remaining or "spectator" part of the projectile becomes a "projectile fragment", having a larger excess of neutrons than the original projectile. Assuming protons and neutrons are uniformly distributed throughout the nuclear volume, a simple calculation illustrates how a fragment can have a larger excess of neutrons than the projectile from which it originated. For example, given the fragmentation of ^{48}Ca with $(Z_i, N_i) = (20, 28)$ and $N_i/Z_i = 1.40$, and assuming the removal of four nucleons (two protons and two neutrons), the resulting fragment has $(Z_f, N_f) = (18, 26)$, corresponding to a $N_f/Z_f = 1.44$, larger than the original 1.40.

Due to the high reaction energy, the projectile fragment is emitted mostly in the forward direction, retaining most of the original beam energy (above ~90%).

A common technique in radioactive-beam facilities is to perform fragmentation in two sequential steps with the goal of reaching nuclei further away from stability than possible with only one fragmentation step [Mor98].

Fragmentation has been theoretically explained by the two-step abrasion-ablation (AA) model [Gai91] (Section 3.1.1). Since cross sections have been found to be mostly independent of the beam energy in the range between ~100 and 2000 MeV/A, the Empirical Parametrization of Fragmentation Cross Sections (EPAX) (Section 3.1.2) has been developed to estimate fragmentation cross sections based on available experimental reaction data. The LISE computer code [Baz02, Tar07] (Section 3.1.3) uses the abrasion-ablation theory of fragmentation to estimate yields and cross sections of fragments from the impact of heavy beams on light targets in particular radioactive-beam facilities.

3.1.1 Abrasion-Ablation Model of Fragmentation

Fragmentation is modeled as a two-step process called abrasion-ablation (AA) [Gai91, Hüf75]. In the first non-equilibrium abrasion step, projectile "pre-fragments" are formed by the removal or abrasion of a number of nucleons due to the peripheral collision of the heavy projectile with a light target. This remaining portion of the projectile is thus composed of a number of "spectator" nucleons and is left with an excitation energy caused by the removal of nucleons during the abrasion process. The number of abraded nucleons depends on the projectile impact parameter. The abrasion model includes estimates for the excitation energy and angular momentum of the pre-fragments.

In the second stage (ablation), the pre-fragments undergo deexcitation by a quasi-equilibrium statistical decay involving particle and/or γ emission to form the final fragments.

The AA model of [Gai91] has been implemented in a Monte Carlo code called ABRALA. The predictions by ABRALA for the yield of fragments vs. their mass number A show good agreement with experimental data.

3.1.2 EPAX Parametrization of Fragmentation Cross Sections

Fragmentation is not well understood theoretically. Also, at a given beam energy, there is usually a mixture of processes (not just fragmentation) leading to the final products. The approach to predict the cross sections is therefore an empirical one, where formulas for cross sections, given by the EPAX empirical parameterization, are obtained by fitting to experimental data [Süm00]. The EPAX cross sections are found to reproduce ~85% of the experimental fragmentation cross section data within a factor of 2. The parametrization is more likely to fail far from stability because there are less experimental data. In this region, EPAX could differ from reality by factor of 5 [Süm00].

3.1.3 Computer Modeling of Fragmentation: LISE

LISE [Baz02, Tar04, Tar07] is a computer program that simulates the production and transport of radioactive ion beams by fragmentation in selected fragment-separator facilities. In particular, we used the LISE configuration files corresponding to the A1900 fragment separator and the S800 spectrograph (Chapter 4) at the National Superconducting Cyclotron Laboratory (NSCL) at Michigan State University (MSU), where the experiments were carried out. LISE was used to select primary beam types and intensities (in pps, or particles per second), target materials and thicknesses, energy-degrader wedge-shaped materials and thicknesses, A1900 and S800 magnetic rigidity

(Bρ) settings, etc., to achieve a given composition, intensity and purity of the secondary beams, and to select desired final fragments at certain minimum production rates and yields. The yield of a specific fragment is the ratio of the number of fragments of that type divided by the total number of fragments produced in the reaction. LISE is also used to plot the predicted particle identification (PID) spectrum at the S800 focal plane so that it can be used for comparison with the focal plane spectrum during an experimental run. The feasibility of an experiment depends fundamentally on the intensity of the secondary beams and final fragments. Because of uncertainties in the cross section libraries, LISE provides an "order of magnitude" estimate of intensities, i.e., predicted intensities could differ from experimental ones by a factor of 2 or 5, but usually not more than 10.

3.2 Few-Nucleon Knockout Reactions

Few-nucleon knockout reactions [Han03] are a type of direct reactions [Sat83] where relatively heavy and energetic (>50 MeV/A) beams interact with a light target resulting in the removal of one or two of the projectile peripheral nucleons while the remaining nucleons of the beam behave as passive spectators. As knockout reactions remove one or two nucleons from a shell-model orbital they are used to explore the single-particle shell structure of neutron-rich nuclei.

Because few-nucleon knockout is a direct reaction, generally written A(a,b)B, its cross section is specified by a quantum-mechanical transition amplitude or transition matrix element M between the initial state A,a and the final state b,B, and therefore involves an overlap between their wave functions [Kra88 (Ch. 11), Sat83]. The overlap, and thus the cross section, is proportional to the difference between the initial and final

states, i.e., is related only to the few removed nucleons and does not involve any of the other nucleons. In Eq. 3.1, the interaction V generally depends on many nuclear coordinates, ψ's are wave functions of the nuclei involved in the reaction, and $d\upsilon$ is an element of volume in the integration:

$$M = \int \psi_B^* \psi_b^* V \psi_A \psi_a d\upsilon \tag{3.1}$$

As a first approximation (plane-wave Born approximation, or PWBA), the incoming and outgoing wave functions, ψ_a and ψ_b, are treated as plane waves [Sat83]. The optical model is then used to take into account a distortion effect caused by the target nucleus on the incoming and outgoing plane waves, which is the basis of the distorted-wave Born approximation, or DWBA [Sat83].

3.2.1 One-Proton Knockout Theory

In one-proton knockout [Nav98, Tos99, Sau00, Mad01, Tos01, Tho03, Tos04a, Gad04a, Gad04b] the projectile of atomic mass number A interacts with the light target losing a proton and thus forming a "projectile residue" of mass A-1, also called the "core". The core continues moving in the forward direction with an energy close to that of the incident projectile energy.

One-proton knockout takes place by two modes of interaction [Han03]:

(a) "Stripping" or "inelastic breakup" (the most probable of the two modes), where the proton that is knocked out from the projectile of mass A is absorbed by the light target (Fig. 3.1(a)).

(b) "Diffractive dissociation" or "elastic breakup", where the removed proton is emitted elastically and not absorbed by the target (Fig. 3.1(b)).

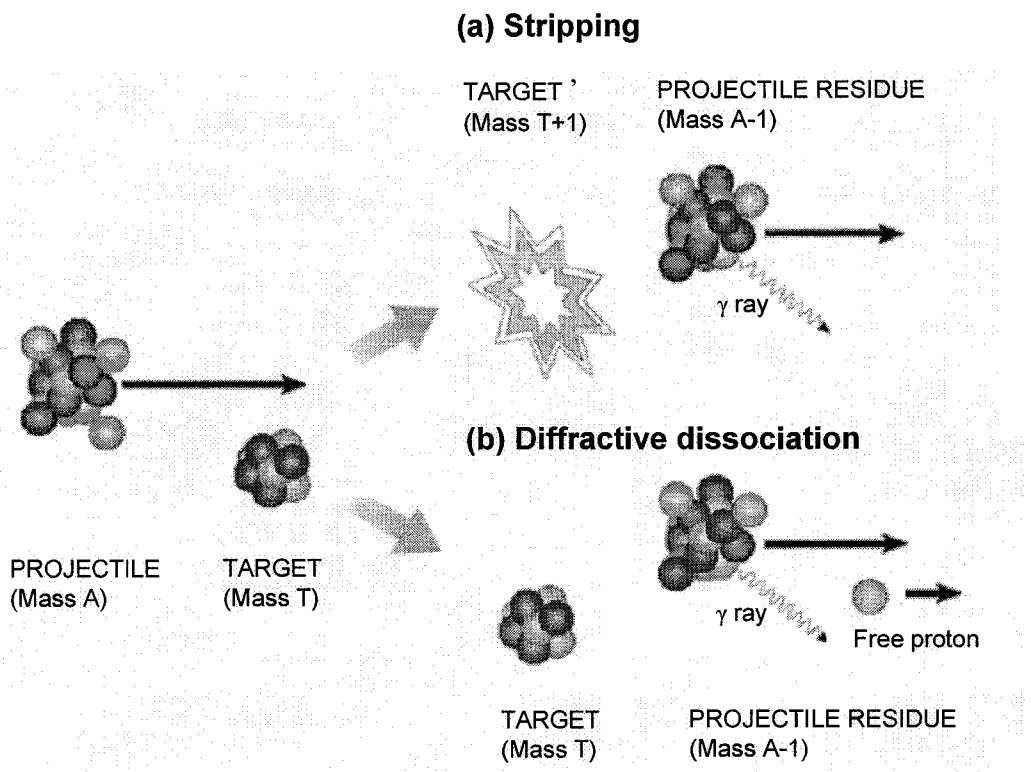

Figure 3.1 Schematic diagram of two modes of one-proton knockout: (a) stripping or inelastic breakup, and (b) diffractive dissociation or elastic breakup, adapted from [Ter06b].

To model the one-proton knockout cross section, two approximations are made based on the high incident energy of the projectile [Han03]:

(a) The "sudden approximation", due to the fact that the reaction takes place within a short reaction time. Given this approximation the reaction is assumed to proceed in one step, excluding the possibility of multi-step processes. The relative motion of the core with respect to the removed nucleon is considered frozen during the collision.

(b) The projectile and the ejected proton are not deflected from their straight-line trajectories by their interaction with the target. This assumption allows the application of the "eikonal" or optical limit of the Glauber theory [Tos99, Tos01].

Approximations (a) and (b) above justify the application of a "semi-classical theory" using elastic S matrices, also called profile functions [Tos99, Tos01]. The semi-classical approximation is generally valid in scattering theory [Mar69, p. 970] and is based on describing the reaction in terms of the impact parameter of the relative motion of projectile and target [Han03].

The final state of the system (Fig. 3.2(b)) is treated as a three-body problem of projectile residue ("core"), proton, and target. The elastic S matrices correspond to the core-target (S_C) and proton-target (S_P) interactions.

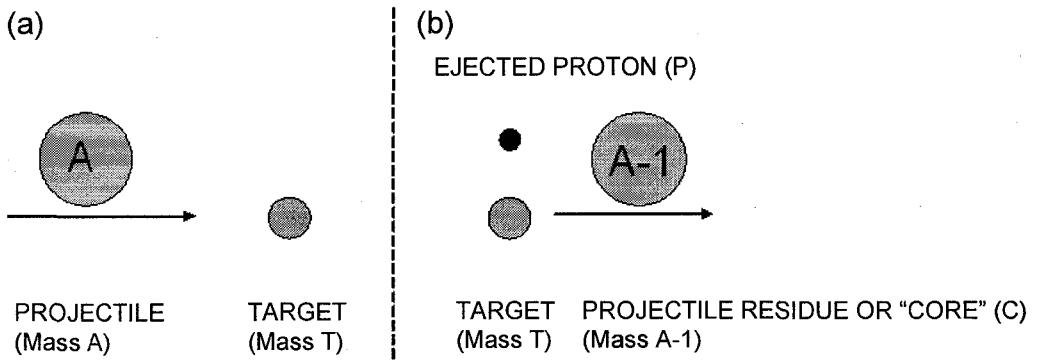

Figure 3.2 Schematic diagram of a one-proton knockout reaction indicating initial (a) and final (b) states. The final state (b) is modeled as a three-body problem of projectile residue ("core"), proton and target.

The proton-target interaction is parametrized by a conventional optical potential, which allows for the proton to be either absorbed or not by the target [Han03]. The proton-core interaction is treated with a Woods-Saxon potential, i.e., the proton is described by the independent-particle model.

Given that the projectile is in a state J^{π}, the core at I_C^{π}, and the removed nucleon at j, so that $\mathbf{J} = \mathbf{I_C} + \mathbf{j}$, the expression in Eq. 3.2 relates their angular momentum values:

$$| Ic - j | < J < Ic + j \tag{3.2}$$

The cross section for formation of the projectile residue or core at a given state I_c^{π} of spin I_C and parity π (Eq. 3.3), $\sigma(I_C^{\pi})$, consists of a sum over the allowed angular momentum transfers (represented by $n\ell j$) of the product of two terms: (1) the spectroscopic factor, C^2S ($n\ell j$, I_C^{π}), given by shell-model calculations and which reflects structure effects, and (2) the single-particle cross section, σ_{sp} ($n\ell j$, S_p^{eff}), given by the Glauber or eikonal model, which represents the reaction effects. Structure and reaction terms are therefore completely separated in one-proton knockout theory.

$$\sigma(I_C^{\pi}) = \sum_{n\ell j} C^2S(n\ell j, I_C^{\pi})\ \sigma_{sp}(n\ell j, S_p^{eff}) \tag{3.3}$$

In Eq. 3.3 the spectroscopic factor C^2S ($n\ell j$, I_C^{π}) for the removed proton with given single-particle quantum numbers $n\ell j$ with respect to the core state I_C^{π} is given by shell-model calculations [Bro07b] and is related to the occupation number of that particular single-particle orbital (nlj) in the final state (I_C^{π}) of the core [Bro02]. As the I_C^{π} state is generally not a pure single-particle state but a linear combination of them with coefficients a_i, the spectroscopic factors are the values $|a_i|^2$. Spectroscopic factors thus represent the overlap between the initial state wave functions of the projectile (of mass A) and of the I_C^{π} state of the core (of mass A-1).

The single-particle cross section, σ_{sp} ($n\ell j$, S_P^{eff}), for the removal of one proton from a single-particle state with quantum numbers $n\ell j$ in Eq. 3.3 depends on the state $n\ell j$ and on S_P^{eff}, the assumed effective separation energy of the proton. S_P^{eff} is the sum of the projectile's proton separation energy and the excitation energy of the I_C^{π} core state. The single-particle cross section is a combination of stripping and diffraction contributions. Equation 3.4 represents the stripping component of the single-particle one-proton knockout cross section derived by [Han03]:

$$\sigma_{sp} = \frac{1}{2j+1} \int d\vec{b} \sum_{m} < \varphi_{jm} | (1-|S_P|^2) |S_C|^2 | \varphi_{jm} > \qquad (3.4)$$

In Eq. 3.4, the proton-core relative-motion wave functions, $|\varphi_{jm}>$, were calculated in a Woods-Saxon potential with radius parameter r_0 = 1.25 fm and diffuseness parameter a = 0.7 fm, where the depth of the potential was adjusted to reproduce the separation energy of the proton in the initial state with given $n\ell j$. The S_P and S_C are elastic S matrices (or profile functions) for the proton-target and the core-target systems, respectively, and are expressed as functions of their individual impact parameters with the target. The method using S matrices involves plane waves.

The equation for σ_{sp} (Eq. 3.4) has a simple interpretation. It is the integral over impact parameter **b** and averaged over m substates of the joint probability of the proton interacting and being absorbed by the target, given by $(1-|S_P|^2)$, and of the core being elastically scattered by the target and therefore being left intact by the reaction, given by $|S_C|^2$. The quantity between brackets is the expectation value of this operator $(1-|S_P|^2)\ |S_C|^2$ evaluated in the phase space of the proton-core system, described by the wave function $|\varphi_{jm}>$.

The corresponding single-particle cross section for diffractive dissociation is similar to that of stripping [Tos01, Han03]; however, in diffractive breakup, the expression for the cross section contains a sum over all continuum relative motion final states of the proton-core system, as the proton is ejected rather than absorbed by the target.

Recent experimental data point to a systematic reduction in the experimental inclusive one-proton cross sections when compared with the theoretical ones. In one-proton knockout the reduction factor $R_s = \sigma_{inc}^{exp} / \sigma_{inc}^{theor}$ was found to be between 0.6 and 0.7 in a variety of moderately neutron-rich nuclei [Bro02, Han03, Gad04b, Ter04, Ter06a].

3.2.2 Two-Proton Knockout Theory

Two-proton knockout has recently been shown to occur as a direct reaction [Baz03b, War03, Tos04b, Yon06]. By using tabulated proton and neutron separation energies [ENS07] it can be shown that a direct two-proton removal is energetically favorable compared to the sequential removal of one proton at a time. For example, in the two-proton knockout of ^{32}Mg studied in this thesis, the one-proton separation energy, S_P, from ^{32}Mg to ^{31}Na is 21 MeV. The subsequent evaporation of one neutron from ^{31}Na (S_n = 4 MeV) is more energetically favorable than the evaporation of one proton from ^{31}Na (S_p = 18 MeV). Therefore, the sequential removal of two protons from ^{32}Mg is much less likely than their direct simultaneous two-proton knockout.

Two-proton knockout theory is based on the same principles as those of one-proton knockout. The main difference is that, while in single-nucleon knockout the cross section factors into a product of a reaction dynamics and a structure term, this does not generalize

in the same way to reactions involving the simultaneous removal of two nucleons. The transition amplitudes now mix the reaction and structure parts. As two protons are simultaneously removed, many two-particle components will contribute to the cross section within each total-angular-momentum channel.

One of the benefits of investigating two-proton knockout reactions is that they can serve to study whether the pairs of protons are or are not "correlated". Two protons are said to be uncorrelated [Tos99] when each of them moves independently of the other, under the influence of a common central field. The two protons are said to be correlated [Tos04b, Tos06a, Tos06b] when their movements are influenced by each other and their behavior deviates from the central-field description.

The cross section for removal of two uncorrelated protons (Eq. 3.5) is derived as an extension of the case for one-proton knockout (Eq. 3.4) [Tos99]:

$$\sigma_{\ell_1\ell_2} = \frac{1}{2\ell_1+1}\frac{1}{2\ell_2+1}\sum_{m_1m_2}\int d\vec{b} < \ell_1 m_1, \ell_2 m_2 | (1-|S_{P1}|^2)(1-|S_{P2}|^2)|S_C|^2 | \ell_1 m_1, \ell_2 m_2 > \quad (3.5)$$

The final state of the system (Fig. 3.3(b)) is treated as a four-body problem of projectile residue ("core"), two protons, and target. The elastic S matrices correspond to the core-target (S_C) and proton-target (S_{P1} and S_{P2}) interactions. In Eq. 3.5, the individual proton-core relative-motion wave functions $|\ell_1 m_1, \ell_2 m_2>$ are calculated by using Woods-Saxon potentials with depths adjusted so as to reproduce the proton separation energies. S_{P1} and S_{P2}, the elastic S-matrices corresponding to the interaction of each of the protons with the target, are functions of their individual impact parameters. Diffractive processes are assumed negligible or very small for the neutron-rich systems with very deeply bound protons.

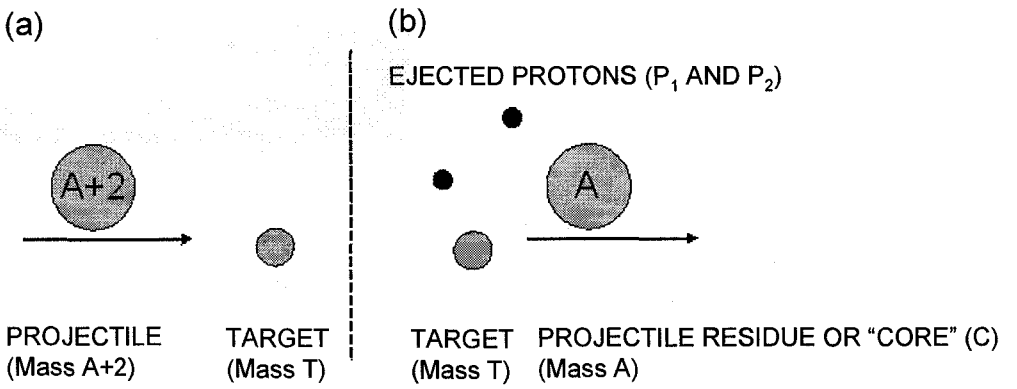

Figure 3.3 Schematic diagram of a two-proton knockout reaction indicating initial (a) and final (b) states. The final state (b) is modeled as a four-body problem of projectile residue ("core"), two ejected protons and the target.

Equation 3.5 can be interpreted as the integral over the two-dimensional impact parameter **b** and averaged over m-substates of the joint probability of the core being elastically scattered and of the two protons being absorbed by the target, thus representing the case of two-proton stripping. Equation 3.5 gives the cross section for the knockout of a given two-proton pair. To obtain the cross section to a given I_C^{π}, the two-proton knockout theory [Han03] incorporates the effect of all possible combinations of two-proton pairs. A first simple approximation, proposed by [Baz03b, Baz04] when studying two-proton knockout of neutron-rich Mg isotopes, consists in multiplying the two-proton cross section in Eq. 3.5 by a factor taking into account all possible pairs of valence protons, assuming that valence protons are uncorrelated. The paper by [Baz03b] addresses the two-proton knockout of ^{28}Mg, which has 12 protons with the configuration: $(1s_{1/2})^2(1p_{3/2})^4(1p_{1.2})^2(1d_{5/2})^4$, where there are 4 valence protons (p = 4) in the $1d_{5/2}$ orbital. [Baz03b] multiplied the two-proton cross section in Eq. 3.5 by the factor $N_p = p(p-1)/2$,

which is the number of different ways to pick two protons out of p valence protons. Multiplying the theoretical cross section in Eq. 3.5 by $N_p = 6$ resulted in a theoretical cross section which was within 20% of the experimental one.

The effects of two-proton correlations have been addressed in a number of recent papers [Tos04b, Tos06a, Tos06b]; these effects are incorporated by using "two-nucleon amplitudes", which are the equivalent of spectroscopic factors in the case of single-nucleon knockout.

Recent experimental data indicate that there is a systematic reduction in the experimental inclusive two-nucleon cross sections when compared to the theoretical ones. In two-nucleon knockout the reduction factor $R_s = \sigma_{inc}^{exp} / \sigma_{inc}^{theor}$ was found to be ~0.5 [Tos06b, Yon06].

Chapter 4

Experimental Equipment and Methods

4.1 Summary of the Experimental Technique

Two-step fragmentation/knockout reactions were used to produce neutron-rich isotopes of Mg, Na, and Ne in two experiments referred to as: E03053, carried out in December 2004, and E05122, carried out in September 2006, at the National Superconducting Cyclotron Laboratory (NSCL), Michigan State University (MSU). Figure 4.1 depicts the layout of the NSCL facility. In both experiments, the first reaction consisted in the fragmentation of a primary beam of ^{48}Ca at 140 MeV/A and 15 pnA[1] is produced by the Coupled Cyclotron Facility (CCF) on a light ^{9}Be target (also called the primary or transmission target). This primary fragmentation led to the production of secondary radioactive ion beams (RIB) at ~80-105 MeV/A that were purified and transported through the A1900 fragment separator followed by an analysis line; the secondary beams were purified by electromagnetic separation using dipole magnets and physical separation using slits (Section 4.2.2). The analysis line focused the secondary beams on a reaction target of ^{9}Be located at the center of the Segmented Germanium Array (SeGA) where they underwent fragmentation into final neutron-rich isotopes in the N ~ 20, A ~ 30 region emitted at ~75-100 MeV/A. The prompt γ-ray emission of the

[1] One particle nanoamp (pnA) ≅ $6x10^{9}$ particles per second (pps)

neutron-rich fragments was detected by SeGA in coincidence with the identification of the fragments at the focal plane of the S800 spectrograph.

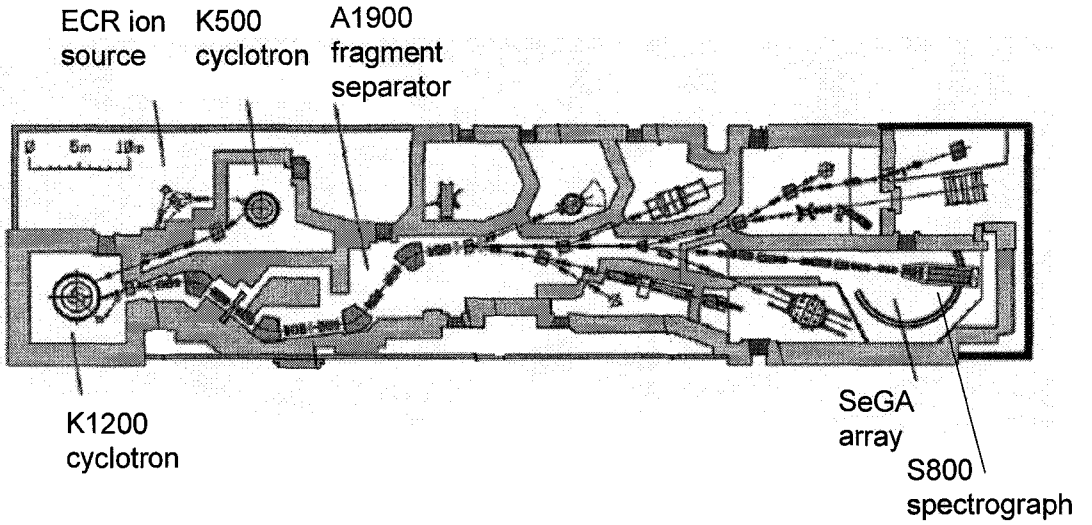

Figure 4.1 Floor plan of the National Superconducting National Laboratory, including the Electron-Cyclotron Resonance (ECR) ion source, the Coupled Cyclotron Facility (K500 and K1200 cyclotrons), the A1900 fragment separator, the S800 spectrograph, and the SeGA array [MSU07].

4.2 Equipment

4.2.1 The SC-ECR Ion Source and the Coupled Cyclotron Facility (CCF)

The primary beam of ^{48}Ca was produced by the Coupled Cyclotron Facility (CCF), fed by a superconducting electron-cyclotron resonance ion source (SC-ECR). In the SC-ECR, an isotopically pure amount of ^{48}Ca was vaporized and heated by microwaves until it achieved the plasma phase where electrons and nuclei are separated from each other. An intense magnetic field generated by superconducting coils inside the SC-ECR is designed to prevent the nuclei from contact with the walls so that they remain ionized. Ions with selected charge states were extracted from the SC-ECR and transported to the first cyclotron of the CCF.

The coupling of the two cyclotrons (K500 and K1200) at the CCF is designed to produce primary beams with energies higher than possible with only one accelerator. In addition, the cyclotrons at the CCF are built with superconducting magnets, which achieve high magnetic fields using compact equipment. The cyclotron (Fig. 4.2), invented by E. O. Lawrence in 1931 [Law32], uses – in its simplest form – a single static magnetic field which causes ions to travel circular paths on a perpendicular plane according to the Lorentz force F = qvB, where q is the charge of the ion, v its velocity, and B the intensity of the magnetic field. In addition, a radio-frequency (RF) modulated electric field periodically imparts kinetic energy to the ions, accelerating them so that they describe orbits with increasingly larger radii. The principle of operation of the cyclotron provides that all ions take the same time to describe a complete circular orbit, regardless of their radii (and hence their kinetic energy), a straightforward consequence of the Lorentz force, and assuming that the mass-to-charge ratio (m/q) of the particles is independent of their velocity. As the particle velocity increases, relativistic effects cause the mass of the particle to increase as its velocity increases, so that the time to describe a circular orbit (regardless of its radii) can be kept constant by allowing B to increase as a function of the radius [Har74]; additional modifications to the cyclotron design have been developed [Har74] to achieve stable operation at relativistic velocities.

From the Lorentz force it also follows that the maximum energy imparted by a cyclotron to an ion of charge q and mass number A is $E = K\, q^2/A$, where E is in MeV and K a constant characteristic of each cyclotron. The constant K depends on the size and magnetic field intensity $|\mathbf{B}|$ of the cyclotrons and it takes the values of 500 and 1200 at the Coupled Cyclotron Facility.

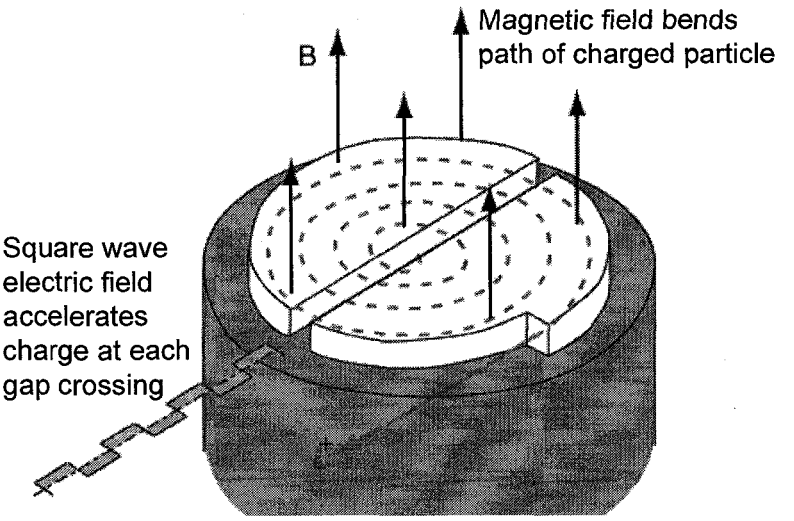

Figure 4.2 Schematic diagram of a cyclotron, adapted from [Nav05].

The ions generated by the SC-ECR are injected at the center of the K500 which accelerates them to an energy of 10-20 MeV/A (or 15-20% of c). As the ions leave the first cyclotron, a stripping foil increases their charge q before injection into the second cyclotron. The K1200 is then able to accelerate the higher-charged ions to an energy of up to 200 MeV/A, or more than 55% of c.

4.2.2 The A1900 Fragment Separator

The A1900 (Fig. 4.3) [Mor97, Mor03] is an ion-optical device that is used to transport, separate and purify secondary-beam components by a sequential in-flight electromagnetic separation using four large dipole magnets, which bend the beam by approximately 45° each, and provides physical separation using slits and the limited momentum acceptance of the device ($\Delta p/p$ of 5%, corresponding to an angular

acceptance $\Delta\Omega$ of 8 msr). The dipole magnets deflect ions by different radii ρ depending on their momentum-to-charge ratio according to the expression $B\rho = p/q$, where $B\rho$ is the magnetic rigidity of a dipole magnet in units of Tesla-meters (T-m), allowing for the separation and selection of desired secondary beams. Figure 4.3 includes the positions of Images 1, 2 (intermediate image) and 3, as well as of the focal plane (FP) and the extended focal plane (XFP). The A1900 also contains eight sets of quadrupole triplet magnets, which help focus the beam throughout the beamline, implementing an "achromatic ion-optical mode", where the dispersion in momentum is maximum at the intermediate image (along the horizontal direction, where the momentum can be measured), and cancelled at the focal plane.

Two detectors provide the start and stop signals for time-of-flight (TOF) measurements in the A1900: a thin plastic scintillator (0.13-mm thick, 350-mm horizontal, 60-mm vertical) located at the intermediate image, and a thick plastic scintillator at the A1900 focal plane (100-mm thick).

At the intermediate image, two position-sensitive parallel-plate avalanche counters (PPACs) measure positions and momenta of traversing ions. Each PPAC is a proportional gas-filled detector consisting of a pair of parallel plates, with dimensions of 400-mm horizontal by 100-mm vertical. At the A1900 focal plane, another pair of PPACs, with dimensions of 100x100 mm^2, is also used for momentum tracking of the secondary beams.

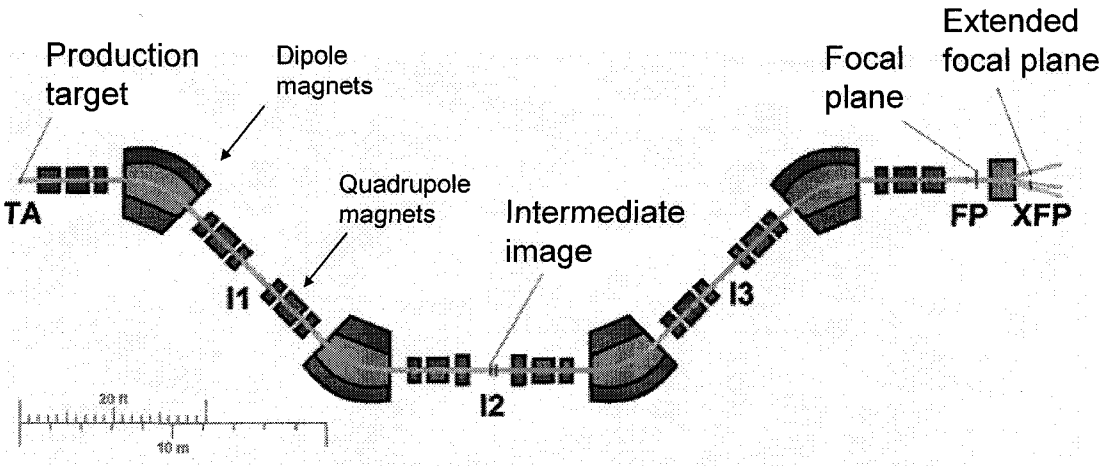

Figure 4.3 Schematic diagram of the A1900 fragment separator, adapted from [MSU07]. The A1900 contains four dipole magnets and eight sets of quadrupole triplets. The figure indicates the location of the production target (TA), images I1, I2 and I3, the focal plane (FP), and the extended focal plane (XFP). A wedge-shaped energy degrader is located at the intermediate image (I2).

At the intermediate image there is a wedge-shaped aluminum energy degrader, with a thickness of 150 mg/cm^2 (E03053) or 300 mg/cm^2 (E05112). The "wedge" is used for separation of incoming secondary beams according to their different Z, based on their differential energy loss ΔE through the aluminum material, as explained in Section 4.3. A thicker wedge is designed for achieving a higher degree of separation and therefore a higher purity of the secondary beams.

In the A1900 focal plane, a silicon PIN detector (0.5-mm thick, 50x50 mm^2) located between the two PPACs provides a ΔE signal used in the particle identification of the secondary beams. At the end of the A1900 separator (Fig. 4.3) there is an additional scintillator detector located at the extended focal plane (XFP); the TOF between the XFP

scintillator and another scintillator (E1) located at the final S800 focal plane is used for particle identification.

4.2.3 The Analysis Line and the S800 Spectrograph

The Analysis Line

The "analysis line" is the part of the beamline that is located upstream from the S800 spectrograph (Fig. 4.4) and is used to measure and characterize the incoming secondary radioactive beams and to tune them on the secondary ^{9}Be reaction target.

The analysis line was operated in "focused-mode", where the secondary beams were focused at the ^{9}Be target and dispersed at the final S800 focal plane. In the analysis line there are two pairs of dipole magnets with maximum rigidity of 5 T-m on both sides of the intermediate image. A 0.25-mm thick scintillator detector located at the object position (OBJ) (Fig. 4.4) is used for TOF measurements for final fragment identification at the S800. At the intermediate image (IM) of the analysis line there are two tracking PPAC detectors which provide position and angle measurements in both the dispersive and non-dispersive planes; the IM also contains momentum slits.

The S800 Spectrograph

The S800 spectrograph (Fig. 4.4) [Baz03a] is a high energy-resolution ($\Delta E/E$ of 1/10,000) and large acceptance ($\Delta p/p$ of 6%, corresponding to an angular acceptance $\Delta\Omega$ of 20 msr) device, spanning from the secondary ^{9}Be target to the S800 focal plane (Fig. 4.5). The solid angle acceptance is an ellipsoid of 7^{o} in the dispersive plane by 10^{o} in the

non-dispersive plane. The S800 spectrograph consists of two dipoles which bend the beam by 75° each.

At the focal plane of the S800 (Fig. 4.5) [Yur99] there are two position-sensitive cathode readout drift chambers (CRDCs) separated by 1 meter, which measure positions and angles in the focal plane and provide particle trajectory information; they have a position resolution of 0.5 mm in both the dispersive and non-dispersive directions. The CRDCs are filled with a mixture of 80% CF_4 (Freon 14) and 20% iC_4H_{10} (isobutane) at a pressure of 50 torr and they cover an area of 56 cm in the dispersive plane by 26 cm in the non-dispersive plane. The CRDCs are followed by a one-meter-thick ionization counter (IC) which measures energy loss ΔE and therefore identifies the Z of the fragments. The IC is filled with P10 gas at a pressure of 140 torr. Finally, the focal plane contains a stack of four plastic scintillators of different thicknesses. In our experiments, only the first, 5-cm-thick scintillator (E1) was used as the S800 trigger and also as one of the signals for time-of-flight (TOF) measurements.

The ionization counter (IC) of the S800 focal plane (FP) measures ΔE used for particle identification. The time-of-flight (TOF) used for the identification of final fragments is measured between the first 3-mm-thick scintillator (E1) in the S800 focal plane and either the scintillator located at the extended focal plane of the A1900 separator (XFP), or the one located at the object of the S800 spectrograph (OBJ) (Fig. 4.4).

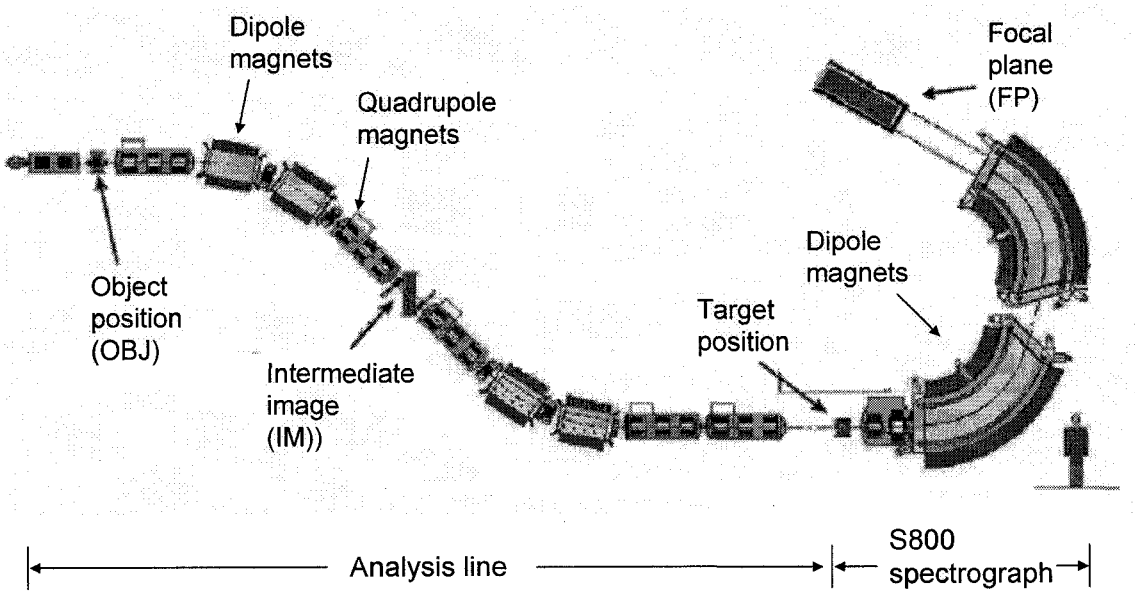

Figure 4.4 Schematic diagram of the analysis line and the S800 spectrograph, adapted from [Baz03a]. The figure includes the locations of the object (OBJ), intermediate image (IM), target, and focal plane (FP), as well as the dipole and quadrupole magnets.

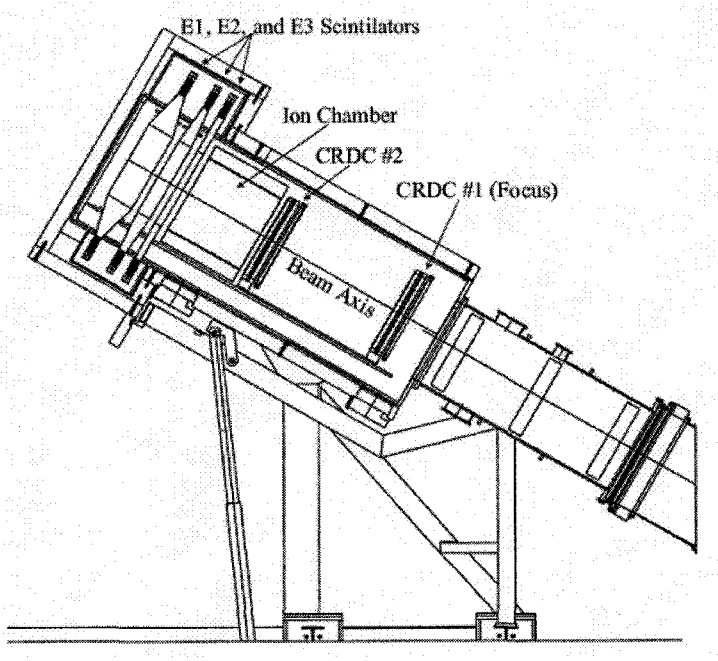

Figure 4.5 Schematic diagram of the S800 focal plane, adapted from [Yur99].

4.2.4 The Segmented Germanium Array (SeGA)

The γ-ray spectroscopy of fast-moving neutron-rich fragments presents two challenges: (1) low γ-ray intensities due to the low fragment production rates, which requires large solid angles and high energy-resolution detectors, and (2) the need for good Doppler correction of the γ-rays due to the relativistic velocities (v/c ~ 0.40) of the γ-emitting fragments. The Segmented Germanium Array (SeGA) at the NSCL was designed to address these two challenges, and it consists of high energy-resolution germanium (Ge) detectors, which are segmented to provide accurate determination of the position of first interaction of the γ-ray with the detector, allowing for an improved Doppler correction capability with respect to non-segmented detectors, and therefore increased energy resolution.

SeGA (Fig 4.6) is an array of 32-fold segmented coaxial single-crystal high-purity germanium (HPGe) detectors [Mue01]. The Ge crystal for each of the SeGA detectors has a diameter of 70 mm, and a length of 80 mm. The outer surface of each of the detectors is electronically divided into 32 segments: eight disks along the longitudinal axis, all of which are also divided into four equal sectors (Fig. 4.7).

The energy resolution (ΔE_γ^0) of the Doppler-reconstructed γ-ray spectra depends on three contributions: (1) the uncertainty in the velocity ($\Delta\beta$) of the γ-emitting moving fragments due to their different energy losses while slowing down within the target thickness, (2) the uncertainty in the emission angle ($\Delta\theta$) of the γ-ray due to both the finite opening angle of the detectors and the inherent uncertainty in the emission angle caused by the fragmentation reaction, and (3) the intrinsic energy resolution of the γ-ray detectors (ΔE_{intr}) which is on the order of ~2 keV at 1.3 MeV, as indicated in Eq. 4.1:

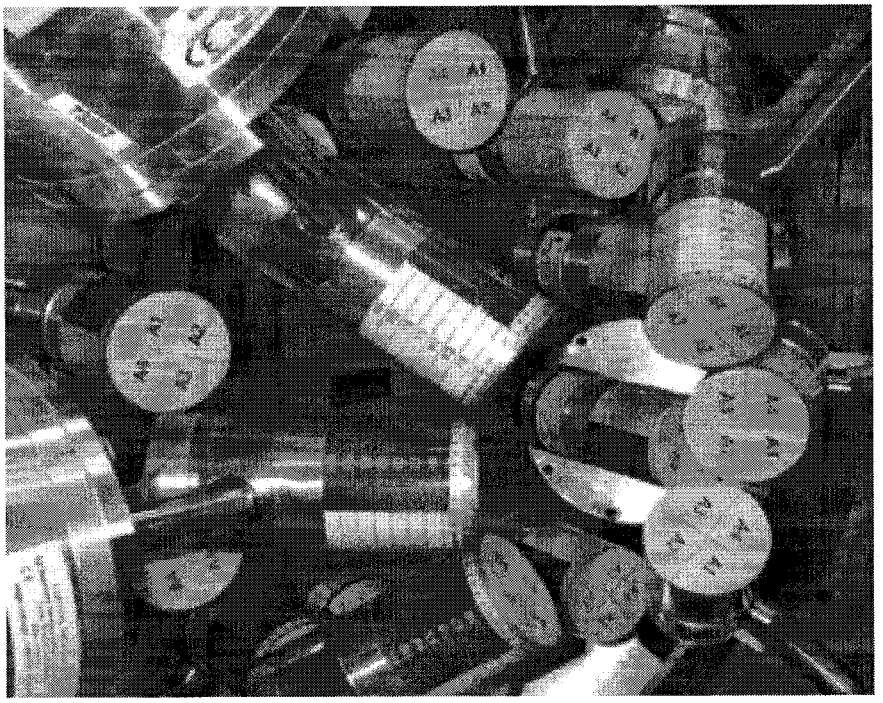

Figure 4.6 Picture of the Segmented Germanium Array (SeGA).

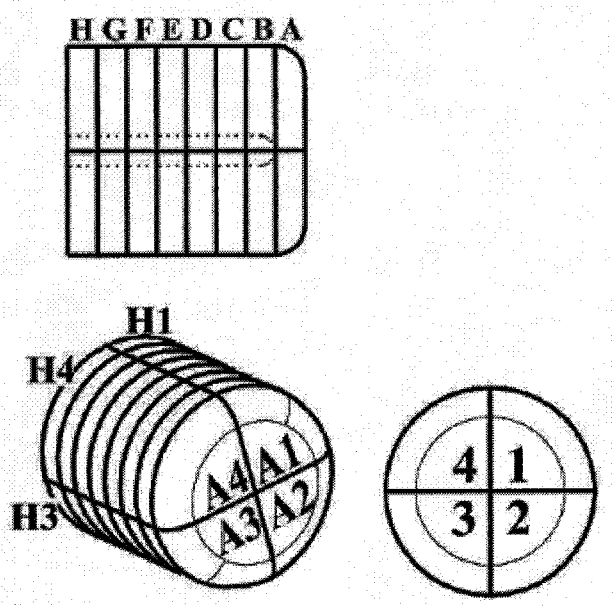

Figure 4.7 Schematic diagram of a SeGA crystal, adapted from [Mue01]. The cylindrical high-purity germanium crystal is electronically segmented into eight disks, labeled A-H, and four sections, labeled 1-4, giving a total of 32 segments per detector. Each cylindrically-shaped germanium crystal has dimensions of 8 cm (height) x 7 cm (diameter).

$$\left(\frac{\Delta E_\gamma^0}{E_\gamma^0}\right)^2 = \left(\frac{\beta \sin\theta}{1-\beta\cos\theta}\right)^2 (\Delta\theta)^2 + \left(\frac{\beta - \cos\theta}{(1-\beta^2)(1-\beta\cos\theta)}\right)^2 (\Delta\beta)^2 + \left(\frac{\Delta E_{intr}}{E_\gamma}\right)^2 \quad (4.1)$$

The two dominant factors contributing to the energy resolution (ΔE_γ^0) in Eq. 4.1 are the uncertainties in β and θ. In Eq. 4.1, the E_γ and ΔE_{intr} on the right-hand side are the energy and its uncertainty of the γ rays referred to the laboratory frame. On the left-hand side of Eq. 4.1, the E_γ^0 and the ΔE_γ^0 are Doppler-reconstructed γ-ray energies (i.e., with respect to the γ-emitting projectile reference frame).

The high degree of segmentation allows for a reduced effective opening angle of the detectors ($\Delta\theta$) and therefore a more precise localization of the photons interacting with the SeGA detectors, contributing to an improved energy resolution of the Doppler-reconstructed γ-ray spectra. The array is designed so that the detectors can be placed at variable distances from the central target position, which permits selection of a balance between competing high efficiency and high energy resolution. In this work, the detectors were located at ~25 cm from the target position, and arranged in two rings, at 37° and 90° angles (Fig. 4.8).

Energy and Efficiency Calibrations

Each SeGA detector underwent energy calibration of its central contact and of all of its segments. The central contact was calibrated by using a number of standard radioactive sources (^{56}Co, ^{60}Co, ^{152}Eu, ^{226}Ra). The energy calibration of each of the 32 individual segments was performed by applying an automated technique described elsewhere [Hu02], and it was done relative to the central contact.

The absolute efficiency of an array is the ratio of the number of full-energy γ rays detected, vs. the number of γ rays emitted by the source. To determine the absolute efficiency of SeGA we used a ^{152}Eu source of known strength placed at the target position of SeGA. The ^{152}Eu source (labeled Z2707 at MSU) had a reported activity of 3.131×10^5 (±1.4%) Bq on May 1, 1978. Using the ^{152}Eu reported half-life of 13.537(6) years [Fir96], we deduced the activity of the source at the time of the experiment. The ^{152}Eu γ-ray energies and relative intensities (or branching ratios) were taken from [Fir96 (Vol. II, App. C)], and are summarized in Table 4.1.

The absolute photo-peak efficiency curves of the 37° and 90°-rings separately, and for the 2004 and 2006 experiments are given by the solid lines joining the experimental points in Figs. 4.9 through 4.12. These figures also include Lorentz-boosted efficiencies (dashed lines); an explanation of the Lorentz-boosted efficiencies is given next. Detailed calculations used to obtain the efficiency calibration curves are given in Appendix A.

Table 4.1 Energies and relative intensities of γ-ray transitions in ^{152}Eu, used for energy and efficiency calibration purposes, adapted from [Fir96].

Eγ (keV)	Iγ (%)
121.7817(3)	28.37(13)
244.6975(8)	7.53(4)
344.2785(13)	26.57(11)
411.1165(13)	2.238(10)
444.0	3.125(14)
778.9045(24)	12.97(6)
867.378(4)	4.214(25)
964.1	14.63(6)
1085.836(9)	10.13(5)
1112.074(4)	13.54(6)
1408.011(4)	20.85(9)

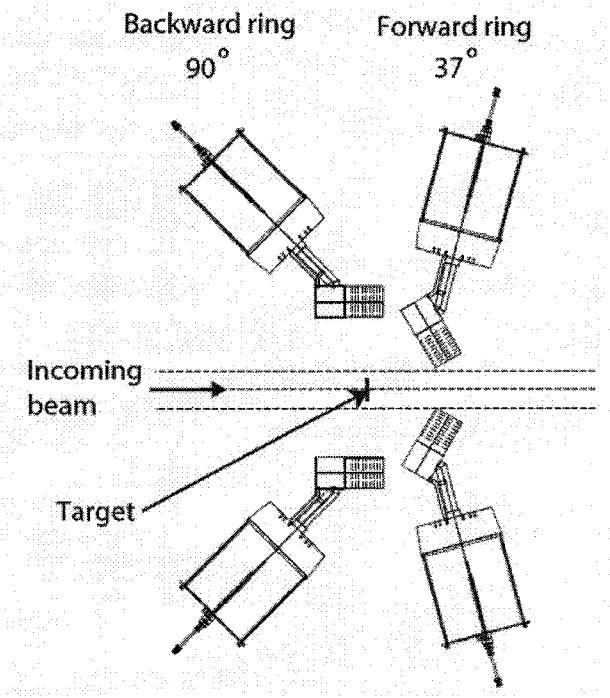

Figure 4.8 Diagram of SeGA indicating the distribution of the detectors in two rings at 37 and 90 degrees, adapted from [Din05].

Relativistic Corrections to Efficiency Calibrations: Lorentz Boost and Doppler Shift

Photons emitted isotropically by a source moving at relativistic speeds in the laboratory are found preferentially in the forward direction in the laboratory reference frame. This Lorentz boost factor f, which depends on β and θ, is given by [Ale78]:

$$f = \frac{1-\beta^2}{(1-\beta\cos\theta)^2} \tag{4.2}$$

where $\beta = v/c$ is the velocity of the γ-emitting fragment, and θ is the angle between the direction of movement of the fragment and the line connecting the point of γ-ray emission with the point of detection; a schematic diagram of the γ-ray detection by a SeGA detector is represented in Fig. 4.13. The application of the Lorentz-boost factor gives rise to an angle-dependent correction to the source efficiency calibration (dashed lines in Figs. 4.9 through 4.12).

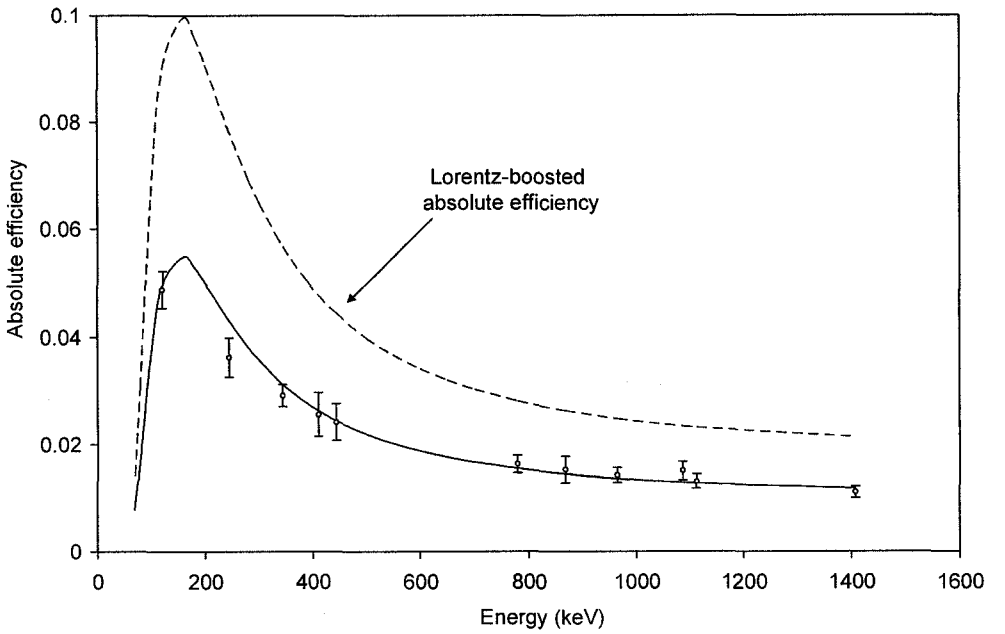

Figure 4.9 Absolute efficiency calibration of the SeGA 37^0-ring in the E03053 experiment (solid line), and its Lorentz-boosted correction for $\beta = 0.40$ (dashed line).

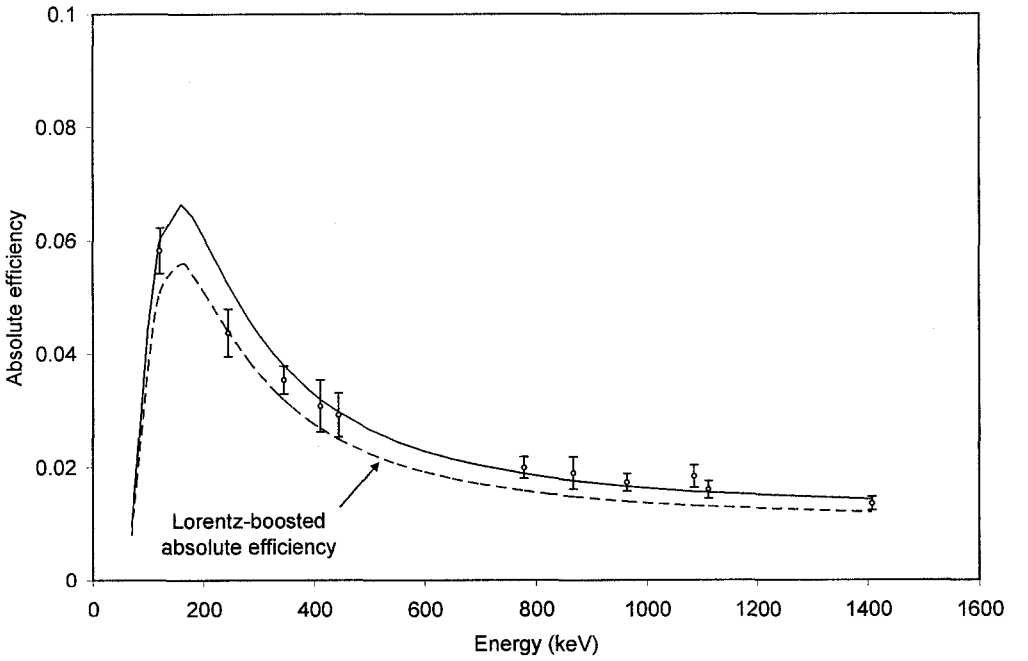

Figure 4.10 Absolute efficiency calibration of the SeGA 90^0-ring in the E03053 experiment (solid line), and its Lorentz-boosted correction for $\beta = 0.40$ (dashed line).

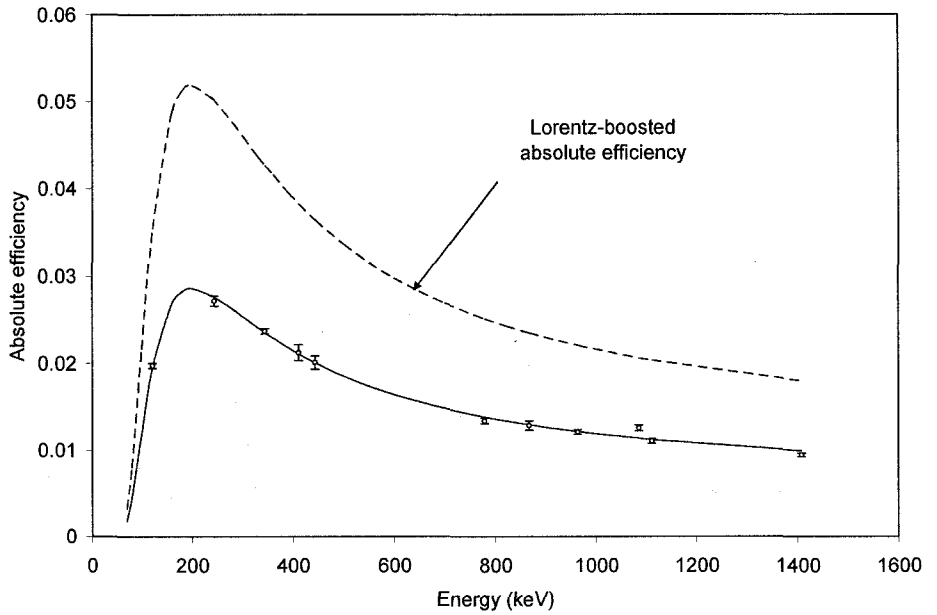

Figure 4.11 Absolute efficiency calibration of the SeGA 37^0-ring in the E05122 experiment (solid line), and its Lorentz-boosted correction for $\beta = 0.40$ (dashed line).

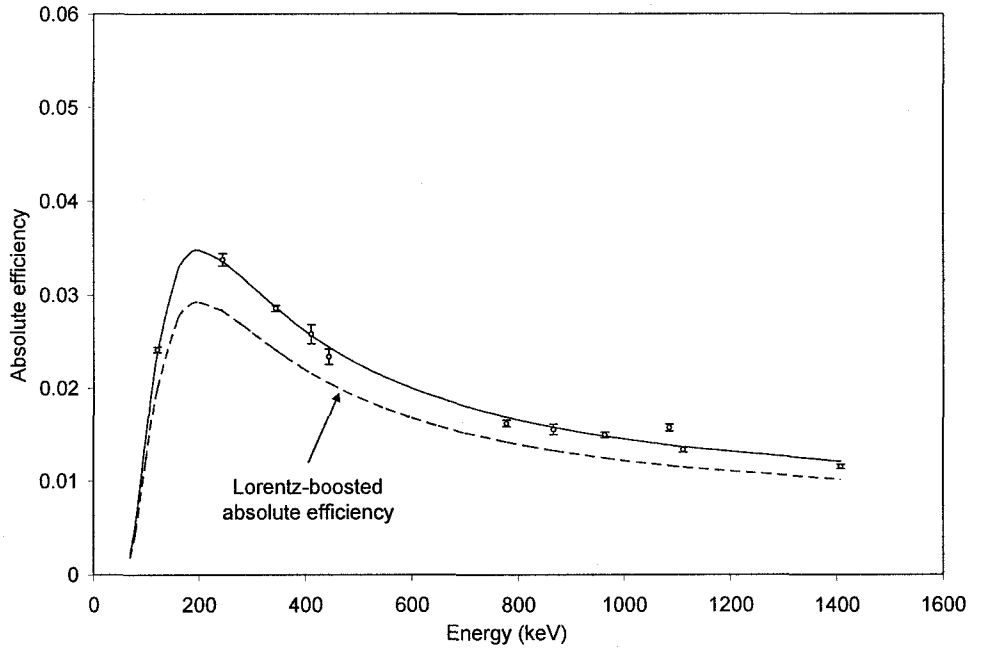

Figure 4.12 Absolute efficiency calibration of the SeGA 90^0-ring in the E05122 experiment (solid line), and its Lorentz-boosted correction for $\beta = 0.40$ (dashed line).

A γ ray emitted from a moving source also undergoes a Doppler shift. The observed Doppler-shifted energies are given by [Ale78]:

$$E_\gamma(\theta) = \frac{E_\gamma^0 (1-\beta^2)^{1/2}}{1-\beta\cos\theta} \tag{4.3}$$

where $E_\gamma(\theta)$ is the Doppler-shifted energy measured by the γ-ray detectors in the laboratory reference frame respect to which the fragments are moving, $\beta = v/c$ is the reduced velocity of the γ-emitting fragments, θ the angle of γ-ray emission with respect to the velocity vector **v** of the fragments, as in Eq. (4.2) above, and E_γ^0 the energy of the γ-ray transition connecting two nuclear levels, measured with respect to the reference frame attached to the moving γ-emitting fragment. Appendices A and C include calculated Lorentz-boost and Doppler-shift factors for the experiments in this thesis.

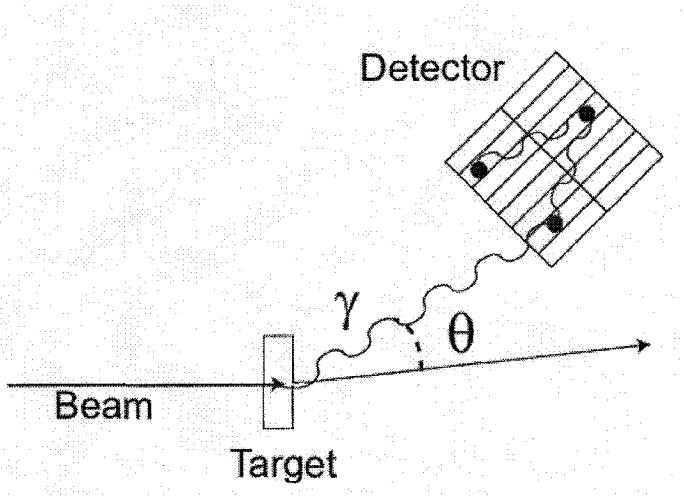

Figure 4.13 Schematic diagram of the interaction of a γ ray with a SeGA detector, indicating the angle of emission θ used in the Lorentz-boost and Doppler-shift corrections, adapted from [Din05].

4.3 Charged-Particle Detection and Identification

The nuclei of interest (secondary beams and fragments) are transported through the system as fully-ionized particles so that their atomic number Z coincides with their charge q. These charged particles interact with detectors located along the experimental beamline. The charged-particle detectors are used to measure energy loss (ΔE) through a given detector thickness, and time-of-flight (TOF) between two detectors. These measurements are used in combination with $B\rho = p/q$ selection achieved by the magnetic dipoles along the system to uniquely identify the fragments in terms of their Z and A.

Charged-particle detection is based on the Bethe formula [Kno00, p. 31] for the linear stopping power or rate of energy loss S of charged particles traversing a given material, defined as $S = - dE/dx$. The Bethe formula is expressed as:

$$-\frac{dE}{dx} = \frac{4\pi e^4 Z^2}{m_o v^2} NB \qquad (4.4)$$

where v and Z are the velocity and charge of the moving charged particle, m_o and e the electron rest mass and charge, respectively, N the number density of atoms in the detector material, and B a term which depends on the atomic number of the detector material Z_d, the average excitation and ionization potential of the detector material I, and the velocity of the moving charged particles v. For the purposes of charged-particle detection in a given detector material, it is sufficient to assume that the specific energy loss of charged particles is roughly proportional to Z^2/v^2 (Eq. 4.4).

Particle Identification with the ΔE-TOF Method

The particle identification (PID) spectra were generated by representing the ΔE of the fragments that was measured by the ionization chamber (IC) located at the S800 focal plane in the vertical axis, vs. the time-of-flight (TOF) of the fragments measured from the S800 object scintillator (OBJ) located at the beginning of the "analysis line", and the E1 scintillator (which is also the S800 trigger) located at the S800 focal plane in the horizontal axis.

The magnetic rigidity Bρ of the S800 dipoles achieves separation of the fragments according to approximately their A/Z ratio, so that a TOF spectrum at the S800 focal plane separates fragments according to this ratio. Since the ΔE measured at the IC is approximately proportional to the Z^2 of the fragments as given by the Bethe formula (Eq. 4.4), a ΔE-TOF spectrum results in the complete separation of regions with unique Z and A values. Figure 4.14 is a ΔE-TOF spectrum of fragments obtained by the secondary cocktail beam composed of ^{32}Mg/^{33}Al/^{35}Si beams in E03053.

4.4 Experimental Determination of Cross Sections

The inclusive cross section (σ_{inc}) for a particular reaction is defined (Eq. 4.5) as the ratio between the number of fragments produced (N_f) and the product of the number of incident beam particles (N_b) and the atom density per cm^2 of the target (N_t):

$$\sigma_{inc} = \frac{N_f \text{ (particles)}}{N_b \text{ (particles)} \; N_t \text{ (particles/cm}^2\text{)}} * 10^{27} \text{ mb/cm}^2 \qquad (4.5)$$

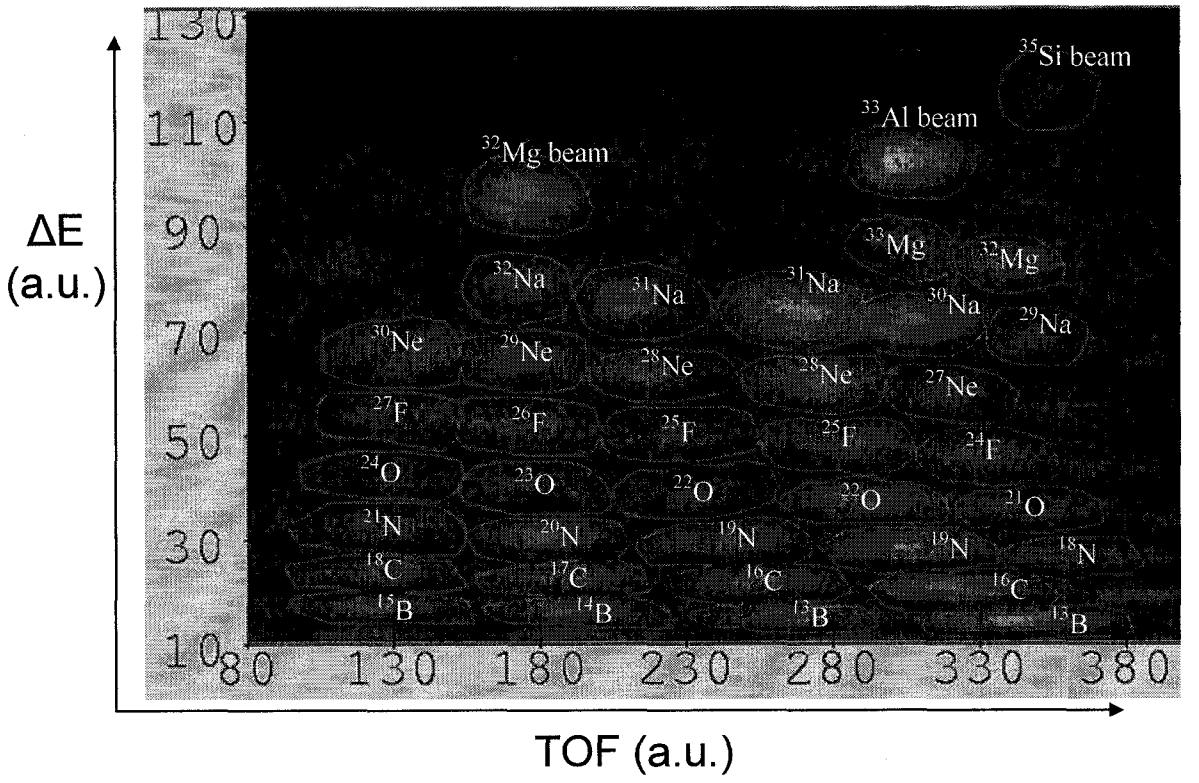

Figure 4.14 Particle identification (ΔE vs. TOF) spectrum. The secondary beams were ^{32}Mg, ^{33}Al, and ^{35}Si.

Therefore, the σ_{inc} in the expression above has units of area. The factor 10^{27} mb/cm^2 in Eq. 4.5 is used so that the final units of the inclusive cross section σ_{inc} are millibarns (1 mb = 10^{-27} cm^2).

The number of fragments N_f is calculated as:

$$N_f = \frac{N_{kn}}{lt_{kn}\, eff_{kn}\, eff_{gat} K_{CRDC}} \tag{4.6}$$

To obtain the number of fragments N_f in Eq. 4.6 above we use the total number of a given type of fragment detected in the particle identification plot (PID) of the knockout run (N_{kn}). A knockout run takes place when the S800 spectrograph is set to transport the fragments produced by the interaction of secondary beams with the secondary ^{9}Be target located at the center of SeGA. The number N_{kn} needs to be corrected by dividing it by the

product of the live time lt_{kn} (to account for the time lost during electronic data collection), the efficiency of the knockout run (eff_{kn}), and the efficiency (eff_{gat}) that results from gating on the secondary beam two-dimensional TOF spectrum; the calculations of the efficiencies will be explained later. Eq. 4.6 includes an additional correction factor K_{CRDC} (a number between 0 and 1) due to the limited acceptance of the S800 spectrograph, measured at the first cathode readout drift chamber (CRDC) detector located at the S800 focal plane. A sample CRDC spectrum is shown in Appendix B. The K_{CRDC} value for a particular fragment is estimated by analyzing the corresponding shape of the CRDC Gaussian distribution, in particular by comparing the CRDC shape of a given fragment to that of a fragment with $K_{CRDC} \sim 1$, that is, a fragment which was almost fully collected within the S800 acceptance.

The expression for the number of beam particles N_b is:

$$N_b = \frac{N_{unr}}{lt_{unr}\, eff_{unr}} \frac{scaler_{kn}}{scaler_{unr}} \tag{4.7}$$

To obtain the number of beam particles N_b in Eq. 4.7 above, we use one of the unreacted runs and measure the number of secondary beam particles in the PID spectrum. An unreacted run is carried out by tuning the S800 spectrograph magnetic rigidity, Bρ, to transport the secondary beams (no secondary ^{9}Be target) and not the fragments. To normalize this number to the same time as the knockout run, we multiply it by the ratio of "scalers" of knockout vs. unreacted runs ($scaler_{kn}$ and $scaler_{unr}$). The scalers are numbers of counts registered by the object scintillator (OBJ) placed at the entrance of the analysis line of the S800 spectrograph. The denominator includes the live time (lt_{unr}) and the efficiency (eff_{unr}).

The number of particles in the secondary ^{9}Be target (Eq. 4.8) is calculated as a function of the target density ρ_t, Avogadro's number N_A, and the atomic weight of the ^{9}Be target AW_t:

$$N_t\ (\text{particles/cm}^2) = \frac{\rho_t\ (\text{g/cm}^2)\ N_A\ (\text{particles/mol})}{AW_t\ (\text{g/mol})} \tag{4.8}$$

Particle Identification Efficiency

Particle identification (Section 4.3) was achieved through data on ΔE measured at the S800 ionization counter (IC), and the TOF between the object (OBJ) and the E1 scintillator located at the S800 focal plane; it also used particle trajectory information obtained by the CRDC detectors at the S800 focal plane, and the PPAC detectors at the intermediate image of the analysis line. The efficiency of particle identification of both the knockout and unreacted runs (eff_{kn} and eff_{unr}) is the product of the efficiencies of the timing scintillators involved, the ionization counter (IC), and the CRDCs and PPACs used in the reconstruction of the particle trajectories. The IC and the E1 detectors are assumed 100% efficient for the light fragments of interest; however, the object scintillator does contribute to the efficiency losses. To estimate these efficiency losses in practice, we used the data-acquisition software SpecTcl [Spe07] to make a selection or "gate" of certain events registered at the ionization counter (IC) located at the S800 focal plane. While the IC spectrum contains data points corresponding to all the fragments detected at the S800 focal plane, the "gate" is intended to select only those fragments corresponding to the inclusive cross section that we are measuring; N_{IC_gate} is the number of counts in this gate. The data acquisition software allows us to generate two-dimensional PID spectra restricted to the events contained in the gate that we previously

selected in the IC spectrum, and we can measure the number of counts in this "gated" PID spectrum, N_{gated_PID}. The efficiency eff_{kn} is then the ratio of $N_{gated\_PID}/N_{IC\_gate}$. This efficiency corresponds to the combination of detectors and reconstruction efficiency, which includes the object scintillator, CRDC and tracking PPAC detector efficiencies.

There was an additional efficiency correction (eff_{gat}) that was needed in the experiments employing a secondary cocktail beam because of the need to separate the contributions from different secondary beam components to the production of a given final fragment. The two-dimensional spectrum of the secondary beams has, on the horizontal axis, the TOF measured from the extended focal plane scintillator (XFP) of the A1900 fragment separator to the E1 scintillator at the focal plane of the S800. The vertical axis contains the dispersive angle θ at the intermediate image of the analysis line. This TOF of the secondary beams uses corrections given by the PPAC detectors located at the intermediate image of the analysis line. To estimate eff_{gat}, we created a "gate" or selection of events in the two-dimensional TOF spectrum of the secondary beam particles to isolate those events corresponding to a given type of secondary beam; the number of counts is N_{IC_gate}. We then applied this gate to the two-dimensional PID spectrum of the fragments at the S800 focal plane and measured the number of fragments produced by that particular type of secondary beam particles; the number of counts in this "gated" spectrum is N_{gated_TOF}. The efficiency eff_{gat} is the ratio $N_{gated\_TOF}/N_{IC\_gate}$. The efficiency calculations for experiments E03053 and E05122 are included in the cross section tables in Appendix B.

Partial Cross Sections

The partial cross sections are the individual probabilities of populating the ground state and each of the different nuclear excited states, where the sum of all the partial cross sections is equal to the inclusive cross section for formation of a given fragment. The partial cross sections to different excited states and the ground state (σ_i) are defined as:

$$\sigma_i = b_i \, \sigma_{inc} \tag{4.9}$$

where the b_i's are the fractional populations or branching ratios to the ground and excited states. The fractional population (b_i) of a given state is obtained by balancing the γ-ray intensities feeding and decaying away from this state; an estimate of the uncertainty in b_i is derived from the uncertainty in the γ-ray intensities (Appendix C) used in its calculation. The fractional population of the ground state is equal to one minus the sum of all other fractional populations of the excited states.

Error Estimates of Cross Sections

The expression used to estimate the uncertainty in the inclusive cross section σ_{inc} of Eq. 4.5 is:

$$\frac{\Delta\sigma_{inc}}{\sigma_{inc}} = \sqrt{\left(\frac{\Delta N_f}{N_f}\right)^2 + \left(\frac{\Delta N_b}{N_b}\right)^2 + \left(\frac{\Delta N_t}{N_t}\right)^2} \tag{4.10}$$

The largest contributor to the uncertainty, $\Delta\sigma_{inc}/\sigma_{inc}$, is $\Delta N_f/N_f$, which is dominated by $\Delta K_{CRDC}/K_{CRDC}$. The term $\Delta K_{CRDC}/K_{CRDC}$ is typically 0.15 to 0.25, but can reach values up to 0.45 to 0.5. The term $\Delta N_b/N_b$ in Eq. 4.10 contributes with values between 0.05 and 0.1, and the $\Delta N_t/N_t$ has a small value of 0.01. Overall, the relative uncertainty $\Delta\sigma_{inc}/\sigma_{inc}$ is typically between 0.20 and 0.25, but can reach up to 0.5, and is therefore dominated by

the relative uncertainty in the S800 acceptance, $\Delta K_{CRDC}/K_{CRDC}$. In the calculation of the different terms in Eq. 4.10 it is assumed [Yon06] that the estimates of numbers of counts in the particle identification plots using SpecTcl carry an uncertainty of 5%. Detailed calculations of uncertainties are included in Appendix B.

4.5 Experimental Details

4.5.1 Properties of Beams and Targets

In both experiments at MSU (E03053 and E05122), the primary beam of ^{48}Ca at 140 MeV/A and 15 pnA (one particle nanoamp $\cong 6x10^9$ particles per second) was fragmented against a primary or transmission ^{9}Be target. The ^{9}Be target had a thickness of 846 mg/cm^2 in E03053, and 376 mg/cm^2 in E05122. The fragmentation of the primary beam generated secondary radioactive ion beams (RIB) that were transported through the A1900 and the S800 beamlines.

In E03053, two types of secondary "cocktail" beams ($^{29}Na/^{30}Mg/^{32}Al$ and $^{32}Mg/^{33}Al/^{35}Si$) were produced at energies of ~90-105 MeV/A ($\beta \sim 0.41$-0.44); their properties are summarized in Tables 4.2 and 4.3. In the E05122 experiment, three types of "nearly pure" secondary beams with an energy range of ~80-90 MeV/A ($\beta \sim 0.39$-0.41), were sequentially produced and utilized: ^{31}Mg, ^{32}Mg, and ^{31}Na; their properties are included in Table 4.4.

Table 4.2 Properties of the secondary beam components of the cocktail beam (^{29}Na/^{30}Mg/^{32}Al) in E03053, including magnetic rigidities of the analysis line and the S800 spectrograph, their energies and velocities, and the final fragments generated by each secondary beam type. The secondary beams were produced by the fragmentation of a ^{48}Ca primary beam at 140 MeV/A and 15 pnA intensity incident on a 846 mg/cm^2 ^{9}Be primary or transmission target located at the entrance of the A1900 fragment separator. The secondary ^{9}Be target thickness is 565 mg/cm^2.

Secondary beams	Bρ (analysis line)	Bρ (S800)	Energy before secondary target	Velocity before target	Energy at mid-target position	Velocity at mid-target position	Products
	(T-m)	(T-m)	(MeV/A)	(v/c)	(MeV/A)	(v/c)	
^{29}Na	3.9142	4	100.9	0.431	93.7	0.418	^{28}Ne
^{30}Mg	3.9142	4	111.6	0.450	104	0.437	^{29,30}Na, ^{26,27,28}Ne
^{32}Al	3.9142	4	114.9	0.456	106.8	0.442	^{29,30}Na, ^{26,27,28}Ne

Table 4.3 Properties of the secondary beam components of the cocktail beam (^{32}Mg/^{33}Al/^{35}Si) in E03053, including magnetic rigidities of the analysis line and the S800 spectrograph, their energies and velocities, and the final fragments generated by each secondary beam type. The secondary beams were produced by the fragmentation of a ^{48}Ca primary beam at 140 MeV/A and 15 pnA intensity incident on a 846 mg/cm^2 ^{9}Be primary or transmission target located at the entrance of the A1900 fragment separator. The secondary ^{9}Be target thickness is 565 mg/cm^2.

Secondary beams	Bρ (analysis line)	Bρ (S800)	Energy before secondary target	Velocity before target	Energy at mid-target position	Velocity at mid-target position	Products
	(T-m)	(T-m)	(MeV/A)	(v/c)	(MeV/A)	(v/c)	
^{32}Mg	3.9232	4	99.1	0.428	91.3	0.413	^{31,32}Na, ^{28,29,30}Ne
^{33}Al	3.9232	4	111.6	0.450	104	0.437	^{32,33}Mg, ^{29,30,31}Na, ^{27,28}Ne
^{35}Si	3.9232	4	114.9	0.456	106.8	0.442	^{32,33}Mg, ^{29,30,31}Na, ^{27,28}Ne

Table 4.4 Properties of the secondary beams used in E05122, including magnetic rigidities of the analysis line and the S800 spectrograph, their energies and velocities, and the final fragments generated by each secondary beam type. The secondary beams were produced by the fragmentation of a ^{48}Ca primary beam at 140 MeV/A and 15 pnA intensity incident on a 376 mg/cm^2 ^{9}Be primary or transmission target located at the entrance of the A1900 fragment separator. The secondary ^{9}Be target thickness is 376 mg/cm^2.

Secondary beams	Bρ (analysis line)	Bρ (S800)	Energy before secondary target	Velocity before target	Energy at mid-target position	Velocity at mid-target position	Products
	(T-m)	(T-m)	(MeV/A)	(v/c)	(MeV/A)	(v/c)	
^{31}Mg	3.668	3.6185	92.7	0.416	87.1	0.405	^{29,30,31}Na, ^{26,27,28}Ne
^{32}Mg	3.6673	3.4957	87.2	0.405	81.5	0.393	^{30,31}Na, ^{27,28}Ne
^{32}Mg	3.6673	3.7201	87.2	0.405	81.5	0.393	^{31,32}Na, ^{28,29,30}Ne
^{32}Mg	3.6673	3.8	87.2	0.405	81.5	0.393	^{31,32}Na, ^{28,29,30}Ne
^{31}Na	4.033	3.6371	94	0.418	89.3	0.409	^{30}Na

4.5.2 Experimental Determination of the Target Position

In both MSU experiments, a method was developed to accurately verify the position of the secondary ^{9}Be target (z_o) with respect to the center of SeGA, where a positive (negative) value of z_o corresponds to the target being located downstream (upstream) from the center of SeGA. The procedure to determine the correct target z_o value is to use the γ-ray spectra of a fragment with accurately known peak energies. We used ^{26}Ne which has a γ-ray transition at 2018.2(1) keV, measured in the β-decay of ^{26}F [Ree99].

The data acquisition software SpecTcl [Spe07] was used to generate and analyze the 37°- and 90°-ring γ-ray spectra for varying values of the parameters z (position of the

target) and β (velocity of the fragment), chosen to give the correct, known, γ-ray energy at ~2018 keV.

Table 4.5 shows pairs of (β,z) values for which the ^{26}Ne peak is located at ~2018 keV, both for the 37°- and the 90°-rings, in experiments E03053 and E05122. The experimental points were fitted to straight lines separately for the 37°- and the 90°-rings, and the correct position of the target z_o is given by the intersection of these two lines (Figs. 4.15 and 4.16), at $z_{o,2004}$ = -0.49(14) cm in E03053, and $z_{o,2006}$ = -1.66(20) cm in E05122.

Table 4.5 Pairs of (β,z) values used to determine the correct position of the target (z_o) in E03053 and E05122 experiments.

E03053 experiment			E05122 experiment		
	37°-ring	90°-ring		37°-ring	90°-ring
β	z (cm)	z (cm)	β	z (cm)	z (cm)
0.42	-2	0.55	0.4	-2.3	-1.4
0.44	-0.8	-0.2	0.42	-1	-1.9
0.45	-0.4	-0.6	0.44	0.35	-2.55

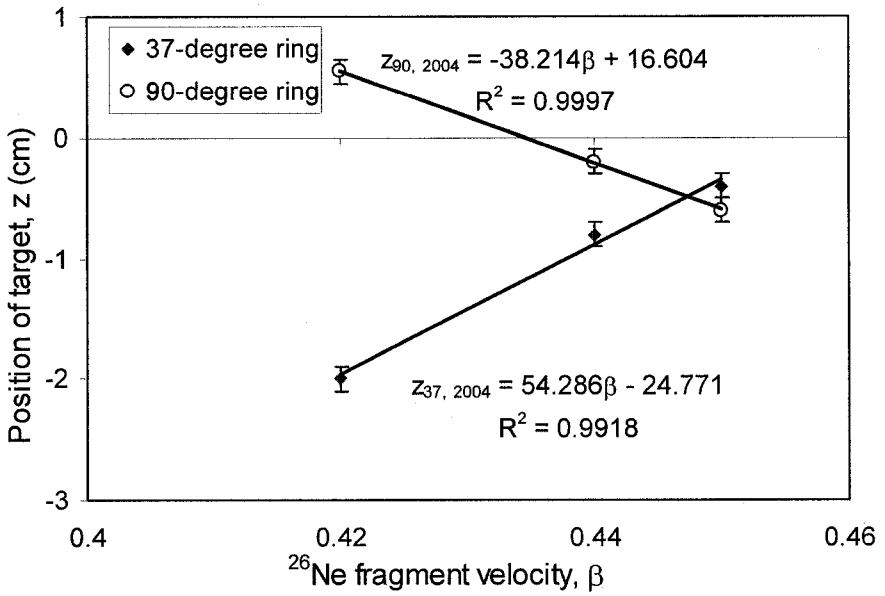

Figure 4.15 Determination of the target position, z_o, in E03053. The data points are pairs of (β,z) values corresponding to the ~2018-keV γ-ray transition in ^{26}Ne, in the 37°- and 90°-ring spectra. The intersection of the two lines gives the target position, $z_{o,2004}$ = -0.49(14) cm.

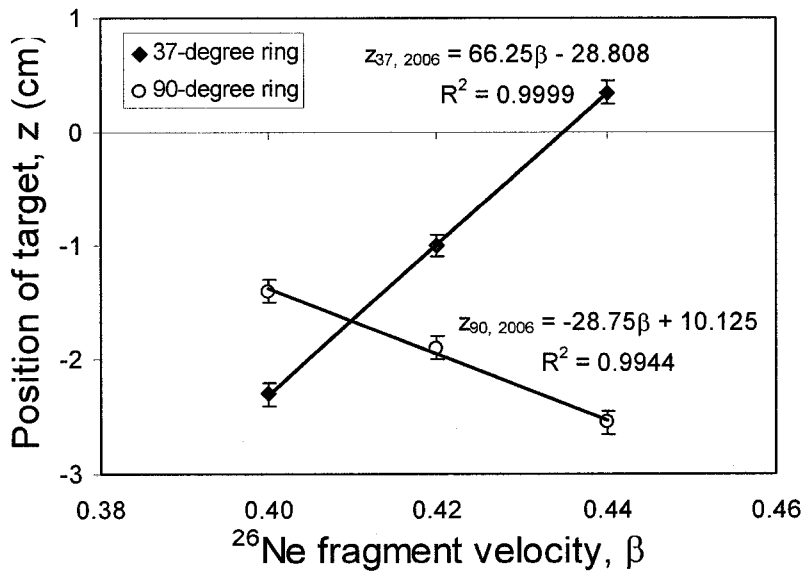

Figure 4.16 Determination of the target position, z_o, in E05122. The data points are pairs of (β,z) values corresponding to the ~2018-keV γ-ray transition in ^{26}Ne, in the 37°- and 90°-ring spectra. The intersection of the two lines gives the target position, $z_{o,2006}$ = -1.66(20) cm.

4.5.3 Experimental Determination of the Velocity (β) of Fragments

The data acquisition software SpecTcl [Spe07] was used to generate and analyze Doppler-corrected γ-ray spectra of different fragments as a function of velocity β for the z_o position determined above (Section 4.5.2). The experimentally determined β is that value for which γ-ray peaks in the 37°-ring spectrum are located at the same energy values as those in the 90°-ring spectrum. An example of the experimental determination of β for ^{28}Ne produced by one-proton knockout of ^{29}Na in E03053 is shown in Fig. 4.17.

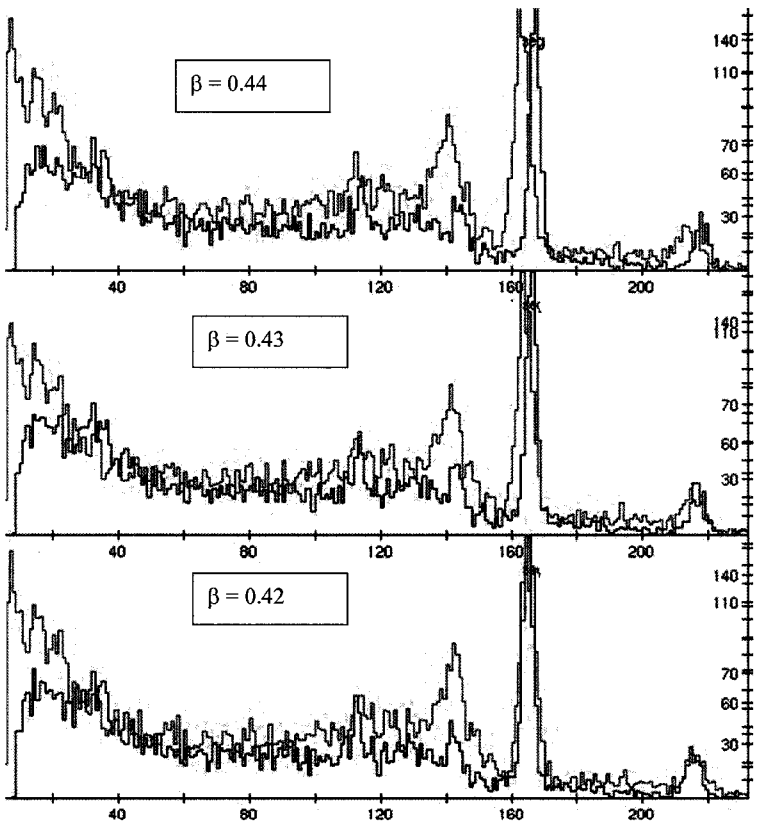

Figure 4.17 Determination of the fragment velocity. This figure shows the 37°-(red) and 90°-ring (blue) γ-ray spectra of the ^{28}Ne fragment produced by one-proton knockout of ^{29}Na secondary beam in E03053. The experimental spectra show that the β value of the emitted ^{28}Ne fragment is 0.42, for which the 37°- and 90°-ring spectra overlap with each other.

4.5.4 Experimental Determination of the Intensity and Energies of γ-Ray Transitions

The intensity of a γ-ray peak is the ratio of the background-subtracted area divided by the Lorentz-boosted efficiency of the SeGA array. Since the Lorentz-boosted efficiencies are different for the 37°- and 90°-rings, it is necessary to obtain two separate measurements of γ-ray peak intensities, I_{37} and I_{90}, using each of the separate efficiency curves:

$$I_{37} = \frac{N_{37}}{\varepsilon_{37}} = \frac{N_{37}}{f_{37}\,\varepsilon_{abs\_37}}$$
$$I_{90} = \frac{N_{90}}{\varepsilon_{90}} = \frac{N_{90}}{f_{90}\varepsilon_{abs\_90}} \qquad (4.11)$$

where N_{37} and N_{90} are the numbers of background-subtracted areas in the 37°- and 90°-ring spectra, f_{37} and f_{90} the Lorentz-boost factors, and ε_{37} and ε_{90}, the Lorentz-boosted efficiencies. The intensity of a γ-ray peak is calculated as the average of the two independent measurements: I_{37} and I_{90}, assuming that γ-ray emission is approximately isotropic in the rest frame.

In using the Lorentz-boosted efficiency curves, it is necessary to use the efficiency for the Doppler-shifted γ-ray energy, that is, for the $E_\gamma(\theta)$ values in Eq. 4.3. So, for example, in ^{30}Ne the value of $E_\gamma^{\,o}$ (the Doppler-reconstructed energy provided by the data acquisition software) for its most intense γ-ray peak was 791.6 keV. Its Doppler-shifted energies (assuming $\beta = 0.40$) are $E_\gamma^{lab}(37^o) = 1113.57$ keV, and $E_\gamma^{lab}(90^o) = 757.84$ keV. These are the energy values used to obtain the corresponding Lorentz-boosted efficiencies ε_{37} and ε_{90}. The energy and γ-ray intensity measurements, as well as their errors, are included in Appendix C.

The γ-ray energies are experimentally determined by fitting the peak shapes to Gaussians using the gf3 program [Rad07]; this program provides the statistical errors of the peak energies. The systematic errors in the peak energies originate from two contributions: the uncertainty in the target position (Δz_o), and the uncertainty in the velocity β of the γ-emitting fragments ($\Delta\beta$), which is used in the Doppler reconstruction of the γ-ray spectra.

Chapter 5

Results

Neutron-rich fragments in the region of N ~ 20 and A ~ 30 were produced by few-nucleon knockout of secondary "cocktail" beams (^{29}Na/^{30}Mg/^{32}Al and ^{32}Mg/^{33}Al/^{35}Si) in experiment E03053, and from three separate secondary beams (^{31}Mg, ^{32}Mg and ^{31}Na) in E05122.

The experimental results are divided into four sections corresponding to four different knockout reaction mechanisms that were used to produce and study neutron-rich $^{28-30}$Ne isotopes. For each reaction we present γ-ray spectroscopy data on the energies and intensities of γ-ray transitions in the final product and the proposed level scheme of excited states populated in the given product. Also for each reaction we present data on its inclusive cross section, as well as on partial cross sections to the ground state and to excited states, derived from γ-ray data. In the Discussion (Chapter 6), we will compare data with shell-model calculations using USD-A and SDPF-M interactions and the cross section measurements with predictions from knockout reaction theory.

Tables 5.1 through 5.3 list the Ne and Na fragments obtained from different secondary beams and include measured fragment velocities (β) and measured production cross sections, both experimentally determined using the methods described in Chapter 4. Details of the analysis performed to obtain these cross sections are given in Appendix B and include cross sections to other fragments such as Mg, F, and N.

Table 5.1 **Neutron-rich Ne and Na produced in experiment E03053 (^{29}Na/^{30}Mg/^{32}Al secondary beams).** The table includes secondary beam energies at the mid-target position (center of SeGA).

Secondary beam	Fragment	Fragment β	σ_{inc} (mb)
^{29}Na 94 MeV/A	^{28}Ne	0.42	14(7)
^{30}Mg 104 MeV/A	^{26}Ne	0.44	0.28(6)
	^{27}Ne	0.44	0.7(2)
	^{28}Ne	0.43	0.8(2)
	^{29}Na	0.43	2.6(6)
	^{30}Na	0.43	0.8(2)
^{32}Al 107 MeV/A	^{26}Ne	0.44	0.30(7)
	^{27}Ne	0.44	0.27(6)
	^{28}Ne	0.43	0.31(7)
	^{29}Na	0.43	1.3(3)
	^{30}Na	0.43	1.4(3)

Table 5.2 **Neutron-rich Ne and Na produced in experiment E03053 (^{32}Mg/^{33}Al/^{35}Si secondary beams).** The table includes secondary beam energies at the mid-target position (center of SeGA).

Secondary beam	Fragment	Fragment β	σ_{inc} (mb)
^{32}Mg 91 MeV/A	^{28}Ne	0.43	0.5(3)
	^{29}Ne	0.40	0.26(6)
	^{30}Ne	0.40	0.25(5)
	^{31}Na	0.43	1.2(6)
^{33}Al 104 MeV/A	^{27}Ne	0.43	0.08(3)
	^{28}Ne	0.43	0.14(3)
	^{29}Na	0.44	0.12(6)
	^{30}Na	0.44	0.34(8)
	^{31}Na	0.43	0.46(9)
^{35}Si 107 MeV/A	^{27}Ne	0.43	0.05(2)
	^{28}Ne	0.43	0.05(1)
	^{29}Na	0.44	0.11(6)
	^{30}Na	0.44	0.14(3)
	^{31}Na	0.43	0.14(3)

Table 5.3 Neutron-rich Ne and Na fragments produced in experiment E05122. The table includes secondary beam energies at the mid-target position (center of SeGA). The three different ^{32}Mg secondary beam experiments correspond to S800 settings of: (a) Bρ = 3.4957 T-m, (b) Bρ = 3.7201 T-m, and (c) Bρ = 3.8 T-m.

Secondary beam	Fragment	Fragment β	σ_{inc} (mb)
^{31}Mg 87 MeV/A	^{26}Ne	0.41	2.6(9)
	^{27}Ne	0.40	1.4(2)
	^{28}Ne	0.395	0.6(1)
	^{30}Na	0.40	14(2)
	^{31}Na	0.40	0.9(2)
^{32}Mg$^{(a)}$ 82 MeV/A	^{27}Ne	0.39	0.9(2)
	^{28}Ne	0.38	1.0(2)
	^{30}Na	0.385	6(1)
	^{31}Na	0.39	4.4(8)
^{32}Mg$^{(b)}$ 82 MeV/A	^{28}Ne	0.40	2.1(8)
	^{29}Ne	0.39	0.27(5)
	^{30}Ne	0.39	0.21(6)
	^{31}Na	0.39	14(5)
	^{32}Na	0.39	0.48(9)
^{32}Mg$^{(c)}$ 82 MeV/A	^{28}Ne	0.40	0.2(1)
	^{29}Ne	0.39	0.21(4)
	^{30}Ne	0.39	0.21(4)
	^{31}Na	0.40	0.4(2)
	^{32}Na	0.39	0.2(1)

5.1 One-Proton Knockout: ^{9}Be(^{29}Na,^{28}Ne)

Figure 5.1 shows the Doppler-corrected (β = 0.42) prompt γ-ray spectrum of ^{28}Ne produced by one-proton knockout from ^{29}Na with an inclusive cross section: σ_{inc} (^{9}Be(^{29}Na,^{28}Ne)) = 14(7) mb, for an average ^{29}Na energy of 94 MeV/A. The γ-ray statistics were sufficient to obtain γ-γ coincidence data (Figs. 5.2 and 5.3), which allowed the identification of three γ-ray transitions at 1306(4), 1707(7), and 891(5) keV, forming a cascade with relative intensities of 100, 23(3), and 10(2)%, respectively (Fig. 5.4). The

uncertainties in the energies include statistical and systematic uncertainties, as described in Chapter 4. The resulting experimental level scheme of ^{28}Ne shown in Fig. 5.4(a) is compared with the most recently published experimental scheme [Bel05] in Fig. 5.4(b). The tentative spin assignments were made based on γ-ray intensity considerations and comparison with shell-model calculations, as will be discussed in Chapter 6.

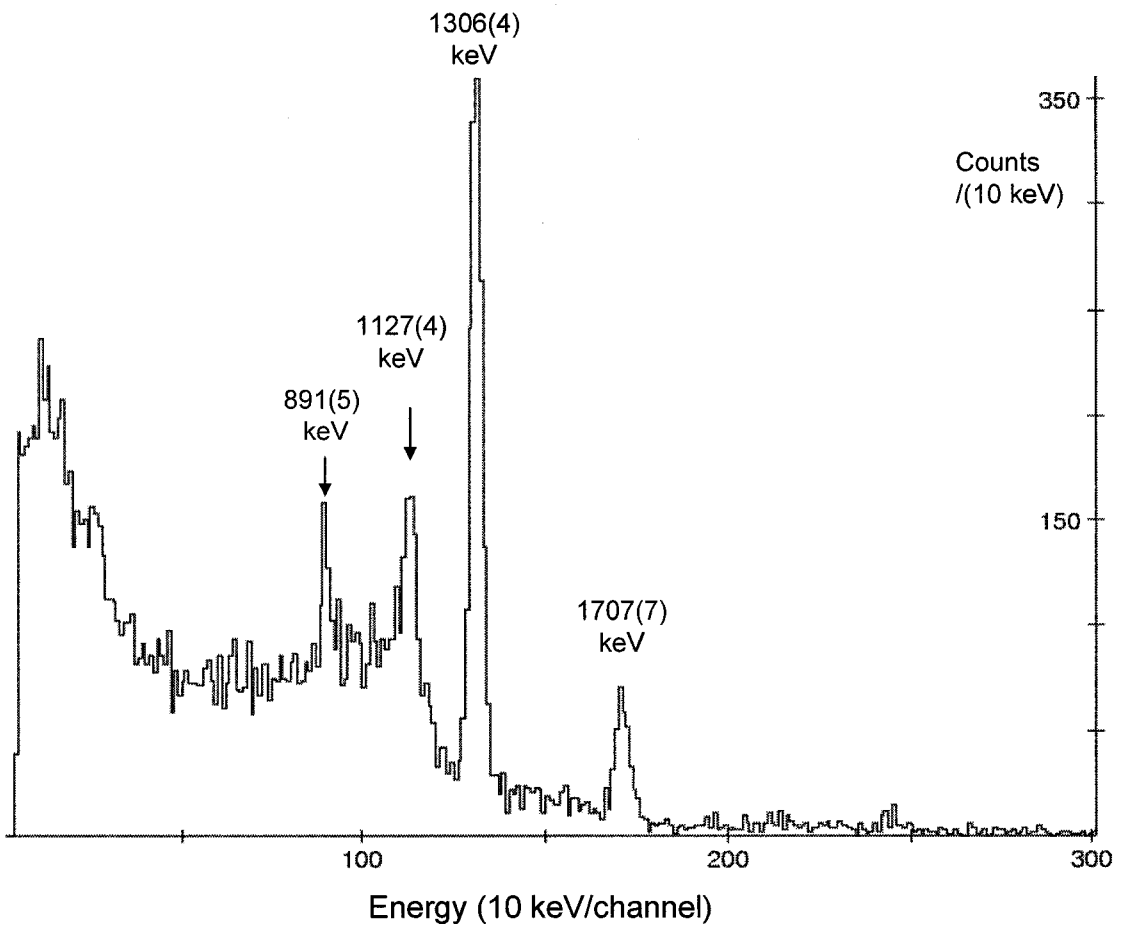

Figure 5.1 Doppler-corrected γ-ray spectrum of ^{28}Ne produced by one-proton knockout of ^{29}Na. The β of ^{28}Ne is 0.42.

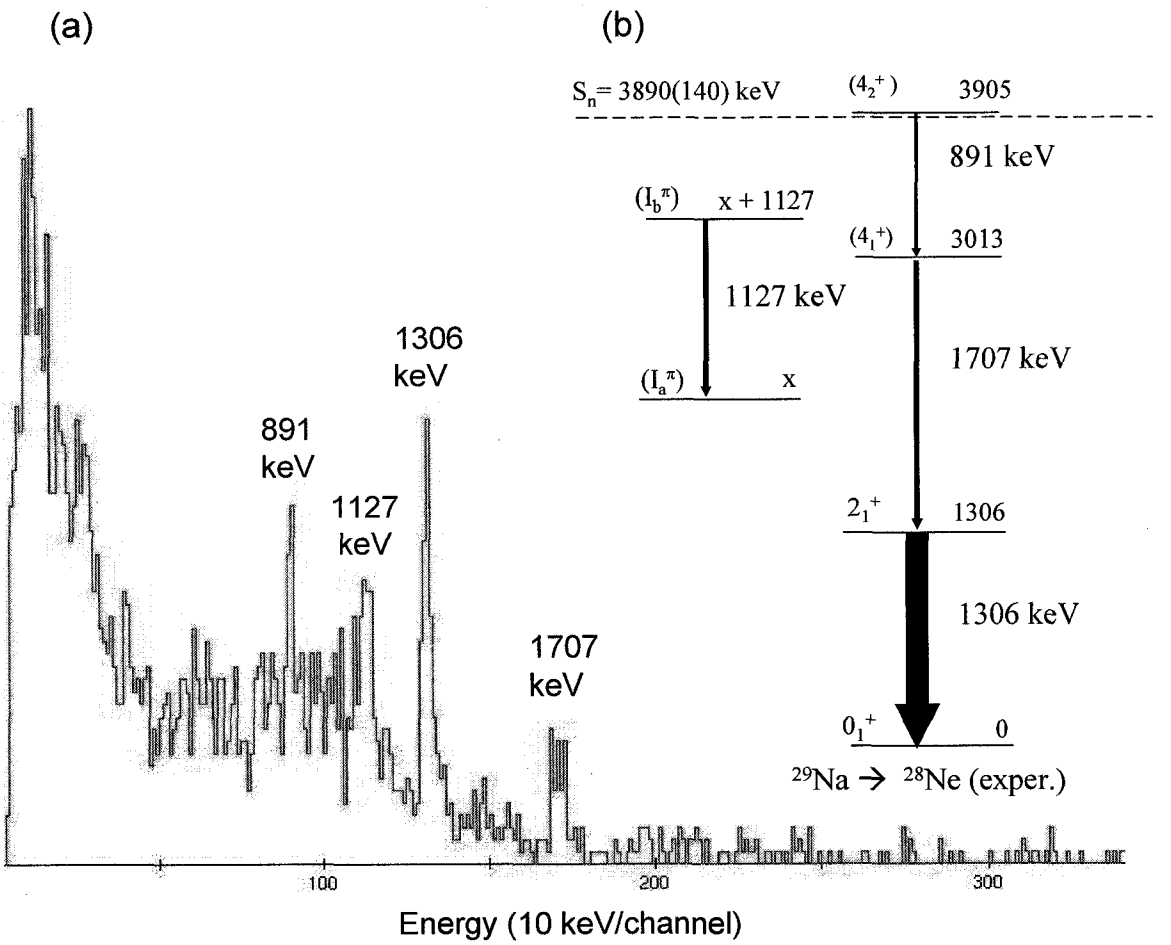

Figure 5.2 (a) Total projection of Doppler-corrected (β = 0.42) γ-γ coincidences, and (b) proposed level scheme of excited states in ^{28}Ne produced by one-proton knockout of ^{29}Na. In Fig. 5.2(b), the thickness of the arrows is roughly proportional to the corresponding γ-ray transition intensity.

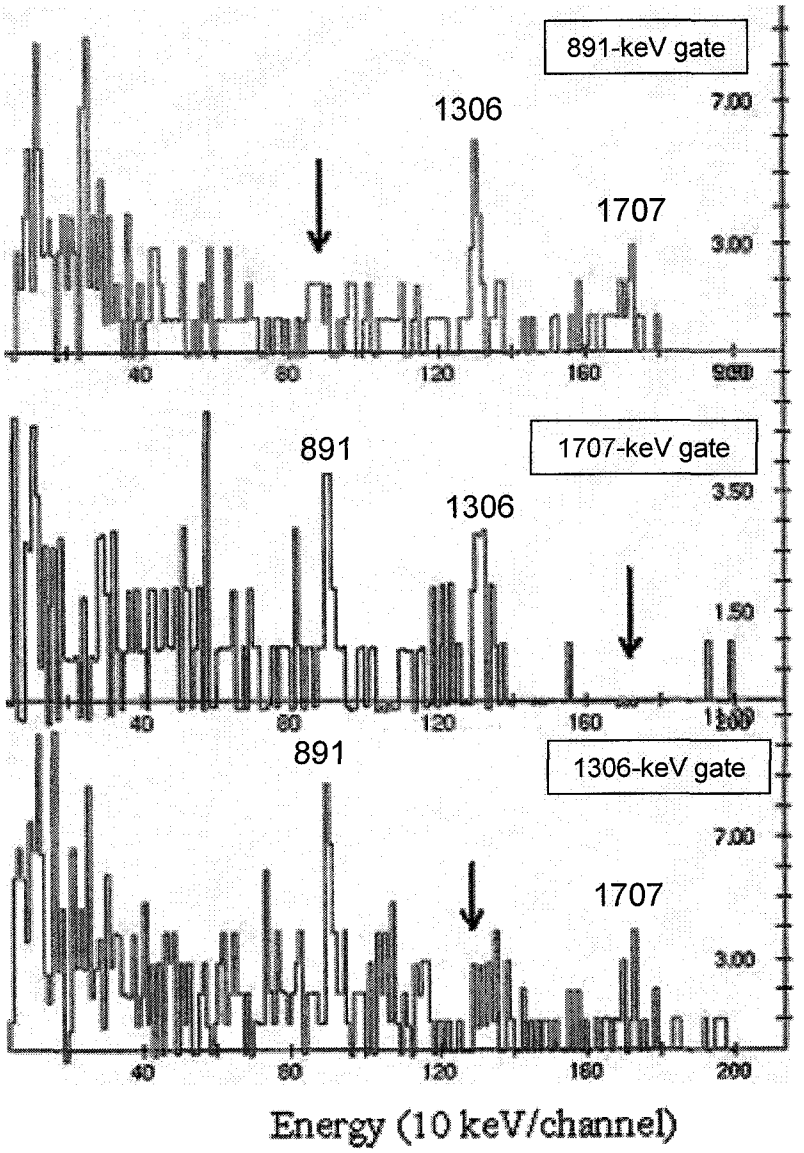

Figure 5.3 Gated Doppler-corrected spectra of ^{28}Ne produced by one-proton knockout of ^{29}Na. The arrows denote the gate energies.

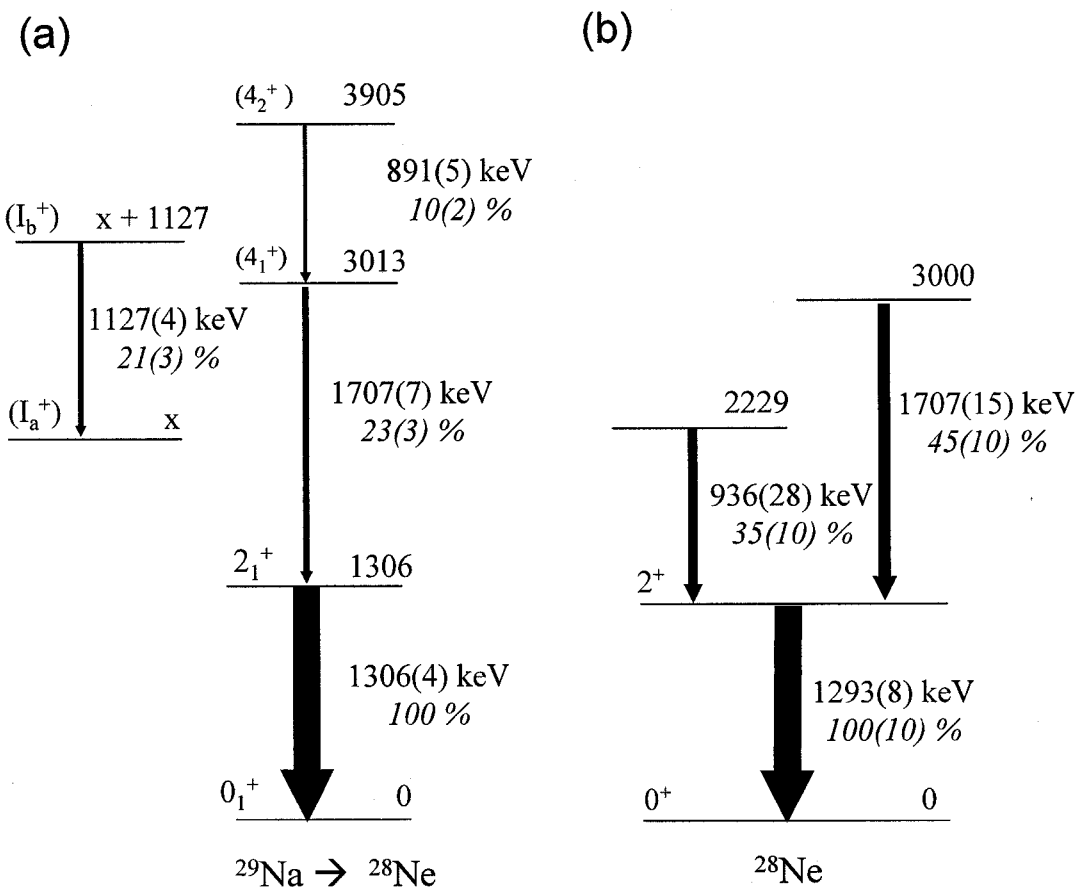

Figure 5.4 Comparison of (a) experimental level scheme of ^{28}Ne produced by one-proton knockout of ^{29}Na, and (b) recent literature data [Bel05] obtained by one- and two-step fragmentation of a ^{36}S primary beam and ^{29,30}Mg secondary beams. In our experimental data (a), the 891-keV γ ray was found to be in coincidence with both the 1707-keV and 1306-keV transitions. The thickness of the arrows is roughly proportional to the corresponding γ-ray transition intensity.

The 1306(4)-keV transition (feeding the 0_1^+ ground state) is reported in the Evaluated Nuclear Structure Data File [ENS07] with a half-life of 2.6 ps and no confirmed spin/parity assignment. The ^{28}Ne 0_1^+ ground state is listed with a half-life of 19(3) ms. The neutron separation energy of ^{28}Ne is given as 3890(140) keV [ENS07].

A 1320(20)-keV transition was first experimentally measured in Coulomb excitation [Pri99], and soon after in fragmentation [Bel00, Aza02a, Aza02b, Gui02]; based on

intensity considerations in these experiments the 1320(20)-keV level was assigned a spin and parity value of 2_1^+. The latter authors also identified an additional γ-ray at 1750(50) keV which was assigned to the $4_1^+ \rightarrow 2_1^+$ transition based on intensity considerations; statistics were not sufficient to allow the analysis of γ-γ coincidence data.

A more recent experiment [Bel05] involving one- and two-step fragmentation with a 77.5 MeV/A ^{36}S primary beam and ~60 MeV/A neutron-rich Na and Mg secondary beams reported three γ-ray transitions in ^{28}Ne at 1293(8), 1707(15), and 936(28) keV; these energy values are in reasonable agreement with the experimental data in our work. In addition, γ-γ coincidences [Bel05] were used to show that the 1707-keV and 936-keV transitions are in coincidence with the 1293-keV (corresponding to the $2_1^+ \rightarrow 0^+_{1(g.s.)}$). The limited statistics of this experiment [Bel05] only allowed the authors to postulate the 936-keV transition to feed the 2_1^+ level in parallel with the 1707-keV γ ray. Our γ-γ coincidence data, however, allow us to unequivocally determine that the 891-keV γ-ray (which is assumed to correspond to the 936-keV γ ray in [Bel05]) is in coincidence with the 1707-keV and located above it, forming a single cascade (Fig. 5.4(a)). This is an important difference, as Belleguic *et al.* [Bel05] postulated the 936-keV transition to connect the 0_2^+ to the 2_1^+ state. Our data rules out the scenario which gives an excited 0_2^+ state at ~2.2 MeV as predicted by the sdpf-shell calculation (Chapter 6). The consequences of our result will be discussed in Chapter 6.

The two lowest transitions in this cascade (Fig. 5.4(a)) have also been recently observed in proton inelastic scattering in inverse kinematics using a liquid hydrogen target at RIKEN [Dom06a, Dom06b], and the reported energies at 1319(22) and 1711(30) keV are in agreement with previous and current data.

In our experiment, the ^{28}Ne spectrum contains one additional (and new) strong γ-ray transition at 1127(4) keV with a relative intensity of 21(3)%, which is not in coincidence with any other transition. It is very unlikely that the 1127-keV γ ray directly feeds the ground state and it is placed "floating" to the left of the main cascade in Figs. 5.2 and 5.4. It is possible that it feeds an isomeric state, as will be discussed in Chapter 6.

Table 5.4 summarizes the level energies, γ-ray transition energies and intensities, fractional populations of states, and cross section data for the ^{9}Be(^{29}Na,^{28}Ne) one-proton knockout reaction.

Table 5.4 Level energies, γ-ray transition energies and intensities, fractional populations of states, and cross section data for ^{9}Be(^{29}Na,^{28}Ne).

Level I^{π}	Level energy, E_i (keV)	Energy of γ-ray decay, $E\gamma$ (keV)	Relative γ-ray intensity, I_γ (%)	Fractional population of level i, b_i	Partial cross section of level i, σ_i (mb)
0_1^+	0			0.15(3)*	2(1)*
2_1^+	1306(4)	1306(4)	100	0.55(7)	8(4)
(4_1^+)	3013(8)	1707(7)	23(3)	0.09(2)	1.2(7)
(4_2^+)	3905(9)	891(5)	10(2)	0.07(2)	1.0(5)
I_b^{π}	x + 1127(4)	1127(4)	21(3)	0.15(2)	2(1)
Total				1	14(7)
σ_{inc} (^{9}Be(^{29}Na,^{28}Ne)) = 14(7) mb					

*These numbers include any direct feeding of the I_a^{π} state.

5.2 Two-Proton Knockout: ^{9}Be(^{30}Mg,^{28}Ne)

Figure 5.5(a) shows the Doppler-corrected (β = 0.43) prompt γ-ray spectrum of ^{28}Ne produced by two-proton knockout from ^{30}Mg (104 MeV/A), with an inclusive cross section: σ_{inc} (^{9}Be(^{30}Mg,^{28}Ne)) = 0.8(2) mb. A value σ_{inc} (^{9}Be(^{30}Mg,^{28}Ne)) = 0.49(5) mb was reported in [Baz03b] for a ^{30}Mg beam energy of 88.5 MeV/A. The resulting experimental level scheme is given in Fig. 5.5(b).

Table 5.5 summarizes the level energies, γ-ray transition energies and intensities, fractional populations of excited states, and cross section data for the ^{9}Be(^{30}Mg,^{28}Ne) two-proton knockout reaction. The level scheme of ^{28}Ne produced from two-proton knockout is identical to the one formed in the one-proton knockout mechanism, already described in Section 5.1. While the γ-ray energies are consistent (within experimental errors) with those obtained in the one-proton knockout reaction, the transition intensities do show some differences, reflecting the different production mechanisms and the initial beam. Overall, the two-proton knockout and the one-proton knockout reactions lead to similar γ-ray spectra for ^{28}Ne.

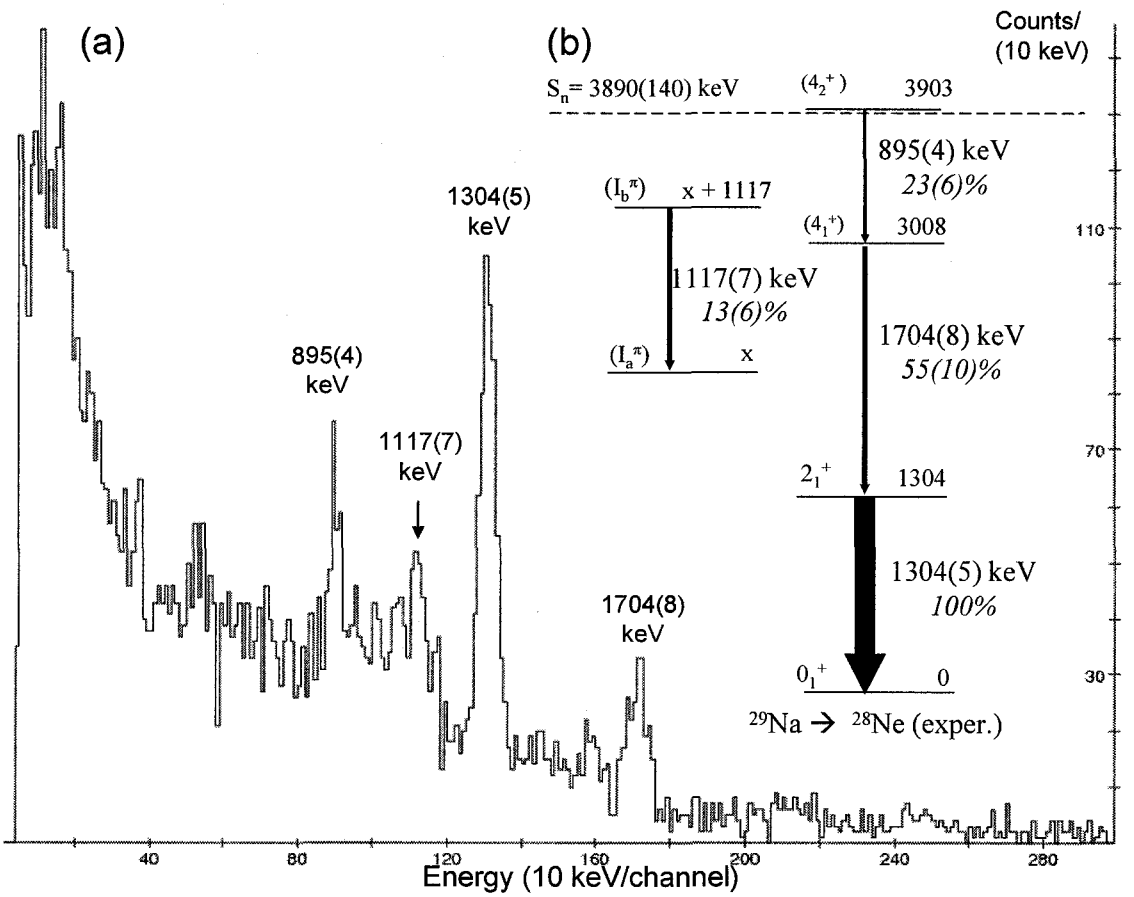

Figure 5.5 (a) Doppler-corrected γ-ray spectrum of ^{28}Ne produced by ^{30}Mg (two-proton knockout) and ^{32}Al, and (b) proposed level scheme of excited states. The β of ^{28}Ne is 0.43. In Fig. 5.5(b), the thickness of the arrows is roughly proportional to the corresponding γ-ray transition intensity.

Table 5.5 Level energies, γ-ray transition energies and intensities, fractional populations of states, and cross section data for ^{9}Be(^{30}Mg,^{28}Ne).

Level I^{π}	Level energy, E_i (keV)	Energy of γ-ray decay, Eγ (keV)	Relative γ-ray intensity, I_γ (%)	Fractional population of level i, b_i	Partial cross section of level i, σ_i (mb)
0_1^+	0			0.5(3)*	0.4(2)*
2_1^+	1304(5)	1304(5)	100	0.19(4)	0.16(4)
(4_1^+)	3008(9)	1704(8)	55(10)	0.14(4)	0.11(4)
(4_2^+)	3903(10)	895(4)	23(6)	0.09(3)	0.08(3)
I_b^{π}	x + 1117(7)	1117(7)	13(6)	0.05(3)	0.05(2)
Total				1	0.8(2)
σ_{inc} (^{9}Be(^{30}Mg,^{28}Ne)) = 0.8(2) mb					

*These numbers include any direct feeding of the I_a^{π} state.

5.3 Two-Proton Knockout: ^{9}Be(^{32}Mg,^{30}Ne)

^{30}Ne was produced by two-proton knockout from ^{32}Mg (~80-90 MeV/A) in two experiments. Experiment E03053 provided one measurement at 0.25(5) mb, while in E05122 we measured two values at 0.21(6) and 0.21(4) mb. The average of the three measurements gives an inclusive cross section: σ_{inc} (^{9}Be(^{32}Mg,^{30}Ne)) = 0.22(3) mb.

The Evaluated Nuclear Structure Data File [ENS07] provides the half-life of the ^{30}Ne 0_1^+ ground state as 7(2) ms, and the neutron separation energy S_n to be 3030(630) keV. ENSDF lists only one excited state at 791(26) keV in ^{30}Ne. This γ-ray transition was observed in a proton inelastic scattering experiment [Yan03, Yan04], which was performed in inverse kinematics with a liquid hydrogen target and a beam of radioactive ^{30}Ne at 48 MeV/A. The observed γ ray at 791(26) keV was assigned to the $2_1^+ \rightarrow 0_1^+{}_{(g.s.)}$

transition, since the 2_1^+ state is expected to be strongly populated in even-even nuclei in this region, and its population is also favored in inelastic scattering processes.

In our experiments, the γ-ray spectrum of ^{30}Ne produced by two-proton knockout from ^{32}Mg is shown in Fig. 5.6(a). This is the sum of spectra obtained in the E03053 and E05122 experiments. The Doppler-corrected γ-ray spectra of ^{30}Ne produced by ^{32}Mg corresponded to values of $\beta = 0.40$ (E03053) and $\beta = 0.39$ (E05122). The strongest γ-ray transition (Fig. 5.6(a)) was observed at an energy of 792(4) keV. This energy is consistent with the previously measured 791(26)-keV γ-ray [Yan03, Yan04], which was associated to the $2_1^+ \rightarrow 0_1^+$ transition. Our measurement provides an important confirmation of the location of the 2_1^+ state. The high statistics achieved by the combination of data from both experiments allowed us to identify a second peak at 1443(11) keV, which we postulate to represent the 4_1^+ to 2_1^+ transition based on its relative intensity of 39(12)% and on the comparison between experimental and calculated partial cross sections to the ground state and excited states, as discussed in Chapter 6. The proposed level scheme is presented in Fig. 5.6(b).

Table 5.6 contains the level energies, γ-ray transition energies and intensities, fractional populations of states, and cross section data for the ^{9}Be(^{32}Mg,^{30}Ne) two-proton knockout reaction. The detailed cross section calculations are included in Appendix B.

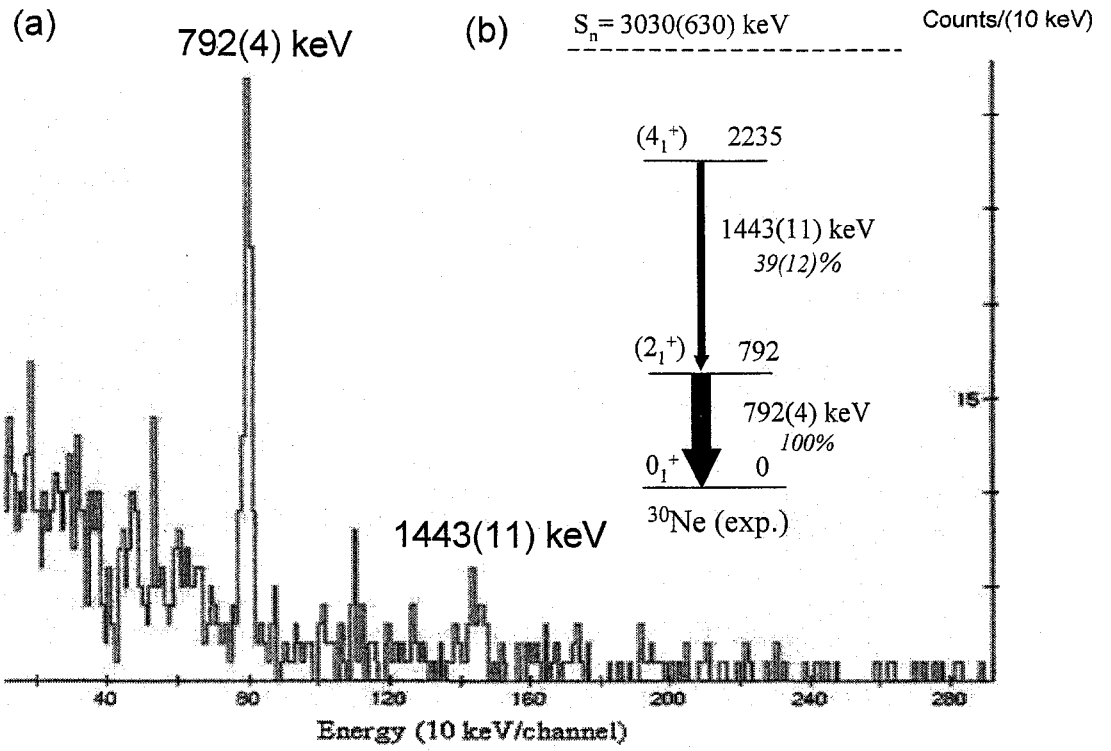

Figure 5.6 **(a) Doppler-corrected γ-ray spectrum of ^{30}Ne produced by two-proton knockout of ^{32}Mg, and (b) proposed level scheme of excited states.** The spectrum in Fig. 5.6(a) is the result of one measurement in E03053 (β = 0.40) and two measurements in E05122 (β = 0.39). In Fig. 5.6(b), the thickness of the arrows is roughly proportional to the corresponding γ-ray transition intensity.

Table 5.6 **Level energies, γ-ray transition energies and intensities, and partial and inclusive cross section data of ^{9}Be(^{32}Mg,^{30}Ne).**

Level I^π	Level energy, E_i (keV)	Energy of γ-ray decay, Eγ (keV)	Relative γ-ray intensity, I_γ (%)	Fractional population of level i, b_i	Partial cross section of level i, σ_i (mb)
0_1^+	0			0.58(10)	0.13(5)
(2_1^+)	792(4)	792(4)	100	0.26(8)	0.06(3)
(4_1^+)	2235(12)	1443(11)	39(12)	0.16(4)	0.04(2)
Total				1	0.22(3)

σ_{inc} (^{9}Be(^{32}Mg,^{30}Ne)) = 0.22(3) mb

5.4 Few-Nucleon Knockout: ^{9}Be(^{32}Mg,^{29}Ne)

^{29}Ne was produced by two-proton plus one-neutron (2pn) knockout from a ^{32}Mg secondary beam (~80-90 MeV/A). In addition to direct 2pn knockout, the reaction to populate ^{29}Ne may include a component of two-proton knockout followed by neutron evaporation. We obtained three separate measurements, one from E03053 with a cross section of 0.26(6) mb, and two from E05122, with cross sections of 0.27(5) and 0.21(4) mb. The average of the three measurements gives an inclusive cross section: $\sigma_{inc}(^{9}Be(^{32}Mg,^{29}Ne))$ = 0.25(3) mb. The detailed cross section calculations appear in Appendix B. The sum of the three γ-ray spectra is displayed in Fig. 5.7(a); the proposed level scheme in Fig. 5.7(b). The errors in the γ-ray energies result from a combination of statistical and systematic, added in quadrature, as explained in Chapter 4.

The ENSDF database [ENS07] provides only a tentative spin/parity assignment for the ground state of ^{29}Ne ($3/2^{+}$) and a half-life of 15.6(5) ms; no γ-ray transitions are reported. The neutron separation energy in ^{29}Ne is given as 1330(320) keV.

The strongest γ-ray transition observed in the spectrum of Fig. 5.7(a) has an energy of 622(4) keV and is a more accurate determination of a recently published transition at 680(80) keV, which was measured with an array of NaI(Tl) scintillator detectors in a two-step fragmentation experiment [Bel05]. By comparison with shell-model calculations, we assign this γ ray to either the $7/2^{+} \rightarrow 3/2^{+}_{(g.s.)}$ or the $1/2^{+} \rightarrow 3/2^{+}_{(g.s.)}$ transitions, as will be discussed in Chapter 6. A more thorough comparison with shell-model calculations is included in Chapter 6, where the experimental level scheme will be compared with shell-model calculations using USD and SDPF-M interactions.

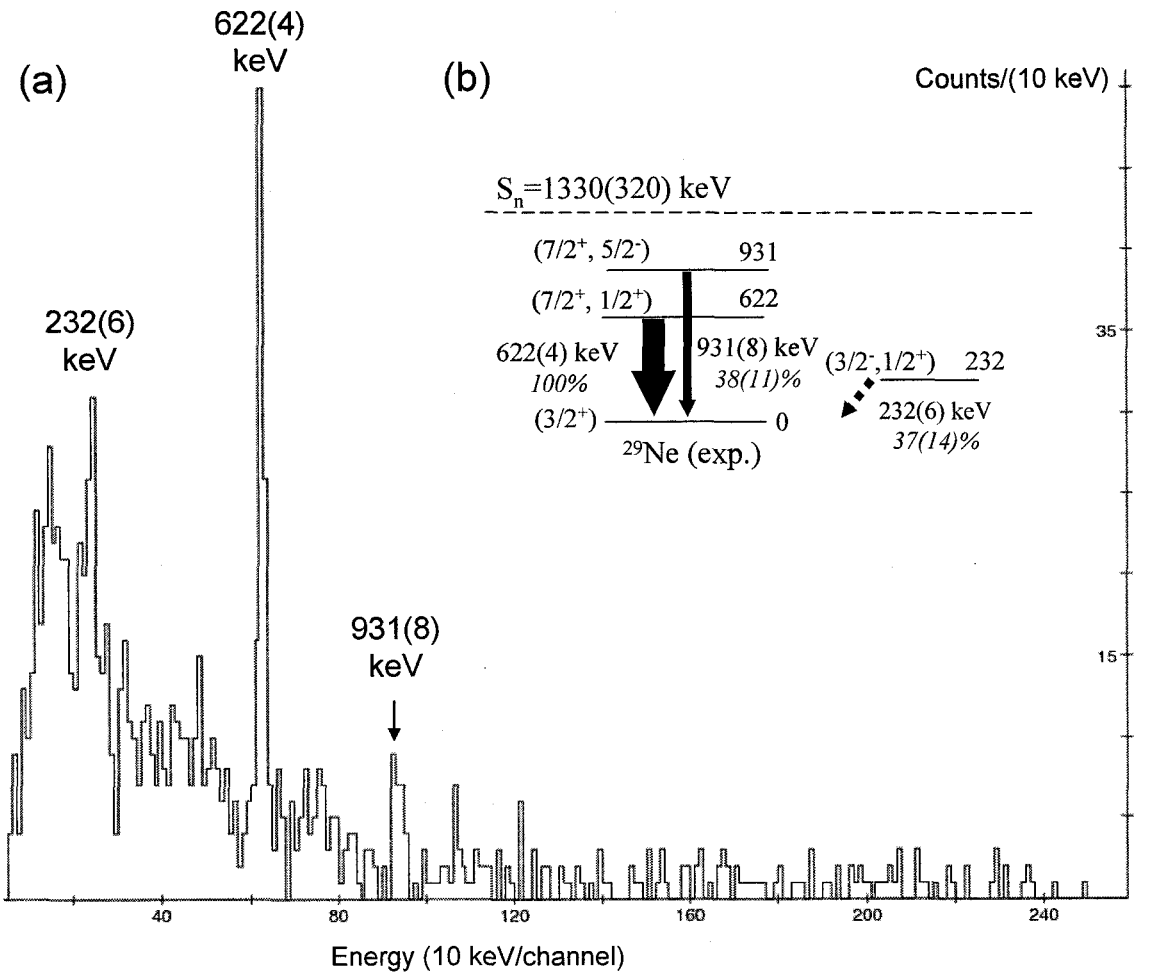

Figure 5.7 (a) Doppler-corrected γ-ray spectrum of ^{29}Ne produced by two-proton plus one-neutron knockout of ^{32}Mg, and (b) proposed level scheme of excited states. The spectrum in Fig. 5.7(a) is the result of one measurement in E03053 (β=0.40) and two measurements in E05122 (β=0.39). In Fig. 5.7(b), the thickness of the arrows is roughly proportional to the corresponding γ-ray transition intensity.

The next transition in order of decreasing relative intensity is that at 931(8) keV, with a relative intensity of 38(11)%, which is postulated to connect the $(7/2^+,5/2^-) \rightarrow 3/2^+_{(g.s.)}$ levels. Given the low neutron separation energy of 1330(320) keV it is highly unlikely that the 931(8)-keV transition is placed above the 622(4)-keV, so they are placed in parallel in the level scheme (Fig. 5.7(b)), both feeding the ground state.

A third transition is observed at 232(6) keV with a relative intensity of 37(14)%, and it is tentatively placed connecting the $(3/2^-, 1/2^+) \rightarrow 3/2^+_{(g.s.)}$ levels.

Earlier publications [Yan03, Yan04] on inelastic scattering of ^{30}Ne suggest two candidate γ rays in ^{29}Ne (obtained by one-neutron removal from ^{30}Ne), at energies of 450 and 580 keV; however, we do not observe any of these two transitions in our experiment. Belleguic *et al.* [Bel05] also do not observe these two candidate transitions in ^{29}Ne in their experimental data.

Table 5.7 summarizes the level energies, γ-ray transition energies and intensities, as well as the inclusive cross section for the ^{9}Be(^{32}Mg,^{29}Ne) knockout reaction.

Table 5.7 Level energies, γ-ray transition energies and intensities, and inclusive cross section of ^{9}Be(^{32}Mg,^{29}Ne).

Level I^π	Level energy, E_i (keV)	Energy of γ-ray decay, $E\gamma$ (keV)	Relative γ-ray intensity, I_γ (%)
$(3/2^+)$	0		
$(7/2^+, 1/2^+)$	622(4)	622(4)	100
$(7/2^+, 5/2^-)$	931(8)	931(8)	38(11)
$(3/2^-, 1/2^+)$	232(6)	232(6)	37(14)
σ_{inc} (^{9}Be(^{32}Mg,^{29}Ne)) = 0.25(3) mb			

Chapter 6

Discussion

The study of the γ-ray spectroscopy of neutron-rich $^{28\text{-}30}$Ne is aimed at investigating structure changes in the neon isotopes while approaching the island of inversion. Here we compare our data presented in Chapter 5 to level energies, transition rates, and production cross sections obtained from shell-model and reaction-model codes described in Chapters 2 and 3.

6.1 ^{28}Ne

MCSM calculations using the SDPF-M interaction predict the N = 18 ^{29}Na and ^{28}Ne isotones to have ~50% 0p0h ("zero particle, zero hole") and ~50% 2p2h ("two particle - two hole") admixtures in their ground states and, in that sense, they are calculated to define the transition to the island of inversion. Data on ^{29}Na [Tri05] show a higher density of excited states compared with a USD-A [Bro07a] shell-model calculation, which assumes a pure sd-shell configuration, and support the interpretation of a sizable 2p2h ground-state component. Does ^{28}Ne also display evidence for a reduced N = 20 shell gap?

The drop in the energy of the lowest 2^+-spin state, $E(2_1^+)$, from ~2000 keV in ^{26}Ne to ~1300 keV in ^{28}Ne has been suggested [Pri99, Bel00] as evidence for a significant 2p2h intruder admixture when approaching N = 20. A similar phenomenon has been observed

in the neutron-rich Mg isotopes, where the $E(2_1^+)$ drops from ~1500 keV in ^{28}Mg and ^{30}Mg [ENS07] to $E(2_1^+)$ = 885.7 keV in the N = 20 ^{32}Mg [Mot95, Aza02a]. In addition, the relatively large B(E2; $0_1^+ \rightarrow 2_1^+$) = 269(136) e^2fm^4 in ^{28}Ne obtained from an early Coulex measurement [Pri99] is in agreement with the predicted 270 e^2fm^4 given by SDPF-M calculations [Uts07], and also supports the idea of a reduced N = 20 shell gap with large intruder admixtures in the ^{28}Ne ground state. However, recent measurements [Iwa05, Dom06a, Dom06b] gave a smaller value of B(E2; $0_1^+ \rightarrow 2_1^+$) = 132(23) e^2fm^4 and suggested that the proton and neutron matter distributions in ^{28}Ne are far smaller than expected for an island of inversion nucleus and more consistent with a predominantly 0p0h configuration (so-called large shell gap interpretation). The fact that both $E(2_1^+)$ and B(E2; $0_1^+ \rightarrow 2_1^+$) values are low has been interpreted as a sign of "suppressed collectivity" [Iwa05], characteristic of a nucleus lying at the border of the island of inversion. An interpretation is offered [Iwa05] where the 0_1^+ ground state is mainly spherical while the 2_1^+ state is deformed, and the small overlap in their wave functions would be responsible for the low B(E2) value. According to calculations by [Rod03], the ground state of ^{28}Ne is slightly deformed, signaling a transition to the island of inversion, and shape coexistence is possible. It was also found that by adopting smaller effective charges [Dom06a, Dom06b], SDPF-M calculations can also reproduce the ^{28}Ne transition probabilities, leading to a situation where the ^{28}Ne data can be interpreted within both sd and sd-pf model spaces, depending on the choice of effective charges.

While it appears the transition matrix elements in ^{28}Ne may be interpreted in either a large shell-gap (USD-A) or reduced shell-gap (SDPF-M) scenario, a reduced N = 20 gap will naturally lead to low-lying intruder states, specifically an excited 0_2^+, absent in the

large N = 20 shell gap assumption (USD). In addition, differences in the intruder contents given in OXBASH (USD) and MCSM (SDPF-M) calculations will result in different population of ^{28}Ne states in the knockout reactions.

6.1.1 ^{28}Ne Spectrum of Excited States and γ-Ray Decays

Figure 6.1 shows the experimental level scheme of ^{28}Ne together with those predicted by shell-model calculations using the USD-A interaction (sd-shell orbitals) [Bro07a] and the SDPF-M interaction (which allows cross-shell mixing between sd and pf shells) [Uts07]. Since both the one-proton knockout (^{29}Na-1p) and two-proton knockout (^{30}Mg-2p) reactions led to the same spectrum of excited states in ^{28}Ne, for simplicity we show only (Fig. 6.1) the spectrum corresponding to the ^{29}Na-1p reaction.

The SDPF-M calculation predicts a second 0_2^+ state at ~2.2 MeV with a 50-50% mixture of 0p0h-2p2h configurations (Fig. 6.1) and its observation would provide important confirmation of the validity of these SDPF-M calculations and a measure of the N = 20 gap. The γ-γ coincidence data show a cascade of three consecutive rays at 891, 1707, and 1306-keV (Figs. 5.2 and 5.3) and rule out the interpretation [Bel05] that the ~900-keV γ ray directly feeds the 2_1^+, thereby removing the existing evidence for an intruder 0_2^+ state at the low excitation energy of ~2229 keV (Fig. 5.4).

From the deduced level scheme, the cascade of γ rays: 891, 1707, and 1306 keV, suggests a minimum of three excited states in ^{28}Ne, which could in principle correspond to either a predominantly 0p0h (USD-A calculation) or 50% 2p2h intruder configuration (MSCM calculation) for ^{28}Ne.

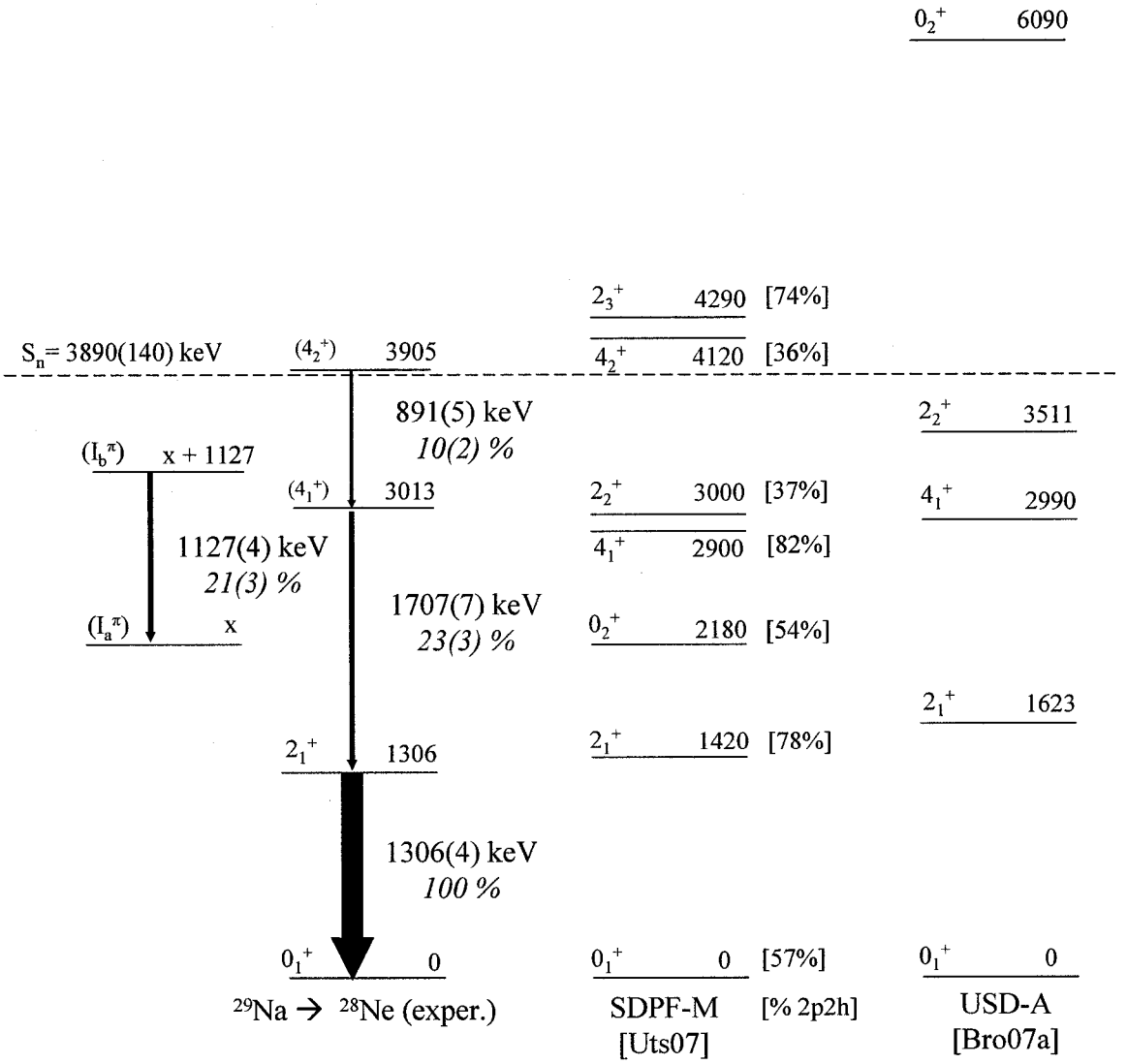

Figure 6.1 Comparison of the experimental level scheme of ^{28}Ne produced by one-proton knockout of ^{29}Na and level schemes predicted by MCSM using the SDPF-M interaction [Uts07] and by OXBASH using the USD-A interaction [Bro07a]. Each level is labeled with its energy in keV (on the right) and its spin/parity assignment (on the left). The spin/parity value is in parenthesis when tentative. For the SDPF-M predictions the numbers in brackets indicate the %2p2h composition of that level (the remainder being %0p0h). Each γ-ray transition is labeled with its energy in keV and its transition intensity (%). The thickness of the arrows is roughly proportional to the corresponding γ-ray transition intensity. The figure includes also the location of the neutron separation energy given by [ENS07].

The shell-model calculation using the USD-A interaction [Bro07a] predicts three levels below the neutron separation energy (Fig. 6.1). The experimental level scheme differs from the USD-A prediction fundamentally in the location of the 2_1^+ state: ~1300 keV in the experiment compared to ~1600 keV in USD-A. Within a 0p0h (USD-A) interpretation the 891-1707-1306 keV γ rays would correspond to the $2_2^+ \rightarrow 4_1^+ \rightarrow 2_1^+ \rightarrow 0_1^+$ decay sequence. However, because the $2_2^+ \rightarrow 2_1^+$ M1-transition branch is calculated to carry ~100% of the 2_2^+ decay rate [Bro07b], then the 891-keV γ ray cannot be associated with the $2_2^+ \rightarrow 4_1^+$ transition and USD-A is not consistent with the experimental observation of the cascade. In addition, the observation of an isolated 1127-keV γ ray (Fig. 6.1) implies the existence of two additional states below ~3.9 MeV (the neutron separation energy). The existence of these additional states is outside the predictions using the USD-A model space and favors the MCSM calculation with its higher density of states due to the reduced N = 20 shell gap. Finally, the experimental finding of the 2_1^+ at ~1306 keV is more consistent with the MCSM prediction of 1420 keV rather than the 1623-keV calculated using USD-A.

The only experimental excited level in ^{28}Ne with confident assignments of spin and parity is the ~1306-keV 2_1^+ state, measured before in Coulomb excitation [Pri99]. Plausible spin/parity assignments for the 3013- and 3905-keV levels (Fig. 6.1) can be proposed by comparing the experimental level scheme with the energies and transition strengths predicted by MCSM. MCSM predicts the following M1 transitions to dominate the decays of the 2_2^+, 4_2^+, and 2_3^+ states: the $2_2^+ \rightarrow 2_1^+$, $4_2^+ \rightarrow 4_1^+$, and $2_3^+ \rightarrow 2_1^+$ have calculated M1/E2 branching ratios of ~99, 97, and 97%, respectively (Table 6.1).

Table 6.1 **B(E2↓) and B(M1↓) transition strengths and E_γ(keV) γ-ray energies in ^{28}Ne, calculated by MCSM using the SDPF-M interaction [Uts07].** The table also includes derived transition probabilities $T_{fi}(s^{-1})$ and partial lifetimes τ_{fi}(ps), i.e., the lifetimes associated to the decay through a particular transition from a given initial state i to a final state f. When a state decays through more than one branch, branching ratios are also included. The shaded areas correspond to the transitions predicted to be observable experimentally, according to their calculated partial lifetimes and branching ratios (the latter when applicable).

Transition $\lambda L\downarrow; I_i^+ \rightarrow I_f^+$	B(E2↓) or B(M1↓)	E_γ (keV)	$T_{fi}(s^{-1})$	τ_{fi}(ps)	BR_{fi}(%)
E2↓; 2_1^+ --> 0_1^+	53.6	1420	3.8E+11	3	
E2↓; 0_2^+ --> 2_1^+	52	760	1.6E+10	62	
E2↓; 4_1^+ --> 2_1^+	74.44	1480	6.5E+11	1.5	
E2↓; 2_2^+ --> 4_1^+	11	100	1.3E+05	7.4E+06	0.00%
E2↓; 2_2^+ --> 0_2^+	39.2	820	1.8E+10	56	0.05%
E2↓; 2_2^+ --> 2_1^+	20	1580	2.4E+11	4	0.64%
M1↓; 2_2^+ --> 2_1^+	0.54	1580	3.7E+13	0.03	99.09%
E2↓; 2_2^+ --> 0_1^+	0.28	3000	8.3E+10	12	0.22%
E2↓; 4_2^+ --> 2_2^+	31.67	1120	6.8E+10	15	0.09%
E2↓; 4_2^+ --> 4_1^+	1.3	1220	4.3E+09	232	0.01%
M1↓; 4_2^+ --> 4_1^+	2.51	1220	8.0E+13	0.01	99.67%
E2↓; 4_2^+ --> 2_1^+	1.11	2700	2.0E+11	5	0.24%
E2↓; 2_3^+ --> 4_2^+	18	170	3.1E+06	3.2E+05	0.00%
E2↓; 2_3^+ --> 2_2^+	5.5	1290	2.4E+10	42	0.02%
M1↓; 2_3^+ --> 2_2^+	0.004	1290	1.5E+11	7	0.10%
E2↓; 2_3^+ --> 4_1^+	0.2	1390	1.3E+09	786	0.00%
E2↓; 2_3^+ --> 0_2^+	0.82	2110	4.2E+10	24	0.03%
E2↓; 2_3^+ --> 2_1^+	14	2870	3.3E+12	0.3	2.24%
M1↓; 2_3^+ --> 2_1^+	0.35	2870	1.5E+14	0.007	97.42%
E2↓; 2_3^+ --> 0_1^+	0.16	4290	2.9E+11	4	0.19%

Comparing the experimental level energies with those predicted by MCSM, the 3013-keV level is likely to be either the 4_1^+ or the 2_2^+ and the 3905-keV level can be either the 4_2^+ or the 2_3^+. The only possible way of having the observed three γ-ray cascade fit within the MCSM predictions is the case where the 3013-keV level corresponds to the 4_1^+ and the 3905-keV to the 4_2^+; both spin assignments are tentatively assigned within parentheses in Fig. 6.1. In particular it can be ruled out that the 3013-keV level corresponds to the 2_2^+ state because there are no levels above that would feed it by the 891-keV γ ray.

The isolated and relatively strong γ-ray transition at an energy of 1127 keV is shown in Fig. 6.1 connecting levels labeled $I_b^\pi \rightarrow I_a^\pi$, where the level I_a^π is located at an energy x (keV) above the ground state. The 1127-keV transition is not in coincidence with the other main transitions (Figs. 5.2 and 5.3) and its nature remains a puzzle. We now consider the possibility that the 1127-keV transition connects the $2_2^+ \rightarrow 0_2^+$ states (and that a γ-ray decay of the 0_2^+ state is isomeric or energetically unfavored). The 0_2^+ and the 2_2^+ states are predicted by MCSM and are not accounted for by the three γ-ray cascade.

The 2_2^+ level has three possible decay branches: $2_2^+ \rightarrow 0_2^+$, $2_2^+ \rightarrow 0_1^+$, and $2_2^+ \rightarrow 2_1^+$, as shown in Fig. 6.2. For the 1127-keV γ ray to correspond to the $2_2^+ \rightarrow 0_2^+$ transition and for this assumption to be consistent with the observed data, then the other possible decay modes must be far weaker. MCSM calculations with the SDPF-M interaction [Uts07] provide B(E2) and B(M1) values (Table 6.1) that can be used to derive a range of possible values of x (excitation energy of the 0_2^+ state) compatible with the assumption that the 1127-keV transition corresponds to the $2_2^+ \rightarrow 0_2^+$ decay.

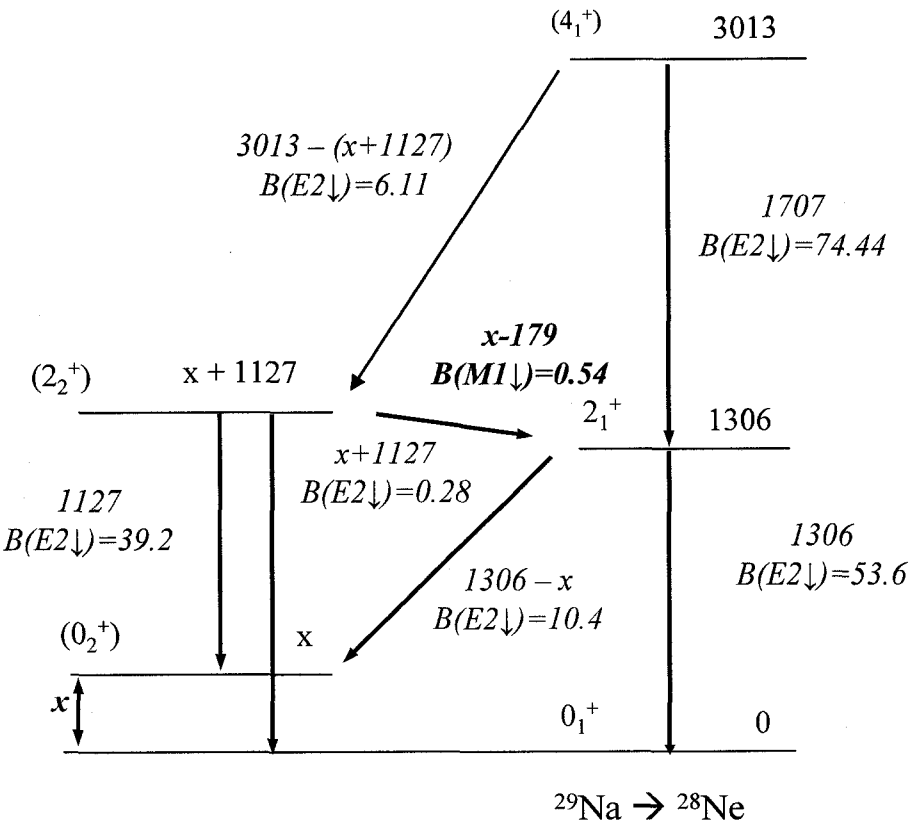

Figure 6.2 Experimental γ-ray transitions in ^{28}Ne (produced by ^{29}Na) and calculated (SDPF-M) values of B(E2) and B(M1) transition strengths.

For the calculated values B(M1; $2_2^+ \rightarrow 2_1^+$) = 0.54 μ_N^2, B(E2; $2_2^+ \rightarrow 0_2^+$) = 39.2 e^2fm^4, and B(E2; $2_2^+ \rightarrow 0_1^+$) = 0.28 e^2fm^4, the 2_2^+ cannot lie ~1500 keV above the 2_1^+ state, as given in the MCSM calculation (Fig. 6.1), because in that case the $2_2^+ \rightarrow 2_1^+$ M1 decay would dominate the assumed 1127-keV $2_2^+ \rightarrow 0_2^+$ transition so that the 1127-keV γ ray would not be observed. The 1127-keV γ ray cannot correspond to the $2_2^+ \rightarrow 2_1^+$ decay since this would require a coincidence with the 1306-keV $2_1^+ \rightarrow 0_1^+$ transition, which is not observed. Figure 6.3 gives the branching ratio of the M1 transition, $2_2^+ \rightarrow 2_1^+$, which is the probability (%) of decay of the 2_2^+ state through the M1 transition with respect to

the total probability of decay of the 2_2^+ via any of the three decay modes. The M1 branching ratio is plotted as a function of the energy (z, keV) of the M1 γ-ray transition, for the calculated B(M1) = 0.54 μ_N^2 and also for the case where the B(M1) was 10 times weaker, B(M1) = 0.054 μ_N^2. The 2_2^+ state can be above (z > 0) or below (z < 0) the 2_1^+ state. Using the conservative assumptions that: (a) an M1 transition would be observed when its branching ratio was above 50%, and (b) the B(M1) value was 0.054 μ_N^2, i.e., ten times weaker than its prediction by SDPF-M, it is possible to set an upper limit to the M1 γ-ray energy of approximately z = 500 keV (Fig. 6.3). In other words, the 2_2^+ state cannot lie more than ~500 keV above the 2_1^+ state and therefore x (keV) ≈ z + 200, the excitation energy of the 0_2^+ state, would need to be a maximum of ~700 keV and not ~2.2 MeV as predicted by the MCSM calculations.

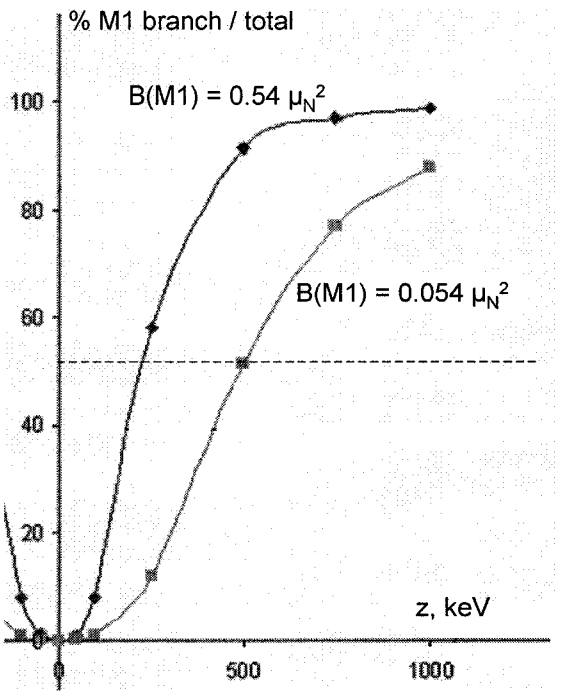

Figure 6.3 Calculated branching ratio (%) of M1 decay from (2_2^+) → 2_1^+ vs. the M1 γ-ray transition energy z in ^{28}Ne, assuming either B(M1) is 0.54 μ_N^2 calculated using SDPF-M [Uts07] or B(M1) is ten times weaker, i.e., B(M1) is 0.054 μ_N^2.

We conclude that the 1127-keV γ ray cannot correspond to the $2_2^+ \rightarrow 0_2^+$ transition and at the same time be consistent with the MCSM calculation, which predicts a 2.2-MeV 0_2^+ state with 50% 2p2h intruder content.

The fact that MCSM calculations predict the 0_1^+ and 0_2^+ states in ^{28}Ne to have similar configurations implies that they would have similar cross sections for direct population in the 1p and 2p knockout reactions; we can use this to provide an additional constraint to the location of the 0_2^+ state. The ^{28}Ne 0_1^+ ground state has a direct production cross section of ~0.4 mb in the ^{30}Mg-2p reaction; assuming a similar cross section for the 0_2^+ state would give ~400 counts in a $0_2^+ \rightarrow 2_1^+$ γ-ray peak. The B(E0; $0_2^+ \rightarrow 0_1^+$) transition is estimated to be far weaker than the B(E2; $0_2^+ \rightarrow 2_1^+$) and the E0 decay branch can be neglected. MCSM calculations give a transition rate B(E2; $0_2^+ \rightarrow 2_1^+$) = 52 e^2fm^4 (Table 6.1) and the predicted 760-keV $0_2^+ \rightarrow 2_1^+$ transition would then have a half-life of ~60 ps, which could be observed in our measurement. On the other hand, a 400-keV γ-ray would then have a half-life of ~1 ns (placing its decay far from the target and significantly altering the Doppler reconstruction) and would not be observed in this measurement. This analysis sets an upper limit of E(x) < 1700 keV for the energy of the 0_2^+ state, if it were directly populated in the ^{30}Mg-2p reaction.

Finally, the 1127-keV could not feed the 0_1^+ ground state directly because in that case it should have been observed in a ^{28}Ne Coulomb excitation experiment [Pri99].

To summarize, while the location of the 0_2^+ state in ^{28}Ne remains undetermined, the properties of observed excited states favor an interpretation based on the MCSM calculation with its higher density of states due to a reduced N = 20 shell gap. If the 0_2^+ state is lower than predicted by MCSM by a few hundred keV it could potentially be isomeric, and a $0_2^+ \rightarrow 2_1^+$ transition would remain undetected in our experiment, were the 0_2^+ to be directly populated. The 1127-keV transition (and the levels it connects) remains a puzzle that cannot be explained within the MCSM calculation given in Fig. 6.1 without significant changes to the location of the 2_2^+ and 0_2^+ states beyond those expected from shell-model uncertainties.

6.1.2 ^{9}Be(^{29}Na,^{28}Ne) One-Proton Knockout

Table 6.2 and Figs. 6.4 and 6.5 compare the experimental and theoretical cross sections for the direct population of states in ^{28}Ne in the ^{9}Be(^{29}Na,^{28}Ne) one-proton knockout reaction. While direct knockout reaction cross section measurements are sensitive to the final state wave functions and could discriminate between a 0p0h or 2p2h configuration, two aspects of the present measurements make such an analysis difficult. First, the ^{28}Ne fragments from the ^{29}Na-1p reaction were not centered on the S800 focal plane leading to a large uncertainty in the S800 acceptance and hence large errors in the measured cross sections. Second, only calculated ^{29}Na-1p cross sections using spectroscopic factors derived from USD wave functions are available and therefore it was not possible to directly compare the cross section data with MCSM wave functions. Nevertheless some comparison is possible and summarized as follows:

Table 6.2 **Comparison of experimental and theoretical fractional populations and partial cross sections of ground and excited states in ^{28}Ne produced in the one-proton knockout reaction ^{9}Be(^{29}Na,^{28}Ne).** The theoretical energy levels used in the reaction theory were given by a shell-model calculation using the USD-A interaction [Bro07a].

Experiment				Theory			
Level I^{π}	Level energy, E_i (keV)	Fractional population of level i, b_i	Partial cross section, σ_i (mb)	Level I^{π}	Level energy, E_i (keV)	Fractional population of level i, b_i	Partial cross section, σ_i (mb)
0_1^+	0	0.15(3)*	2(1)*	0_1^+	0	0.01	0.31
2_1^+	1306(4)	0.55(7)	8(4)	2_1^+	1623	0.688	21.46
(4_1^+)	3013(8)	0.09(2)	1.2(7)	4_1^+	2990	0.234	7.32
(4_2^+)	3905(9)	0.07(2)	1.0(5)	2_2^+	3511	0.07	2.12
I^{π}_b	x + 1127(4)	0.15(2)	2(1)				
Total		1	14(7)			1	31.22
$\sigma_{inc}^{exp}(^{9}Be(^{29}Na, ^{28}Ne)) = 14(7)$ mb							
$\sigma_{inc}^{theo}(^{9}Be(^{29}Na, ^{28}Ne)) = 31.22$ mb							

*These numbers include any direct feeding of the I_a^{π} state.

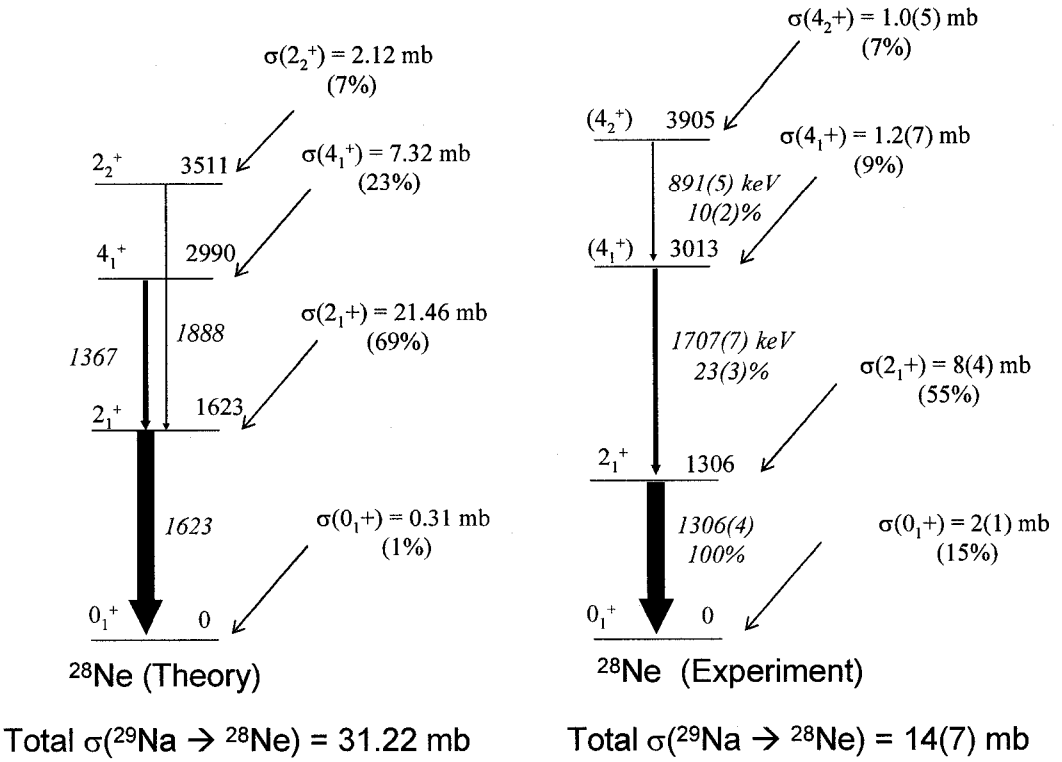

Figure 6.4 Comparison of experimental and theoretical fractional populations and partial cross sections of ground and excited states in ^{28}Ne produced in the one-proton knockout reaction ^{9}Be(^{29}Na,^{28}Ne).

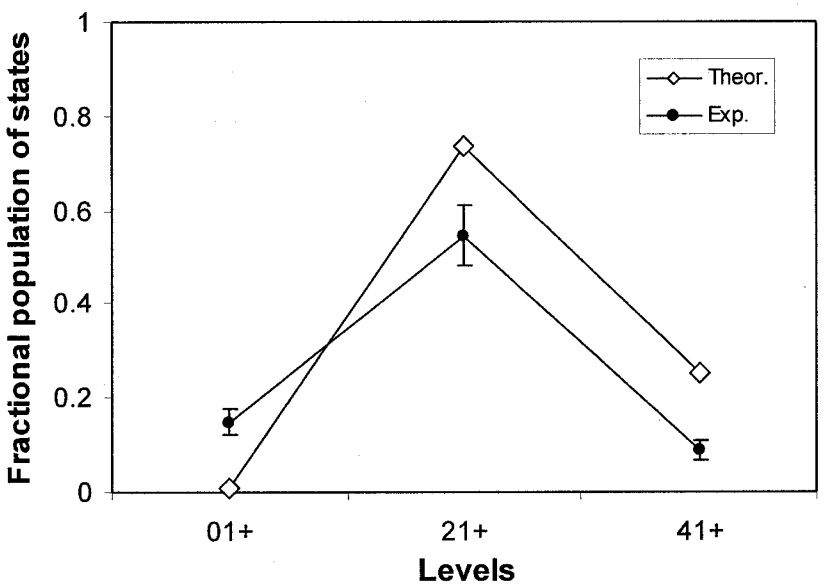

Figure 6.5 Comparison of experimental and theoretical fractional population of ground and excited states in ^{28}Ne produced in the one-proton knockout reaction ^{9}Be(^{29}Na,^{28}Ne).

- The inclusive cross section for the ^{9}Be(^{29}Na,^{28}Ne) reaction was measured to be 14(7) mb compared to the theoretical value of 31.22 mb. The experimental-to-theoretical reduction factor R_s = 0.5(3) is consistent with the reduction factor for single-nucleon knockout, R_s = 0.7, observed in similar measurements [Bro02, Han03, Gad04b]. However, as noted, the ~50% error means it is not possible to rule out a difference in the neutron intruder contents between ^{29}Na and ^{28}Ne as predicted by MCSM calculations, which would likely manifest themselves as a $R_s < 0.7$ if only USD wave functions are used.
- The fraction of direct population to the 0_1^+, 2_1^+, and 4_1^+ states calculated using USD wave functions is shown in Fig. 6.5, where the 2_1^+ state receives the majority of feeding and direct population of the 0_1^+ is negligible. The experimental and theoretical data are in qualitative agreement (under the assumption that the experimental 1707-keV transition is the $4_1^+ \rightarrow 2_1^+$ decay); the 2_1^+ state is the one predominantly populated in the experiment with a fractional population of 0.55(7) compared to 0.69 in the calculation. The experimental value for the fractional population of the 4_1^+ state, $b(4_1^+)$ = 0.088, is ~1/3 of the calculated value and is closer to the value calculated for the 2_2^+ state. However, these differences between calculated and measured partial cross sections for the 4_1^+ (and 0_1^+) may reflect the fact that the σ(calc.) values were derived using USD wave functions and in the absence of SDPF-M wave functions it is not possible to reliably compare σ(exp.) with σ(calc.) to extract structure information in the ^{29}Na-1p reaction.

6.1.3 ^{9}Be(^{30}Mg,^{28}Ne) Two-Proton Knockout

The experimental and calculated ^{9}Be(^{30}Mg,^{28}Ne) two-proton knockout cross sections are compared in Table 6.3 and Figs. 6.6 and 6.7. The measured ^{30}Mg-2p inclusive cross section for a ^{30}Mg beam energy of ~104 MeV/A is 0.8(2) mb. This measurement is consistent with recently published data [Baz03b] on the 2p knockout of a ~88.5 MeV/A ^{30}Mg beam where the cross section was measured to be 0.49(5) mb.

Table 6.3 Comparison of experimental and theoretical fractional populations and partial cross section of ground and excited states in ^{28}Ne produced in the two-proton knockout reaction ^{9}Be(^{30}Mg,^{28}Ne).

Experiment				Theory			
Level I^{π}	Level energy, E_i (keV)	Fractional population of level i, b_i	Partial cross section, σ_i (mb)	Level I^{π}	Level energy, E_i (keV)	Fractional population of level i, b_i	Partial cross section, σ_i (mb)
0_1^+	0	0.5(3)*	0.4(2)*	0_1^+	0	0.36	1.107
2_1^+	1304(5)	0.19(4)	0.16(4)	2_1^+	1785	0.13	0.399
(4_1^+)	3008(9)	0.14(4)	0.11(4)	4_1^+	3300	0.37	1.144
(4_2^+)	3903(10)	0.09(3)	0.08(3)	2_2^+	3678	0.14	0.434
I^{π}_b	x + 1117(7)	0.05(3)	0.05(2)				
Total		1	0.8(2)			1	3.084
Summed 2^+ (theory)						0.27	0.833
$\sigma_{inc}^{exp}(^{9}Be(^{30}Mg,^{28}Ne)) = 0.8(2)$ mb $\sigma_{inc}^{theo}(^{9}Be(^{30}Mg,^{28}Ne)) = 3.084$ mb							

*These numbers include any direct feeding of the I_a^{π} state.

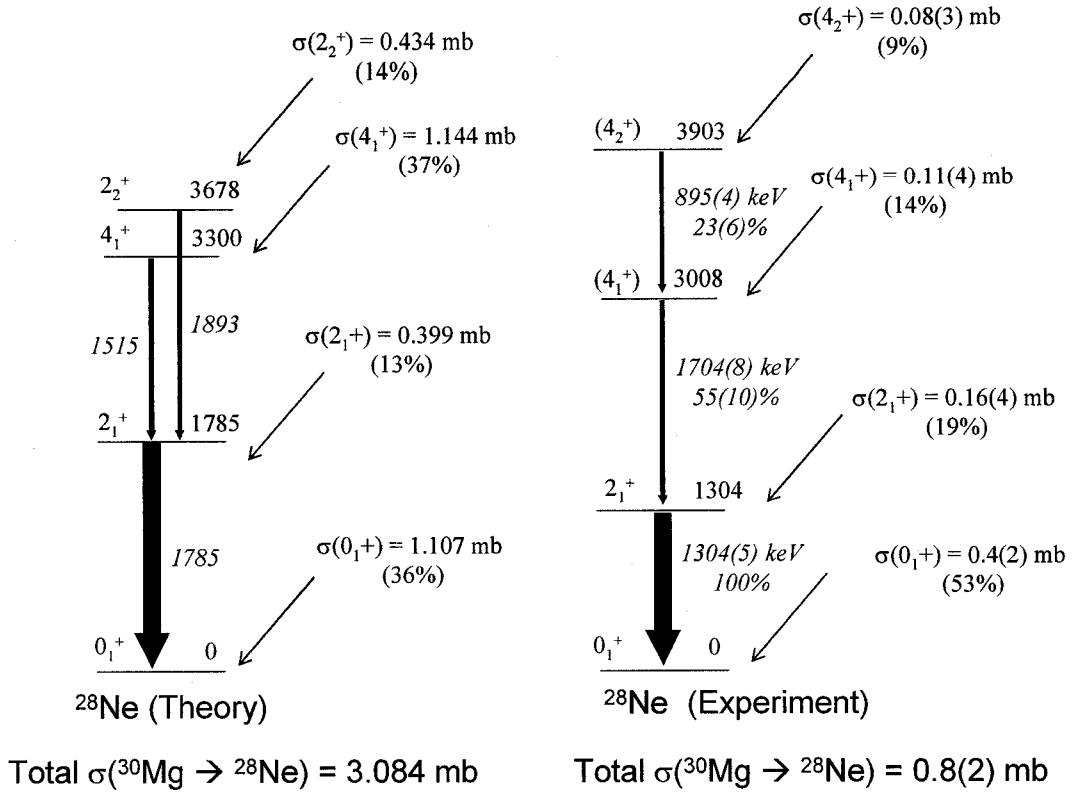

Figure 6.6 Comparison of experimental and theoretical fractional populations and partial cross sections of ground and excited states in ^{28}Ne produced in the two-proton knockout reaction ^{9}Be(^{30}Mg,^{28}Ne).

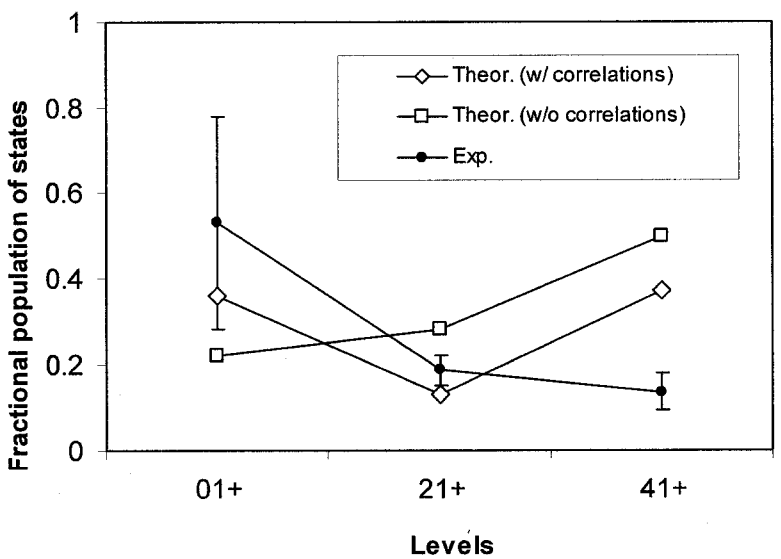

Figure 6.7 Comparison of experimental and theoretical fractional population of ground and excited states in ^{28}Ne produced in the two-proton knockout reaction ^{9}Be(^{30}Mg,^{28}Ne).

The calculated inclusive ^{30}Mg-2p cross section is 3.084 mb. The comparison of the experimental and the model inclusive cross sections results in a reduction factor R_s = 0.27(6). Reduction factors for two-proton knockout of moderately neutron-rich nuclei have been found to be on the order of ~0.5 [Tos06b, Yon06]. The calculated ^{30}Mg two-proton knockout cross section used USD wave functions. The USD wave functions are very likely to be realistic regarding the modeling of the protons, which are assumed to be removed from the $1d_{5/2}$ orbital. However, using USD wave functions for the neutrons is not likely to be a good assumption, as a fraction of the neutrons in ^{28}Ne is expected to be located in some of the pf-shell levels (consistent with the discussion on the ^{28}Ne level scheme). Under the assumption that (a) the ^{30}Mg ground state is ~100% 0p0h and (b) the neutrons behave as passive spectators, then the reduced σ(exp) says that ^{28}Ne and ^{30}Mg have differing neutron configurations beyond USD. The additional 50% reduction in R_s in ^{30}Mg $\rightarrow$ ^{28}Ne compared to other 2p knockout reactions can be interpreted as a measure of the 2p2h content in the ^{28}Ne ground state. This suggests a 50% 2p2h intruder content in ^{28}Ne.

Regarding the fractional populations of the ground state and the different excited states, both experimental data and the model (assuming the existence of two-proton correlations) agree reasonably well on the fractional population of the ground state, with an experimental value of 0.5(3), consistent with a theoretical prediction of 0.36. The experimental fractional population of the 2_1^+ state is 0.19(4), compared to a theoretical value of 0.13. The experimental fractional population of the 4_1^+ state is 0.14(4), compared to a theoretical value of 0.37. These fractional populations are included in Table 6.3 and Figs. 6.6 and 6.7. The enhanced population of the 0_1^+ ground state is due to

two-nucleon correlations. Cross sections calculated without correlations are also shown in Fig. 6.7 for comparison.

6.2 ^{30}Ne

Given that N = 20 is a magic number within the conventional shell model, the even-even ^{32}Mg and ^{30}Ne N = 20 isotones should display a large E(2_1^+) energy and low B(E2; $0_1^+ \rightarrow 2_1^+$). However, in ^{32}Mg the E(2_1^+) has been measured to have a low value of 885.7 keV [Mot95, Aza02a], and in ^{30}Ne, the E(2_1^+) value is seen to have an even smaller energy value of ~791 keV [Yan03]. These data have been used to infer that there is an enhancement of deformation as the neutron excess increases in the N = 20 isotones, and that ^{30}Ne belongs to the island of inversion. This energy value (791 keV) is the lowest among the 2_1^+ energies of even-even N=20 isotones, suggesting a large deformation.

Regarding transition strengths, the B(E2; $0_1^+ \rightarrow 2_1^+$) in ^{32}Mg has been measured to be large and equal to 454(78) e^2fm^4 [Mot95]; from this quantity a large quadrupole deformation parameter $\beta \sim 0.5$ has been deduced [Mot95]. The transition strength B(E2; $0_1^+ \rightarrow 2_1^+$) in ^{30}Ne has been measured to be large with a value of 460(270) e^2fm^4 [Yan03], which compares well with the SDPF-M prediction of 348 e^2fm^4 [Uts07].

Earlier theoretical work [Rod03] concluded that the ground state of ^{30}Ne is slightly deformed and that shape coexistence is possible. According to [Rod03], the ground state of the N = 20 nucleus ^{30}Ne is not as deformed as that of its ^{32}Mg isotone; their 2_1^+ deformations are however predicted to be almost identical.

Even though there is already experimental data on the E(2_1^+) and B(E2; $0_1^+ \rightarrow 2_1^+$) of ^{30}Ne, which suggest a large intruder content of the 0_1^+ and 2_1^+ states, there are still no

data on additional states which would provide valuable information on the structure and degree of collectivity of ^{30}Ne. Also, the energy of the 2_1^+ published so far [Yan03] was obtained in a proton inelastic scattering experiment with relatively low statistics and therefore large uncertainty: $E(2_1^+)$ = 791(26) keV [Yan03].

6.2.1 ^{30}Ne Spectrum of Excited States and γ-Ray Decays

The experimental level energies are compared to calculations in Fig. 6.8. Both MCSM (SDPF-M interaction) and OXBASH shell-model calculations with two neutrons in the pf-shell (a pure or 100% 2p2h configuration for the ground state and all excited states, in Fig. 6.8) show good agreement with the data.

The observation of the transition at 792(4) keV connecting the (2_1^+) to the 0_1^+ state is an important confirmation of a previously reported value which was observed in a proton inelastic scattering experiment [Yan03]. It is interesting to note that this energy value (~792-keV) is the lowest of all the 2_1^+ energy levels in neighboring even-even N = 20 isotones and is evidence for a collective state based on a deformed 2p2h ground state. Shell model calculations using the USD-A interaction greatly overestimate the experimental value of the (2_1^+) energy.

The data provide the first observation of a second γ-ray transition with an energy of 1443(11) keV and a relative intensity of 39(12)%.

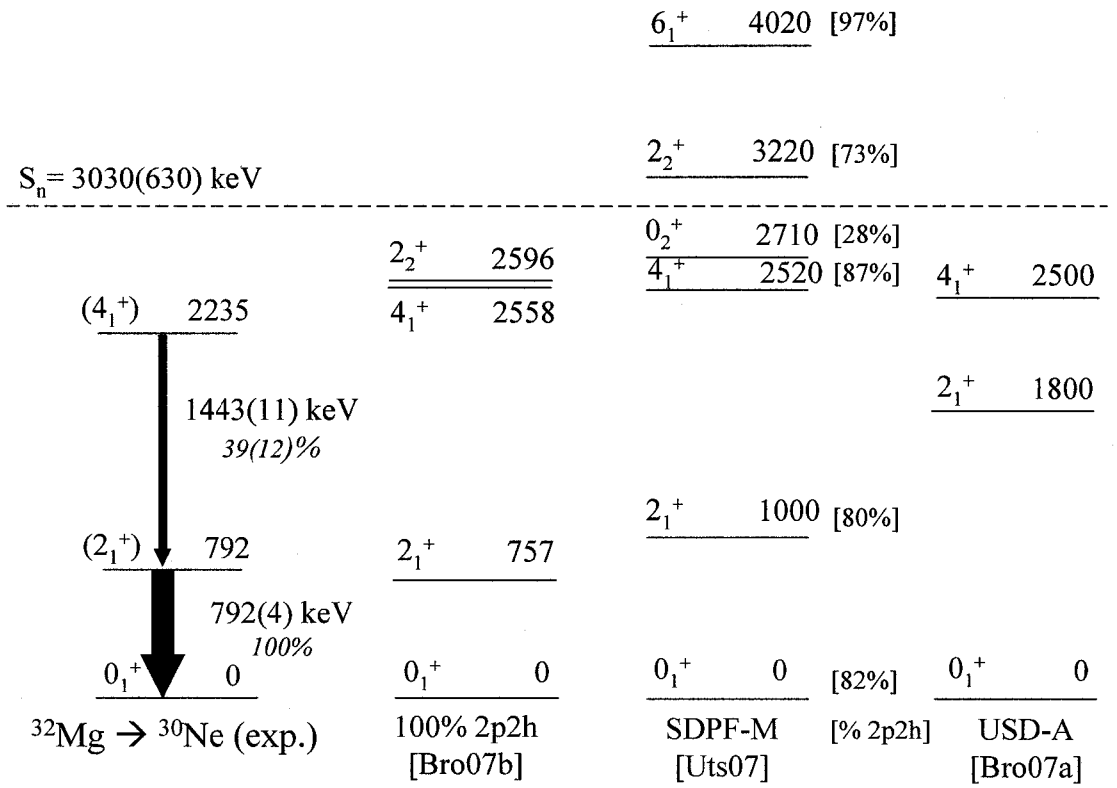

Figure 6.8 Comparison of the experimental level scheme of ^{30}Ne produced by two-proton knockout of ^{32}Mg and level schemes predicted by: OXBASH using 100% 2p2h configuration for all states [Bro07b], MCSM using the SDPF-M interaction [Uts07], and OXBASH using the USD-A interaction [Bro07a]. Each level is labeled with its energy in keV (on the right) and its spin/parity assignment (on the left). The spin/parity value is in parenthesis when tentative. For the SDPF-M predictions the numbers in brackets indicate the %2p2h composition of that level (the remainder being %4p4h). Each γ-ray transition is labeled with its energy in keV and its transition intensity (%). The thickness of the arrows is roughly proportional to the corresponding γ-ray transition intensity. The figure includes also the location of the neutron separation energy given by [ENS07].

While there is good evidence to assign the 792-keV γ ray to the $2_1^+ \rightarrow 0_1^+$ decay, the 1443-keV line could be from the $4_1^+ \rightarrow 2_1^+$ but could in principle also be from the decay of either the 2_2^+ or the 0_2^+ states with calculated energies around 2.5-3.0 MeV (Fig. 6.8) and it is not possible to assign a spin from energies alone. However, the properties of direct two-proton knockout from the $1d_{5/2}$ level can be used to constrain the data and assign spins as discussed in Section 6.2.2; based on the observed partial cross sections the 2235-keV state is assigned a spin 4_1^+.

Overall, the experimental ^{30}Ne spectrum is consistent with the SDPF-M model and 100%-2p2h calculations.

Table 6.4 includes transition rates obtained from calculated B(E2) and B(M1) values and energies; the calculations were performed with MCSM using the SDPF-M interaction [Uts07]. The reduced transition probability B(E2; $0_1^+ \rightarrow 2_1^+$) has been measured to be 460(270) e^2fm^4 [Yan03, Yan04], consistent with the calculated B(E2; $0_1^+ \rightarrow 2_1^+$) estimate of 348 e^2fm^4 using the MCSM model (which is listed as B(E2; $2_1^+ \rightarrow 0_1^+$) = 69.6 e^2fm^4 in Table 6.4 [Uts07]), and is not consistent with the B(E2; $0_1^+ \rightarrow 2_1^+$) value of 129 e^2fm^4 obtained with a model including only the sd shell [Bro07b].

Table 6.4 **B(E2↓) and B(M1↓) transition strengths and E_γ(keV) γ-ray energies in ^{30}Ne, calculated by MCSM using the SDPF-M interaction [Uts07].** The table also includes derived transition probabilities $T_{fi}(s^{-1})$ and partial lifetimes τ_{fi}(ps), i.e., the lifetimes associated to the decay through a particular transition from a given initial level i. When a state decays through more than one branch, branching ratios are also derived. The shaded areas correspond to the transitions predicted to be observable experimentally, according to their calculated partial lifetimes and branching ratios (the latter when applicable).

Transition $\lambda L\downarrow; I_i^+ \rightarrow I_f^+$	B(E2↓) (e^2fm^4) or B(M1↓)(μ_N^2)	E_γ (keV)	$T_{fi}(s^{-1})$	τ_{fi}(ps)	BR_{fi}(%)
E2↓; 2_1^+ --> 0_1^+	69.6	1000	8.5E+10	12	
E2↓; 4_1^+ --> 2_1^+	91.7	1520	9.1E+11	1.1	
E2↓; 0_2^+ --> 2_1^+	8.1	1710	1.5E+11	7	
E2↓; 2_2^+ --> 0_2^+	32.2	510	1.4E+09	734	0.05%
E2↓; 2_2^+ --> 4_1^+	0	700	0		0.00%
E2↓; 2_2^+ --> 2_1^+	28	2220	1.9E+12	0.5	70.63%
M1↓; 2_2^+ --> 2_1^+	0.004	2220	7.7E+11	1.3	29.31%
E2↓; 2_2^+ --> 0_1^+	0	3220	0		0.00%
E2↓; 6_2^+ --> 4_1^+	73	1500	6.8E+11	1.5	

6.2.2 ^{9}Be(^{32}Mg,^{30}Ne) Two-Proton Knockout

We can use the properties of direct two-proton (2p) knockout from the $1d_{5/2}$ level to constrain the data and assign spins. According to the two-proton knockout theory, the relative populations of states will be different because the 2p spatial overlaps are different for I = 0, 2, or 4 coupling [Tos06a].

Table 6.5 and Figs. 6.9 and 6.10 show the relative population of the ^{30}Ne ground and excited states in the 2p knockout reaction. The ground state is directly populated ~58% of the time, the 792-keV has about 26% direct population, and the 1443-keV γ ray (2235-keV level energy) has about 16%.

Table 6.5 Comparison of experimental and theoretical fractional populations and partial cross sections of ground and excited states in ^{30}Ne produced in the two-proton knockout reaction ^{9}Be(^{32}Mg,^{30}Ne).

Experiment				Theory			
Level I^{π}	Level energy, E_i (keV)	Fractional population of level i, b_i	Partial cross section, σ_i (mb)	Level I^{π}	Level energy, E_i (keV)	Fractional population of level i, b_i	Partial cross section, σ_i (mb)
0_1^+	0	0.58(10)	0.13(5)	0_1^+	0	0.572	0.626
(2_1^+)	792(4)	0.26(8)	0.06(3)	2_1^+	757	0.043	0.047
(4_1^+)	2235(12)	0.16(4)	0.04(2)	4_1^+	2558	0.286	0.313
				2_2^+	2596	0.099	0.108
Total		1	0.22(3)			1	1.094
Summed 2^+ (theory)						0.142	0.155

$\sigma_{inc}^{exp}(^{9}\text{Be}(^{32}\text{Mg},^{30}\text{Ne})) = 0.22(3)$ mb

$\sigma_{inc}^{theo}(^{9}\text{Be}(^{32}\text{Mg},^{30}\text{Ne})) = 1.094$ mb

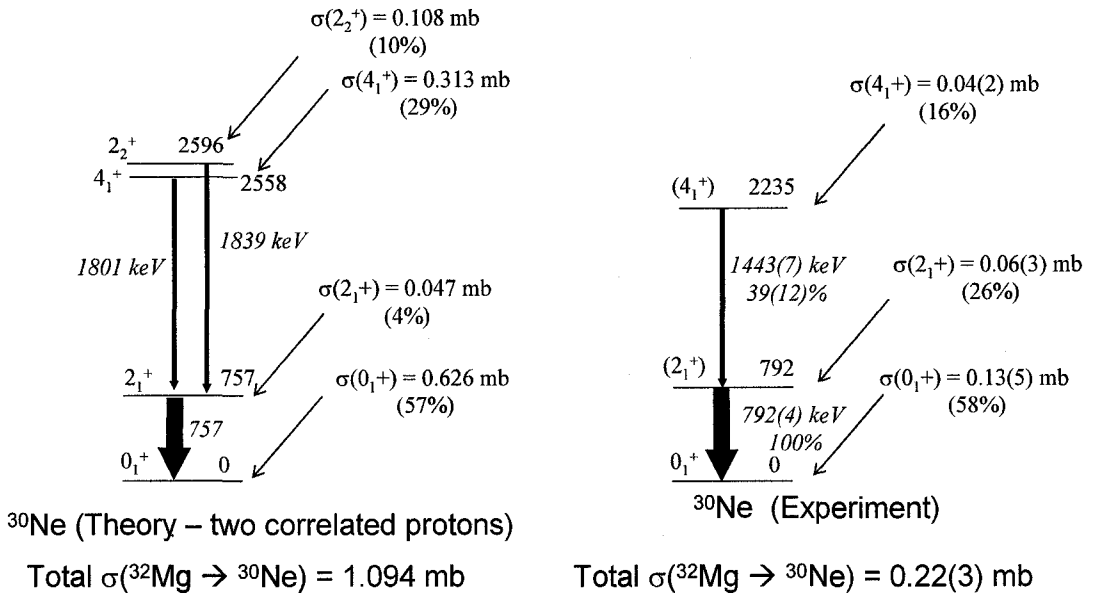

Figure 6.9 Comparison of experimental and theoretical fractional populations and partial cross sections of ground and excited states in ^{30}Ne produced in the two-proton knockout reaction ^{9}Be(^{32}Mg,^{30}Ne).

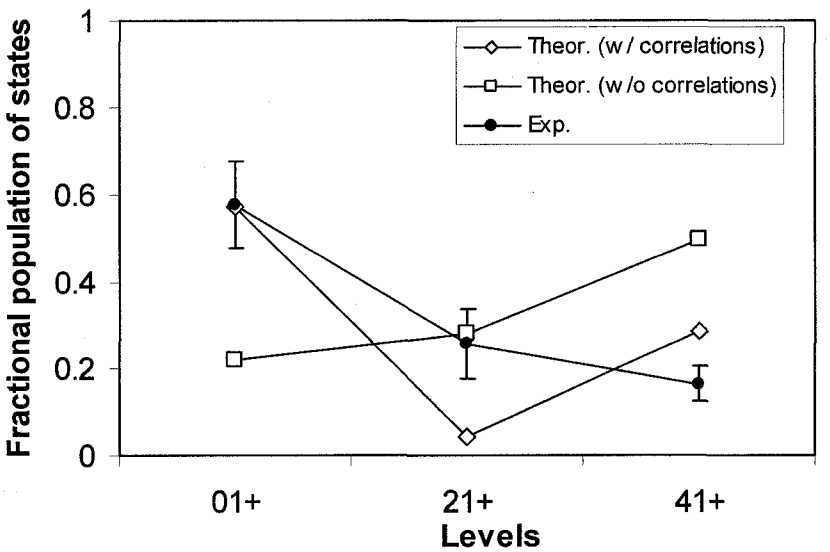

Figure 6.10 Comparison of experimental and theoretical fractional populations of ground and excited states in ^{30}Ne produced in the two-proton knockout reaction ^{9}Be(^{32}Mg,^{30}Ne).

A comparison with theory for 2p knockout from the $d_{5/2}$ orbital indicates that we should expect about a 60:40 split between ground state and excited state population, in agreement with observations. The relative enhancement of the 0^+ and the suppression of the 2^+ is a general feature of two-nucleon correlations (e.g., pairing) and was seen in other data sets (e.g., in the ^{30}Mg two-proton knockout described in Section 6.1.3). Moreover, the calculations predict a greater probability to knock out two protons coupled to I = 4 than I = 2; i.e., the summed I = 2 direct population is calculated to be ~15% while the 4^+ is ~30%.

Therefore, given the expectation for a significant population of the 4_1^+ state, and given the statistics in Fig. 5.6 we expect to observe a $4_1^+ \rightarrow 2_1^+$ transition in our data. The measured relative cross sections (γ-ray intensities) are consistent with the interpretation that the 1443-keV line corresponds to the decay of the 4_1^+. If, on the other hand, the 1443-keV γ ray was from the decay of the 2_2^+ then the total I = 2 direct population would be ~40%, with no appreciable direct 4_1^+ population. This is not expected from the two-proton knockout theory. Furthermore, although sd-pf calculations predict a second I = 0^+ state at 3 MeV, this 0_2^+ state is mainly 0p0h and one should expect little cross-section for direct two-proton knockout from a 2p2h intruder-dominated ^{32}Mg ground state.

In summary, the combination of experimental and theoretical γ-ray energies and intensities and cross section data support the interpretation that we have observed the decays from the $4_1^+ \rightarrow 2_1^+$ and the $2_1^+ \rightarrow 0_1^+$, which constitute a good case to fix the location of the deformed 4_1^+ state. This is the first experimental observation of an excited 4_1^+ state for a nucleus in the "island of inversion".

The experimental fractional populations in ^{28}Ne and ^{30}Ne produced in both ^{30}Mg and ^{32}Mg 2p knockout reactions do not agree well with a model which assumes that there are no correlations between the protons; this model predicts that the populations of the 0_1^+, 2_1^+, and 4_1^+ states are 0.22, 0.28, and 0.50. Both the experiment and the model with correlations agree instead on an enhanced population of the 0_1^+ ground state.

The inclusive cross section of the ^{9}Be(^{32}Mg,^{30}Ne) two-proton knockout reaction was measured to be 0.22(3) mb, while that predicted by the model [Tos07] (excluding the partial cross section to the 2_2^+ state) is 0.986 mb. The comparison of the experimental and the model inclusive cross sections results in a reduction factor R_s = 0.23(3). This reduction factor is similar to the one observed in the ^{9}Be(^{30}Mg,^{28}Ne) in this work.

In recent literature on two-proton knockout [Tos06b, Yon06] it was reported that, while the measured relative partial cross sections agree with theory, the measured inclusive cross section is consistently lower than predicted by theory. Fig. 6.11 depicts the "reduction factor" (ratio of the experimental to the calculated inclusive cross section) for a number of two-nucleon knockout reactions that were recently investigated. Previous two-nucleon knockout data yielded an R_s factor of ~0.5 between experiment and theory; our data yield an additional reduction factor of ~2, so that R_s ~ 0.25. The origin of this difference is of interest. If we consider the R_s ~0.5 value seen in other measurements to be an overall "normalization", then the extra reduction seen in our data could be used to provide information on the ^{32}Mg and ^{30}Ne wave functions. The observed additional reduction factor can be postulated to be due to differences in the neutron intruder configurations.

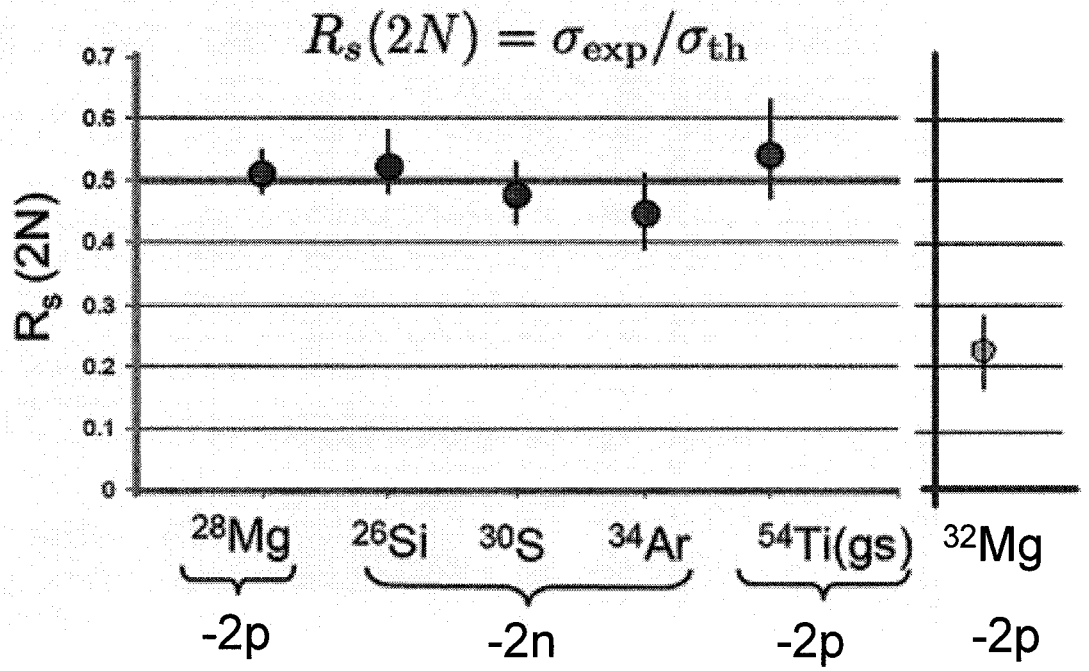

Figure 6.11 Experimental-to-theoretical cross section ratios (or reduction factors $R_s = \sigma^{exp}/\sigma^{theor}$) observed in a number of two-nucleon knockout experiments. The values for two-nucleon knockout from ^{28}Mg, ^{26}Si, ^{30}S, ^{34}Ar and ^{54}Ti are taken from [Tos07].

The shell-model wave functions used to calculate the two nucleon amplitudes (for input to the reaction code used to model the ^{32}Mg → ^{30}Ne 2p knockout reaction) were derived using full 2p2h configurations with two holes in the sd-shell and two particles in the pf-shell [Bro07b].

MCSM calculations predict different neutron configurations for ^{32}Mg and ^{30}Ne; ^{30}Ne has more 4p4h component and has larger occupancy of the $p_{3/2}$-orbital in the pf-shell compared with ^{32}Mg. In particular, in [Uts01, Fig. 3], MCSM calculations list approximate proportions of 0p0h, 2p2h, and 4p4h configurations for the ground states of ^{32}Mg and ^{30}Ne to be: ~5%-85%-10% and ~5%-70%-25%, respectively. The ratios of

occupancies of orbital $f_{7/2}$ with respect to $p_{3/2}$ [Uts99] in ^{32}Mg and ^{30}Ne are 6:1 and 3:1, respectively. This means that ^{30}Ne has a larger fraction of neutrons promoted to the higher-energy $p_{3/2}$ state, consistent with the fact that ^{30}Ne has a greater component of intruder configurations (larger percentage of 4p4h configuration) than ^{32}Mg.

The proton overlap for the ^{32}Mg-^{30}Ne pair is expected to be well described by USD wave functions (neutrons are spectators) and consequently the reduced cross section compared with the 2p2h theory is likely due to differences in neutron configurations. A simple estimate, assuming that ^{32}Mg is ~100% 2p2h, suggests that ^{30}Ne would have ~50% 2p2h, ~50% 4p4h intruder content.

6.3 ^{29}Ne

The spin/parity of the ^{29}Ne ground state has been tentatively assigned to be $3/2^+$ [ENS07], and its intruder configuration predicted to be ~100% 2p2h by SDPF-M [Uts07]. Only one γ ray in ^{29}Ne has been reported in the literature, at an energy of 680(80) keV [Bel05].

Recent experimental data on the N = 19 ^{31}Mg isotope provide some evidence for a large intruder configuration in the ground-state of N = 19 isotones. In particular, the magnetic dipole moment of the ^{31}Mg ground state was measured [Ney05] and shown to be consistent with predictions of an sdpf shell-model code which assigns a ~100% 2p2h intruder configuration to the ground state of ^{31}Mg.

Experimental data on the energy levels in N = 19 ^{29}Ne will provide additional information on the extent of intruder configuration at N = 19.

6.3.1 ^{29}Ne Spectrum of Excited States and γ-Ray Decays

Figure 6.12 shows the experimental decay scheme of ^{29}Ne along with SDPF-M and USD-A shell-model predictions. The three experimental γ-ray transitions are those at 622(4), 931(8) and 232(6) keV. SDPF-M calculations [Uts07] assign a ~100% 2p2h ground state to ^{29}Ne, and it can be considered to be a neutron (K = 1/2) hole in a deformed ^{30}Ne core according to the Nilsson model.

The existence of these low-lying excited states is not compatible with the USD-A calculations, which predict the first excited state to be located at a high energy of 1700 keV. The low-lying transitions can be instead explained within the framework of the SDPF-M calculations which involve 2p2h and 1p1h excitations, and assume a reduced N = 20 shell gap.

Comparing the measured 622-keV γ-ray transition with SDPF-M predictions, we postulate it to connect the $7/2^+$ level (predicted at 850 keV) to the $3/2^+_{(g.s.)}$. The 622-keV γ-ray transition could also correspond to the decay from $1/2^+$ to $3/2^+_{(g.s.)}$, where the $1/2^+$ level is predicted by the SDPF-M calculation to be located at 540 keV. Both the $7/2^+$ and the $1/2^+$ levels are part of the theoretically-predicted 2p2h intruder "K=1/2" band, where the $3/2^+$ becomes the ground state because of mixing with other $3/2^+$ spherical states not represented in Fig. 6.12.

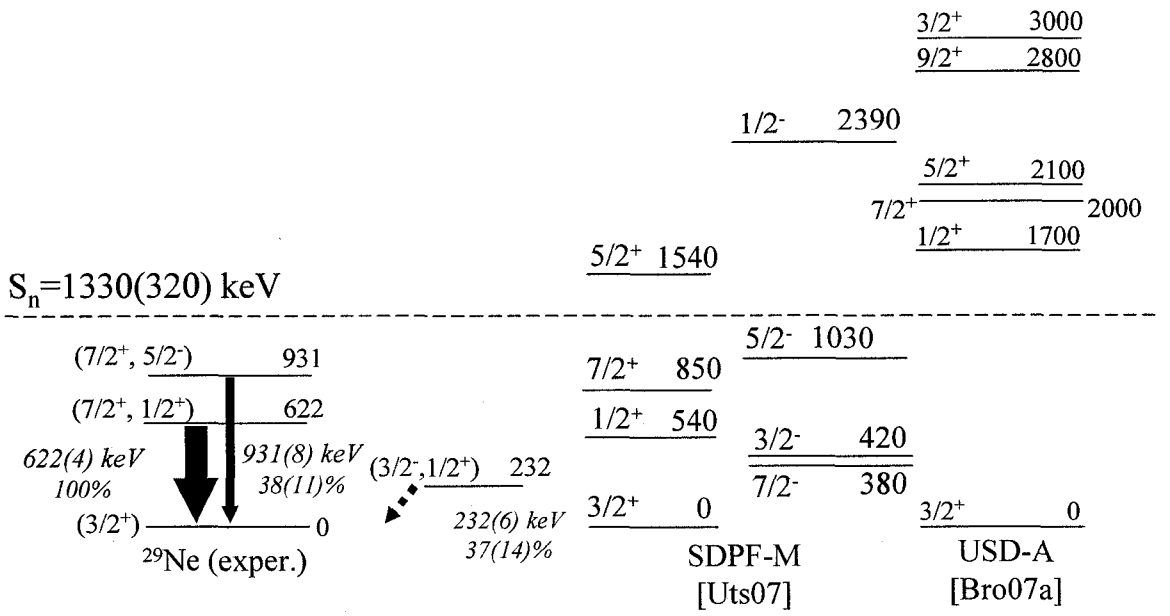

Figure 6.12 Comparison of the experimental level scheme of ^{29}Ne with level schemes predicted by MCSM shell-model calculations using the SDPF-M interaction [Uts07] and OXBASH using the USD-A interaction [Bro07a]. Each level is labeled with its energy in keV (on the right) and its spin/parity assignment (on the left). The spin/parity value is in parenthesis when tentative. Each γ-ray transition is labeled with its energy in keV and its transition intensity (%). The thickness of the arrows is roughly proportional to the corresponding γ-ray transition intensity. The figure includes also the location of the neutron separation energy given by [ENS07].

The next γ-ray transition in order of decreasing intensity is that at 931(8) keV, with a relative intensity of 38(11)%. By comparison with energy levels given by SDPF-M we postulate this transition to connect either the $7/2^+$ or the $5/2^-$ to the ground state.

Even though we don't have γ-γ coincidence data, we can rule out placing the 622- and the 931-keV transitions in the same decay cascade because the total excitation energy would be above the tabulated neutron separation energy, S_n = 1330(320) keV [ENS07].

The transition at 232(6) keV, with a relative intensity of 37(14)%, is a candidate for the decay of the negative-parity 1p1h $3/2^-$ level (predicted by SDPF-M at 420 keV) to the $3/2^+$ ground state. It is interesting to note that the experimental energies are lower than the SDPF-M shell-model predictions, particularly if the decays correspond to the positive-parity 2p2h states. Moreover, all the experimental energies fall far below USD predictions, where the first excited state with positive parity ($1/2^+$) lies at an energy of ~1700 keV (negative parity states would lie at 1 MeV and higher).

In summary, the observed ^{29}Ne spectrum displays the expected characteristics of a strongly deformed 2p2h intruder configuration and is consistent with a reduced N = 20 gap.

Chapter 7

Summary and Conclusions

This thesis addressed the structure of neutron-rich $^{28-30}$Ne nuclei located at the transition and in the "island of inversion." The island of inversion is a region of light neutron-rich nuclei centered around Z ~ 11 and N ~ 20 and characterized by strongly deformed ground states despite their nucleon number being close to the N = 20 "conventional" magic number.

The $^{28-30}$Ne nuclei were produced by few-nucleon knockout of ~80-105 MeV/A $^{30-32}$Mg and ^{29}Na beams following fragmentation of 140 MeV/A ^{48}Ca at the National Superconducting Cyclotron Laboratory, Michigan State University. Few-nucleon knockout is a direct reaction which – combined with γ-ray spectroscopy – provided information on the $^{28-30}$Ne structures. The low-lying $^{28-30}$Ne structures were determined through measurements of prompt single-γ and γ-γ coincidences using the Segmented Germanium Array (SeGA), where high transverse segmentation provided the Doppler correction necessary to achieve good energy resolution.

The $^{28-30}$Ne level schemes were compared with two types of shell-model calculations: (a) OXBASH using the USD-A interaction, with an sd-shell model space and restricted to 0p0h (0-particle-0-hole) "normal" configurations, and (b) a Monte Carlo Shell Model (MCSM) code using the SDPF-M interaction, which included the promotion of pairs of neutrons (mainly 2p2h "intruder" configurations) across a reduced N = 20

shell gap. A dominance of intruder configurations is believed to explain ground-state deformation. New data on $^{28-30}$Ne excited states were used to study the transition to the island of inversion and to test the validity of shell-model calculations.

^{28}Ne was produced by one- and two-proton knockout of 94 MeV/A ^{29}Na and 104 MeV/A ^{30}Mg with cross sections of 14(7) and 0.8(2) mb, respectively. The spectrum of excited states observed in ^{28}Ne was similar for both reactions. The ^{28}Ne structure consisted of a cascade of three consecutive transitions leading to the ground state. In the ^{29}Na to ^{28}Ne reaction, the measured $4_1^+ \rightarrow 2_1^+$ 1707(7)-keV and $2_1^+ \rightarrow 0_1^+$ 1306(4)-keV γ-ray transitions confirmed literature data [Bel00, Aza02a, Aza02b, Gui02, Bel05, Dom06a, Dom06b]. The γ-γ coincidence relationships for the observed 891(5)-keV γ ray (proposed to correspond to the $4_2^+ \rightarrow 4_1^+$ transition) ruled out recently published data [Bel05] assigning this transition to the $0_2^+ \rightarrow 2_1^+$. The MCSM model using the SDPF-M interaction predicts a ~50-50% 0p0h-2p2h ground-state configuration, suggesting that ^{28}Ne is a mixed normal-intruder nucleus located at the boundary of the island of inversion. Our experimental data showed better agreement with SDPF-M compared to USD-A, and thus supports a mixed normal-intruder ground state. However discrepancies exist; for example, the low-lying 2.2-MeV 0_2^+ state predicted by SDPF-M remains unobserved, and ^{28}Ne contains a new isolated 1127(4)-keV transition not explained by SDPF-M.

The $^{29-30}$Ne structures, with ~100% 2p2h ground-state configurations predicted by SDPF-M, showed significantly better fits to MCSM calculations using the SDPF-M interaction than the OXBASH code using the USD-A interaction.

^{30}Ne was produced in three measurements of two-proton knockout from ^{32}Mg (at ~80-90 MeV/A), with an average inclusive cross section of 0.22(3) mb. In the combined γ-ray spectrum of ^{30}Ne, a $2_1^+ \rightarrow 0_1^+$ 792(4)-keV transition confirmed literature data [Yan03, Yan04]. A new $4_1^+ \rightarrow 2_1^+$ 1443(11)-keV transition provided the first evidence for a 4_1^+ state in the island of inversion.

^{29}Ne was produced by few-nucleon knockout from ~80-90 MeV/A ^{32}Mg secondary beams with an average inclusive cross section of 0.25(3) mb. The strongest γ-ray transition at 622(4) keV feeding the ground state is a more accurate measurement of a recently reported transition at 680(80) keV [Bel05]. This transition and two new low-lying transitions at 931(8) keV and 232(6) keV are in better agreement with SDPF-M than USD-A, confirming that N = 19 ^{29}Ne is in the island of inversion.

Regarding reaction cross sections, our few-nucleon knockout cross section measurements between 0.2 and 14 mb agree with others reported in the literature. These data show measured one-proton knockout cross-sections to be ~0.5-0.7 of the magnitude of theoretical predictions. Our observed ~0.25 experimental-to-theoretical cross-section ratio in two-proton knockout was lower than the ~0.5 reported in the literature. This additional reduction factor for two-proton knockout suggests differences in the neutron configurations in the initial and final nuclei greater than those included in the reaction model.

Overall, there is good evidence that the structure data tend to be in better agreement with the MCSM calculations using a larger model space and using the SDPF-M interaction allowing pair scattering from the sd to the pf shell, favored by a reduced N = 20 shell gap caused by a strong proton-neutron interaction. However, the experimental

data provide evidence for a number of discrepancies relative to the SDPF-M predictions, especially in the case of ^{28}Ne, which have not been completely solved.

Future experimental research would benefit from the availability of more intense and energetic radioactive beams, which would contribute to significantly improved statistics in the γ-singles and γ-γ coincidence data. More and better γ-ray data, also allowed by larger and more highly-segmented and electronically-segmented germanium detector arrays such as GRETA [Lee03], would help discriminate between existing peaks and observe new transitions. Other experiments such as Coulomb excitation and inelastic scattering will be helpful as they provide data on transition strengths which are valuable in assessing the collectivity of nuclei, and can also serve to test predictions by shell-model calculations.

From the theoretical viewpoint, the reaction models need to be improved to quantitatively explore the differences between theoretical and observed inclusive cross sections. Specifically, in the Monte Carlo Shell Model calculations, there is a need to obtain nucleon overlap functions ("spectroscopic" factors) using fully mixed 0p0h, 2p2h and 4p4h wave functions that will constitute a more realistic input to the one- and two-proton knockout reaction codes.

Appendix A

Efficiency Calibrations of the Segmented Germanium Array

As explained in Chapter 4 (Section 4.2.4), the absolute efficiency of an array is the ratio of the number of full-energy γ rays detected vs. the number of γ rays emitted by the source. The absolute efficiency is a function of the energy of the γ ray. To determine the absolute efficiency of SeGA we used a ^{152}Eu source (labeled Z2707 at MSU) with a reported activity of 3.131×10^5 ($\pm$1.4%) Bq on May 1st 1978. The half-life of ^{152}Eu is $t_{1/2}$ (^{152}Eu) = 13.537(6) years [Fir96].

The first step in obtaining an absolute efficiency curve was to obtain a relative efficiency curve. The relative efficiency curve is a fit to a number of data points, each of which is the measured "intensity" of a γ-ray peak in the γ-ray spectrum produced by the ^{152}Eu source during a ~one-hour time interval. Each measured "intensity" is the ratio of a given background-subtracted peak area to its corresponding branching ratio (the branching ratios are listed in Table 4.1).

A. 1 Absolute Efficiency Curves in E03053

In the E03053 experiment (conducted in 2004), the relative efficiency was fitted to the following expression:

$$\log_{10}(\varepsilon_{rel,2004}) = 14.07 - 5.851\log_{10}(E) + 0.8846\log_{10}^{2}(E) - \frac{10050}{E^2} \quad (A.1)$$

where E is in keV.

To obtain the absolute efficiency, we used the known value of the activity of the ^{152}Eu source (with MSU label Z2707) which was used for the efficiency calibration. The reported activity of this source on May 1st 1978, neglecting its small uncertainty, is:

$$A_o(^{152}\text{Eu source, May 1}^{st}\text{ 1978}) = 3.131\text{x}10^5\text{ Bq} \quad (A.2)$$

The calibration run was performed on Dec. 13th 2004, so that its activity after the elapsed time of 26.622 years, and using the $t_{1/2}(^{152}\text{Eu}) = 13.537$ years, was calculated as:

$$A\ (t = 26.622\text{ yr}) = A_o \exp(-t*0.693/t_{1/2}) = 8.0131\text{x}10^4\text{ Bq} \quad (A.3)$$

To calculate the absolute efficiency we used one of the ^{152}Eu peaks, in particular we chose the 1.085-MeV peak with branching ratio of 10.13% (Table 4.1). The activity corresponding to this peak was calculated as:

$$A(1.085\text{-MeV peak}) = (0.1013)*(8.0131\text{x}10^4\text{ Bq}) = 8117.27\text{ Bq} \quad (A.4)$$

The area under the 1.085 MeV peak, accumulated during the calibration run was 199687.5. The calibration run lasted 3720 seconds, with a live time of 23.0897%, so that the actual time was 858.94 seconds. Using this area and the actual time we calculated the activity (of 1.085 MeV peak) as 232.48 Bq. Since the total activity of this peak was 8117.27 Bq, the absolute efficiency of the 17-detector array in E03053 was calculated as 2.864% at 1.085 MeV. This value was used to convert the relative efficiency curve (Eq. A.1) into an absolute efficiency calibration curve as follows:

$$\varepsilon_{abs,2004} = \frac{1}{987639.67} 10^{\left[14.07 - 5.851\log_{10}(E) + 0.8846\log_{10}^{2}(E) - \frac{10050}{E^2}\right]} \quad (A.5)$$

where E is in keV, and $\varepsilon_{abs,\,2004}$ denotes the absolute efficiency of the 17-detector SeGA array used in E03053 and evaluated with a stationary ^{152}Eu calibration source located at the center of SeGA.

Due to the high velocity of the secondary fragments, the γ rays that they emit are affected by the Lorentz-boost and the Doppler-shift corrections (Section 4.2.4). These two corrections are angle-dependent and they affect differently the efficiency of the 37°- and the 90°-rings, so it was necessary to have separate absolute efficiency curves for the 37°- and the 90° rings. By comparing the areas of the ^{152}Eu peaks measured by the 37° and the 90° rings, we observed that the 90° peaks were, on average and consistently, a factor of 1.2125 that of the 37° peaks. Therefore we deduced the contributions of the 37° and 90° rings to the efficiency curve to be 45.2% and 54.8%, respectively. Assuming that the shape of the efficiency curves in the individual rings is the same as that of the total efficiency, we can write:

$$\varepsilon_{abs\_37,2004} = \frac{0.452}{987639.67} 10^{\left[14.07 - 5.851\log_{10}(E) + 0.8846\log_{10}^{2}(E) - \frac{10050}{E^2}\right]} \qquad (A.6)$$

$$\varepsilon_{abs\_90,2004} = \frac{0.548}{987639.67} 10^{\left[14.07 - 5.851\log_{10}(E) + 0.8846\log_{10}^{2}(E) - \frac{10050}{E^2}\right]} \qquad (A.7)$$

where the absolute efficiency of the array is the sum of the corresponding 37°- and 90°-ring contributions:

$$\varepsilon_{abs,\,2004} = \varepsilon_{abs\_37,\,2004} + \varepsilon_{abs\_90,\,2004} \qquad (A.8)$$

Expressions (A.6) and (A.7) are the formulas for the solid lines connecting the experimental efficiency points in Figs. 4.9 and 4.10, respectively.

The Lorentz-boosted efficiency curves in Figs. 4.9 and 4.10 (dashed lines) were obtained from the absolute efficiency curves by multiplying them by their corresponding Lorentz-boost factor:

$$\varepsilon_{37,\,2004} = f_{37}\,\varepsilon_{abs\_37,\,2004} \tag{A.9}$$

$$\varepsilon_{90,\,2004} = f_{90}\,\varepsilon_{abs\_90,\,2004} \tag{A.10}$$

where the Lorentz-boost factors f_{37} and f_{90} can be calculated using Eq. 4.2 in Chapter 4.

A.2 Absolute Efficiency Curves in E05122

The same procedure described in A.1 was applied to obtain the absolute efficiency curves in the E05122 experiment (conducted in 2006). In E05122, the relative efficiency was fitted to the following expression:

$$\log_{10}(\varepsilon_{rel,\,2006}) = 8.623 - 2.93\log_{10}(E) + 0.384\log_{10}^{2}(E) - \frac{10200}{E^{2}} \tag{A.11}$$

where E is in keV.

We used the same ^{152}Eu calibration source as in E03053, with original activity A_o as expressed in Eq. A.2. The calibration run was performed on Sept. 2nd, 2006, so that its activity after the elapsed time of 28.34 years was calculated as:

$$A(t = 28.34\ yr) = A_o \exp(-t*0.693/t_{1/2}) = 7.3384\text{x}10^{4}\ Bq \tag{A.12}$$

To calculate the absolute efficiency we used again the 1.085-MeV peak with branching ratio 10.13% (Table 4.1). The activity corresponding to this peak was calculated as:

$$A(1.085\text{-MeV peak}) = (0.1013)*(7.3384\text{x}10^{4}\ Bq) = 7433.85\ Bq \tag{A.13}$$

The area under the 1.085 MeV peak, accumulated during the calibration run was 13016. The calibration run lasted 282 seconds, with a live time of 24.6%, so the actual time was 69.372 seconds. Using this area and the actual time we calculated the activity (of the 1.085-MeV peak) as 187.6 Bq. Since the total activity of this peak is 7433.85 Bq, the absolute efficiency of the 16-detector array in E05122 was obtained as 2.52% at 1.085 MeV. This value was used to convert the relative efficiency curve (Eq. A.11) into an absolute efficiency calibration curve as follows:

$$\varepsilon_{abs,2006} = \frac{1}{71947.5} 10^{\left[8.623 - 2.93\log_{10}(E) + 0.384\log_{10}^{2}(E) - \frac{10200}{E^{2}}\right]} \qquad (A.14)$$

where E is in keV, and $\varepsilon_{abs,2006}$ denotes the absolute efficiency of the 16-detector SeGA array used in E05122 and evaluated with a stationary ^{152}Eu calibration source located at the center of SeGA.

To allow for the application of Lorentz-boost and Doppler-shift corrections (Section 4.2.4) it was necessary to obtain separate absolute efficiency curves for the 37°- and the 90°-rings. By comparing the areas of the ^{152}Eu peaks measured by the 37° and the 90° rings, we observed that the 90° peaks were, on average and consistently, a factor of 1.219 that of the 37° peaks. Therefore we can deduce the contributions of the 37° and 90° rings to the efficiency curve to be 45.1% and 54.9%, respectively. Assuming again that the shape of the efficiency curves in the individual rings is the same as the total intrinsic efficiency, we can write:

$$\varepsilon_{abs\_37,2006} = \frac{0.451}{71947.5} 10^{\left[8.623 - 2.93\log_{10}(E) + 0.384\log_{10}^{2}(E) - \frac{10200}{E^{2}}\right]} \qquad (A.15)$$

$$\varepsilon_{abs\_90,2006} = \frac{0.549}{71947.5} 10^{\left[8.623 - 2.93\log_{10}(E) + 0.384\log_{10}^{2}(E) - \frac{10200}{E^2}\right]} \quad \text{(A.16)}$$

where the absolute efficiency of the array is the sum of the corresponding 37°- and 90°-ring contributions:

$$\varepsilon_{abs,2006} = \varepsilon_{abs\_37,2006} + \varepsilon_{abs\_90,2006} \quad \text{(A.17)}$$

Expressions (A.15) and (A.16) are the formulas for the solid lines connecting the experimental efficiency points in Figs. 4.11 and 4.12, respectively.

The Lorentz-boosted efficiency curves in Figs. 4.11 and 4.12 (dashed lines) are obtained from the absolute efficiency curves by multiplying them by their corresponding factor:

$$\varepsilon_{37,2006} = f_{37}\,\varepsilon_{abs\_37,2006} \quad \text{(A.18)}$$

$$\varepsilon_{90,2006} = f_{90}\,\varepsilon_{abs\_90,2006} \quad \text{(A.19)}$$

Appendix B

Analysis of Cross Section Data and Calculation of Errors

B.1 Inclusive Cross Sections

The inclusive cross section σ_{inc} was defined in Chapter 4 (Eq. 4.5) to be:

$$\sigma_{inc} = \frac{N_f \text{ (particles)}}{N_b \text{ (particles) } N_t \text{ (particles/cm}^2)} * 10^{27} \text{ mb/cm}^2 \quad \text{(B.1)}$$

The numbers of fragment (N_f), beam (N_b) and target (N_t) particles were defined in Chapter 4 as follows (Eqs. B.2 to B.4):

$$N_f = \frac{N_{kn}}{lt_{kn}\ eff_{kn}\ eff_{gat} K_{CRDC}} \quad \text{(B.2)}$$

$$N_b = \frac{N_{unr}}{lt_{unr}\ eff_{unr}} \frac{scaler_{kn}}{scaler_{unr}} \quad \text{(B.3)}$$

$$N_t \text{ (particles/cm}^2) = \frac{\rho_t \text{(g/cm}^2) N_A \text{(particles/mol)}}{AW_t \text{ (g/mol)}} \quad \text{(B.4)}$$

where N_{kn} and N_{unr} are numbers of particles detected in the PID spectrum for a given fragment type in the knockout run (N_{kn}) and for a given beam type during the unreacted run (N_{unr}); lt_{kn} and lt_{unr} are lifetimes of the knockout and unreacted runs, respectively; eff_{kn}, eff_{unr} and eff_{gat} are efficiencies in the knockout and unreacted runs, and due to gating in the knockout run (explained in Chapter 4); K_{CRDC} is the fraction (between 0 and 1) of fragments that were detected within the S800 focal plane acceptance; $scaler_{kn}$ and $scaler_{unr}$ are numbers of counts registered at the S800 object scintillator; ρ_t is the density

of the target, N_A is Avogadro's number = 6.023×10^{23}, and AW_t is the atomic weight of the target in units of g/mol.

The uncertainty in the inclusive cross section σ_{inc} was expressed as:

$$\frac{\Delta\sigma_{inc}}{\sigma_{inc}} = \sqrt{\left(\frac{\Delta N_f}{N_f}\right)^2 + \left(\frac{\Delta N_b}{N_b}\right)^2 + \left(\frac{\Delta N_t}{N_t}\right)^2} \tag{B.5}$$

The following are expressions for the uncertainties in N_f, N_b, and N_t:

$$\frac{\Delta N_f}{N_f} = \sqrt{\left(\frac{\Delta N_{kn}}{N_{kn}}\right)^2 + \left(\frac{\Delta eff_{kn}}{eff_{kn}}\right)^2 + \left(\frac{\Delta eff_{gat}}{eff_{gat}}\right)^2 + \left(\frac{\Delta K_{CRDC}}{K_{CRDC}}\right)^2} \tag{B.6}$$

$$\frac{\Delta N_b}{N_b} = \sqrt{\left(\frac{\Delta N_{unr}}{N_{unr}}\right)^2 + \left(\frac{\Delta eff_{unr}}{eff_{unr}}\right)^2} \tag{B.7}$$

$$\frac{\Delta N_t}{N_t} = \frac{\Delta \rho_t}{\rho_t} \tag{B.8}$$

Tables B.1 through B.10 contain detailed calculations of inclusive cross sections in experiments E03053 and E05122, including error estimates. Figure B.1 contains the CRDC spectrum of ^{28}Ne produced by two-proton knockout of ^{30}Mg measured at the S800 focal plane, for which the estimated K_{CRDC} was ~0.70.

Table B.1 **Cross sections of fragments produced by the ^{29}Na secondary beam in E03053.** The calculations use the following constant values: N_{unr} = 11676, $\Delta N_{unr}/N_{unr}$ = 0.05, $scaler_{unr}$ = 1.25x10^5, lt_{unr} = 0.737, eff_{unr} = 0.88, $\Delta eff_{unr}/eff_{unr}$ = 0.071, $scaler_{kn}$ = 6.63x10^9, $\Delta N_{kn}/N_{kn}$ = 0.05, lt_{kn} = 0.996, eff_{kn} = 0.79, $\Delta eff_{kn}/eff_{kn}$ = 0.071, eff_{gat} = 1, $\Delta eff_{gat}/eff_{gat}$ = 0, $\Delta N_t/N_t$ = 0.01.

Reaction	N_b	$\Delta N_b/N_b$	N_{kn}	K_{CRDC}	$\Delta K_{CRDC}/K_{CRDC}$	N_f	$\Delta N_f/N_f$	N_t	σ(mb)	Δσ/σ	Δσ(mb)
29Na → 28Ne	9.57E+08	0.087	59112	0.15	0.47	500951	0.48	3.78E+22	14	0.5	7
29Na → 25F	9.57E+08	0.087	13785	0.60	0.17	29206	0.19	3.78E+22	0.8	0.2	0.2
29Na → 26F	9.57E+08	0.087	9974	0.70	0.14	18113	0.17	3.78E+22	0.5	0.2	0.1
29Na → 27F	9.57E+08	0.087	4458	0.60	0.17	9445	0.19	3.78E+22	0.3	0.2	0.1
29Na → 22O	9.57E+08	0.087	6924	0.60	0.17	14670	0.19	3.78E+22	0.4	0.2	0.1
29Na → 19N	9.57E+08	0.087	7535	0.60	0.17	15964	0.19	3.78E+22	0.4	0.2	0.1
29Na → 20N	9.57E+08	0.087	7507	0.60	0.17	15905	0.19	3.78E+22	0.4	0.2	0.1
29Na → 16C	9.57E+08	0.087	6096	0.60	0.17	12915	0.19	3.78E+22	0.4	0.2	0.1

Table B.2 **Cross sections of fragments produced by the ^{30}Mg secondary beam in E03053.** The calculations use the following constant values: N_{unr} = 23112, $\Delta N_{unr}/N_{unr}$ = 0.05, $scaler_{unr}$ = 1.25x10^5, lt_{unr} = 0.737, eff_{unr} = 0.88, $\Delta eff_{unr}/eff_{unr}$ = 0.071, $scaler_{kn}$ = 6.63x10^9, $\Delta N_{kn}/N_{kn}$ = 0.05, lt_{kn} = 0.996, eff_{kn} = 0.79, $\Delta eff_{kn}/eff_{kn}$ = 0.071, eff_{gat} = 0.442, $\Delta eff_{gat}/eff_{gat}$ = 0.071, $\Delta N_t/N_t$ = 0.01.

Reaction	N_b	$\Delta N_b/N_b$	N_{kn}	K_{CRDC}	$\Delta K_{CRDC}/K_{CRDC}$	N_f	$\Delta N_f/N_f$	N_t	σ(mb)	Δσ/σ	Δσ(mb)
30Mg → 29Na	1.89E+09	0.087	38893	0.60	0.17	186427	0.20	3.78E+22	2.6	0.2	0.6
30Mg → 30Na	1.89E+09	0.087	12412	0.60	0.17	59495	0.20	3.78E+22	0.8	0.2	0.2
30Mg → 26Ne	1.89E+09	0.087	4215	0.60	0.17	20204	0.20	3.78E+22	0.28	0.22	0.06
30Mg → 27Ne	1.89E+09	0.087	10752	0.60	0.17	51538	0.20	3.78E+22	0.7	0.2	0.2
30Mg → 28Ne	1.89E+09	0.087	14446	0.70	0.14	59352	0.18	3.78E+22	0.8	0.2	0.2
30Mg → 24F	1.89E+09	0.087	9617	0.60	0.17	46097	0.20	3.78E+22	0.6	0.2	0.1
30Mg → 25F	1.89E+09	0.087	6059	0.80	0.13	21782	0.17	3.78E+22	0.30	0.20	0.06

Table B.3 **Cross sections of fragments produced by the ^{32}Al secondary beam in E03053.** The calculations use the following constant values: N_{unr} = 7612, $\Delta N_{unr}/N_{unr}$ = 0.05, $scaler_{unr}$ = 1.25x10^5, lt_{unr} = 0.737, eff_{unr} = 0.88, $\Delta eff_{unr}/eff_{unr}$ = 0.071, $scaler_{kn}$ = 6.63x10^9, $\Delta N_{kn}/N_{kn}$ = 0.05, lt_{kn} = 0.996, eff_{kn} = 0.79, $\Delta eff_{kn}/eff_{kn}$ = 0.071, eff_{gat} = 0.442, $\Delta eff_{gat}/eff_{gat}$ = 0.071, $\Delta N_t/N_t$ = 0.01.

Reaction	N_b	$\Delta N_b/N_b$	N_{kn}	K_{CRDC}	$\Delta K_{CRDC}/K_{CRDC}$	N_f	$\Delta N_f/N_f$	N_t	σ(mb)	Δσ/σ	Δσ(mb)
32Al → 29Na	6.24E+08	0.087	6601	0.60	0.17	31641	0.20	3.78E+22	1.3	0.2	0.3
32Al → 30Na	6.24E+08	0.087	7128	0.60	0.17	34167	0.20	3.78E+22	1.4	0.2	0.3
32Al → 26Ne	6.24E+08	0.087	1462	0.60	0.17	7008	0.20	3.78E+22	0.30	0.22	0.07
32Al → 27Ne	6.24E+08	0.087	1308	0.60	0.17	6270	0.20	3.78E+22	0.27	0.22	0.06
32Al → 28Ne	6.24E+08	0.087	1524	0.60	0.17	7305	0.20	3.78E+22	0.31	0.22	0.07
32Al → 24F	6.24E+08	0.087	2151	0.60	0.17	10310	0.20	3.78E+22	0.4	0.2	0.1
32Al → 25F	6.24E+08	0.087	1055	0.70	0.14	4335	0.18	3.78E+22	0.18	0.21	0.04

Table B.4 **Cross sections of fragments produced by the ^{32}Mg secondary beam in E03053.** The calculations use the following constant values: N_{unr} = 11473, $\Delta N_{unr}/N_{unr}$ = 0.05, $scaler_{unr}$ = 2.26x10^5, lt_{unr} = 0.663, eff_{unr} = 0.9144, $\Delta eff_{unr}/eff_{unr}$ = 0.071, $scaler_{kn}$ = 3.07x10^9, $\Delta N_{kn}/N_{kn}$ = 0.05, lt_{kn} = 0.999, eff_{kn} = 0.82, $\Delta eff_{kn}/eff_{kn}$ = 0.071, eff_{gat} = 1, $\Delta eff_{gat}/eff_{gat}$ = 0, $\Delta N_t/N_t$ = 0.01.

Reaction	N_b	$\Delta N_b/N_b$	N_{kn}	K_{CRDC}	$\Delta K_{CRDC}/K_{CRDC}$	N_f	$\Delta N_f/N_f$	N_t	σ(mb)	Δσ/σ	Δσ(mb)
32Mg → 31Na	2.56E+08	0.087	1882	0.20	0.50	11492	0.51	3.78E+22	1.2	0.5	0.6
32Mg → 28Ne	2.56E+08	0.087	794	0.20	0.50	4848	0.51	3.78E+22	0.5	0.5	0.3
32Mg → 29Ne	2.56E+08	0.087	1238	0.60	0.17	2520	0.19	3.78E+22	0.26	0.21	0.06
32Mg → 30Ne	2.56E+08	0.087	1526	0.78	0.13	2389	0.15	3.78E+22	0.25	0.18	0.05
32Mg → 25F	2.56E+08	0.087	590	0.20	0.50	3603	0.51	3.78E+22	0.4	0.5	0.2
32Mg → 26F	2.56E+08	0.087	706	0.30	0.33	2874	0.34	3.78E+22	0.3	0.4	0.1
32Mg → 27F	2.56E+08	0.087	521	0.60	0.17	1060	0.19	3.78E+22	0.11	0.21	0.02

Table B.5 **Cross sections of fragments produced by the ^{33}Al secondary beam in E03053.** The calculations use the following constant values: N_{unr} = 43125, $\Delta N_{unr}/N_{unr}$ = 0.05, $scaler_{unr}$ = 2.26x10^5, lt_{unr} = 0.663, eff_{unr} = 0.9144, $\Delta eff_{unr}/eff_{unr}$ = 0.071, $scaler_{kn}$ = 3.07x10^9, $\Delta N_{kn}/N_{kn}$ = 0.05, lt_{kn} = 0.999, eff_{kn} = 0.82, $\Delta eff_{kn}/eff_{kn}$ = 0.071, eff_{gat} = 0.71, $\Delta eff_{gat}/eff_{gat}$ = 0.071, $\Delta N_t/N_t$ = 0.01.

Reaction	N_b	$\Delta N_b/N_b$	N_{kn}	K_{CRDC}	$\Delta K_{CRDC}/K_{CRDC}$	N_f	$\Delta N_f/N_f$	N_t	σ(mb)	Δσ/σ	Δσ(mb)
33Al → 32Mg	9.63E+08	0.087	1101	0.20	0.50	9469	0.51	3.78E+22	0.3	0.5	0.1
33Al → 33Mg	9.63E+08	0.087	341	0.20	0.50	2933	0.51	3.78E+22	0.08	0.52	0.04
33Al → 29Na	9.63E+08	0.087	491	0.20	0.50	4223	0.51	3.78E+22	0.12	0.52	0.06
33Al → 30Na	9.63E+08	0.087	4309	0.60	0.17	12353	0.20	3.78E+22	0.34	0.22	0.08
33Al → 31Na	9.63E+08	0.087	7792	0.80	0.13	16753	0.17	3.78E+22	0.46	0.20	0.09
33Al → 27Ne	9.63E+08	0.087	508	0.30	0.33	2913	0.35	3.78E+22	0.08	0.37	0.03
33Al → 28Ne	9.63E+08	0.087	2056	0.70	0.14	5052	0.18	3.78E+22	0.14	0.21	0.03
33Al → 24F	9.63E+08	0.087	973	0.60	0.17	2789	0.20	3.78E+22	0.08	0.22	0.02
33Al → 25F	9.63E+08	0.087	1276	0.50	0.20	4389	0.23	3.78E+22	0.12	0.25	0.03

Table B.6 **Cross sections of fragments produced by the ^{35}Si secondary beam in E03053.** The calculations use the following constant values: N_{unr} = 10737, $\Delta N_{unr}/N_{unr}$ = 0.05, $scaler_{unr}$ = 2.26x10^5, lt_{unr} = 0.663, eff_{unr} = 0.9144, $\Delta eff_{unr}/eff_{unr}$ = 0.071, $scaler_{kn}$ = 3.07x10^9, $\Delta N_{kn}/N_{kn}$ = 0.05, lt_{kn} = 0.999, eff_{kn} = 0.82, $\Delta eff_{kn}/eff_{kn}$ = 0.071, eff_{gat} = 0.71, $\Delta eff_{gat}/eff_{gat}$ = 0.071, $\Delta N_t/N_t$ = 0.01.

Reaction	N_b	$\Delta N_b/N_b$	N_{kn}	K_{CRDC}	$\Delta K_{CRDC}/K_{CRDC}$	N_f	$\Delta N_f/N_f$	N_t	σ(mb)	Δσ/σ	Δσ(mb)
35Si → 32Mg	2.40E+08	0.087	378	0.20	0.50	3251	0.51	3.78E+22	0.4	0.5	0.2
35Si → 33Mg	2.40E+08	0.087	251	0.20	0.50	2159	0.51	3.78E+22	0.2	0.5	0.1
35Si → 29Na	2.40E+08	0.087	115	0.20	0.50	989	0.51	3.78E+22	0.11	0.52	0.06
35Si → 30Na	2.40E+08	0.087	435	0.60	0.17	1247	0.20	3.78E+22	0.14	0.22	0.03
35Si → 31Na	2.40E+08	0.087	586	0.80	0.13	1260	0.17	3.78E+22	0.14	0.20	0.03
35Si → 27Ne	2.40E+08	0.087	82	0.30	0.33	470	0.35	3.78E+22	0.05	0.37	0.02
35Si → 28Ne	2.40E+08	0.087	194	0.70	0.14	477	0.18	3.78E+22	0.05	0.21	0.01
35Si → 24F	2.40E+08	0.087	208	0.60	0.17	596	0.20	3.78E+22	0.07	0.22	0.01
35Si → 25F	2.40E+08	0.087	143	0.50	0.20	492	0.23	3.78E+22	0.05	0.25	0.01

Table B.7 **Fragments produced by the ^{31}Mg secondary beam in E05122, where Bρ of the S800 is 3.6185 Tm.** The calculations use the following constant values: N_{unr} = 141019, $\Delta N_{unr}/N_{unr}$ = 0.05, $scaler_{unr}$ = 3.15x10^5, lt_{unr} = 0.547, eff_{unr} = 0.994, $\Delta eff_{unr}/eff_{unr}$ = 0.071, $scaler_{kn}$ = 2.67x10^9, $\Delta N_{kn}/N_{kn}$ = 0.05, lt_{kn} = 0.854, eff_{kn} = 0.576, $\Delta eff_{kn}/eff_{kn}$ = 0.071, eff_{gat} = 1, $\Delta eff_{gat}/eff_{gat}$ = 0, $\Delta N_t/N_t$ = 0.01.

Reaction	N_b	$\Delta N_b/N_b$	N_{kn}	K_{CRDC}	$\Delta K_{CRDC}/K_{CRDC}$	N_f	$\Delta N_f/N_f$	N_t	σ(mb)	Δσ/σ	Δσ(mb)
31Mg → 26Ne	2.20E+09	0.087	21619	0.30	0.33	146524	0.34	2.52E+22	2.6	0.4	0.9
31Mg → 27Ne	2.20E+09	0.087	34256	0.90	0.11	77391	0.14	2.52E+22	1.4	0.2	0.2
31Mg → 28Ne	2.20E+09	0.087	13832	0.80	0.13	35155	0.15	2.52E+22	0.6	0.2	0.1
31Mg → 30Na	2.20E+09	0.087	352965	0.90	0.11	797413	0.14	2.52E+22	14	0.2	2
31Mg → 31Na	2.20E+09	0.087	19257	0.80	0.13	48943	0.15	2.52E+22	0.9	0.2	0.2

Table B.8 **Fragments produced by the ^{32}Mg secondary beam in E05122, where Bρ of the S800 is 3.4957 Tm.** The calculations use the following constant values: N_{unr} = 122646, $\Delta N_{unr}/N_{unr}$ = 0.05, $scaler_{unr}$ = 3.07x10^5, lt_{unr} = 0.646, eff_{unr} = 0.994, $\Delta eff_{unr}/eff_{unr}$ = 0.071, $scaler_{kn}$ = 1.94x10^9, $\Delta N_{kn}/N_{kn}$ = 0.05, lt_{kn} = 0.896, eff_{kn} = 0.576, $\Delta eff_{kn}/eff_{kn}$ = 0.071, eff_{gat} = 1, $\Delta eff_{gat}/eff_{gat}$ = 0, $\Delta N_t/N_t$ = 0.01.

Reaction	N_b	$\Delta N_b/N_b$	N_{kn}	K_{CRDC}	$\Delta K_{CRDC}/K_{CRDC}$	N_f	$\Delta N_f/N_f$	N_t	σ(mb)	Δσ/σ	Δσ(mb)
32Mg → 27Ne	1.21E+09	0.087	8028	0.60	0.17	25927	0.19	2.52E+22	0.9	0.2	0.2
32Mg → 28Ne	1.21E+09	0.087	12182	0.80	0.13	29507	0.15	2.52E+22	1.0	0.2	0.2
32Mg → 30Na	1.21E+09	0.087	80302	0.90	0.11	172895	0.14	2.52E+22	6	0.2	1
32Mg → 31Na	1.21E+09	0.087	61821	0.90	0.11	133105	0.14	2.52E+22	4.4	0.2	0.8

Table B.9 **Fragments produced by the ^{32}Mg secondary beam in E05122, where Bρ of the S800 is 3.7201 Tm.** The calculations use the following constant values: N_{unr} = 122646, $\Delta N_{unr}/N_{unr}$ = 0.05, $scaler_{unr}$ = 3.07x10^5, lt_{unr} = 0.646, eff_{unr} = 0.994, $\Delta eff_{unr}/eff_{unr}$ = 0.071, $scaler_{kn}$ = 1.19x10^9, $\Delta N_{kn}/N_{kn}$ = 0.05, lt_{kn} = 0.970, eff_{kn} = 0.88, $\Delta eff_{kn}/eff_{kn}$ = 0.071, eff_{gat} = 1, $\Delta eff_{gat}/eff_{gat}$ = 0, $\Delta N_t/N_t$ = 0.01.

Reaction	N_b	$\Delta N_b/N_b$	N_{kn}	K_{CRDC}	$\Delta K_{CRDC}/K_{CRDC}$	N_f	$\Delta N_f/N_f$	N_t	σ(mb)	Δσ/σ	Δσ(mb)
32Mg → 28Ne	7.43E+08	0.087	10071	0.30	0.33	39326	0.34	2.52E+22	2.1	0.4	0.8
32Mg → 29Ne	7.43E+08	0.087	3949	0.92	0.11	5028	0.14	2.52E+22	0.27	0.17	0.05
32Mg → 30Ne	7.43E+08	0.087	1489	0.44	0.23	3964	0.24	2.52E+22	0.21	0.3	0.06
32Mg → 31Na	7.43E+08	0.087	67232	0.30	0.33	262529	0.34	2.52E+22	14	0.4	5
32Mg → 32Na	7.43E+08	0.087	5372	0.70	0.14	8990	0.17	2.52E+22	0.48	0.2	0.09

Table B.10 Fragments produced by the ^{32}Mg secondary beam in E05122, where Bρ of the S800 is 3.7201 Tm. The calculations use the following constant values: N_{unr} = 122646, $\Delta N_{unr}/N_{unr}$ = 0.05, $scaler_{unr}$ = 3.07x10^5, lt_{unr} = 0.646, eff_{unr} = 0.994, $\Delta eff_{unr}/eff_{unr}$ = 0.071, $scaler_{kn}$ = 1.1x10^9, $\Delta N_{kn}/N_{kn}$ = 0.05, lt_{kn} = 0.999, eff_{kn} = 0.85, $\Delta eff_{kn}/eff_{kn}$ = 0.071, eff_{gat} = 1, $\Delta eff_{gat}/eff_{gat}$ = 0, $\Delta N_t/N_t$ = 0.01.

Reaction	N_b	$\Delta N_b/N_b$	N_{kn}	K_{CRDC}	$\Delta K_{CRDC}/K_{CRDC}$	N_f	$\Delta N_f/N_f$	N_t	σ(mb)	Δσ/σ	Δσ(mb)
32Mg → 28Ne	6.82E+08	0.087	952	0.30	0.33	3740	0.34	2.52E+22	0.2	0.4	0.1
32Mg → 29Ne	6.82E+08	0.087	2022	0.65	0.15	3666	0.18	2.52E+22	0.21	0.20	0.04
32Mg → 30Ne	6.82E+08	0.087	2304	0.74	0.14	3669	0.16	2.52E+22	0.21	0.19	0.04
32Mg → 31Na	6.82E+08	0.087	1241	0.20	0.50	7313	0.51	2.52E+22	0.4	0.5	0.2
32Mg → 32Na	6.82E+08	0.087	933	0.30	0.33	3665	0.34	2.52E+22	0.2	0.4	0.1

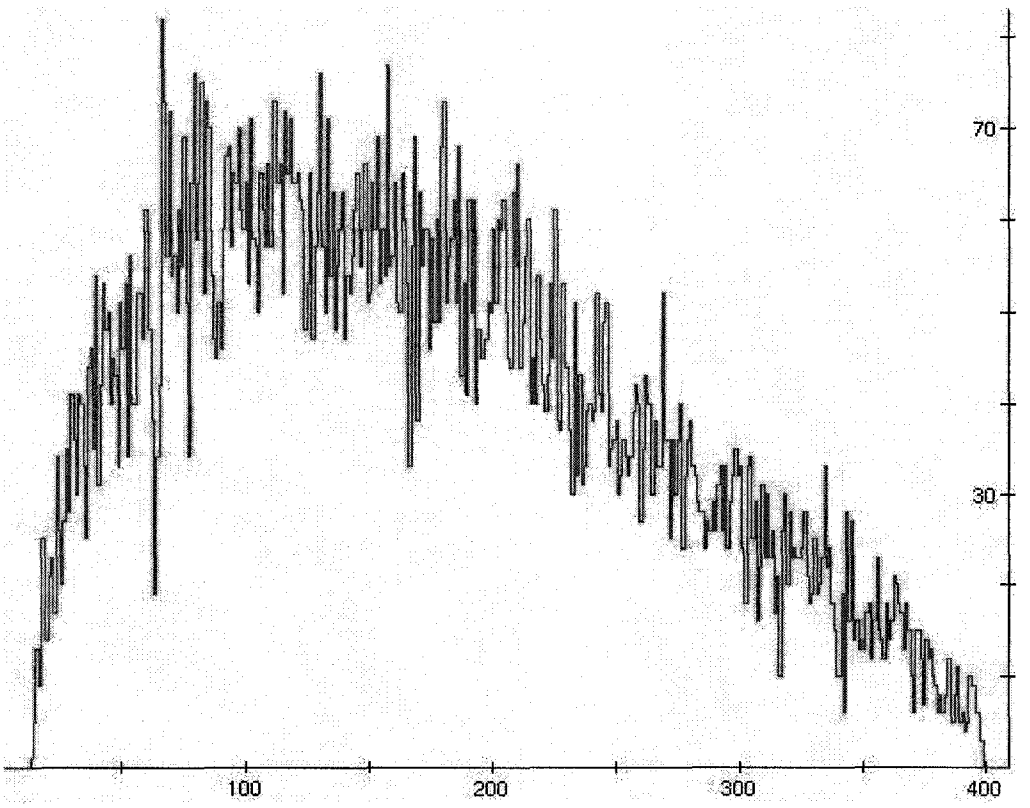

Figure B.1 Sample of a CRDC spectrum of ^{28}Ne produced by two-proton knockout of ^{30}Mg, measured at the S800 focal plane.

Appendix C

Analysis of γ-Ray Intensity Data and Calculation of Errors

This appendix details the procedure to obtain the γ-ray intensities, I_γ, where the γ-ray intensity of the transition from the first excited state to the ground state is defined as 100%. The procedure involves first the measurement of peak intensities, I_p, in a given γ-ray spectrum. The peak intensity is defined as the ratio of the area of a background-subtracted peak, A_p, vs. the Lorentz-boosted absolute efficiency ε, i.e., $I_p = A_p/\varepsilon$.

The energy of a given peak in the γ-ray spectrum given by the data acquisition software SpecTcl [Spe07] is a "Doppler-corrected" (or "Doppler-reconstructed") energy, E_γ^0, which is converted to a Doppler-shifted energy, $E_\gamma(\theta)$, where θ is 37° or 90°, by multiplying E_γ^0 by the corresponding $E_\gamma(\theta)/E_\gamma^0$ factor, which depends on β (= v/c of the fragment) and θ (the θ values for the SeGA rings are either 37° or 90°) as indicated in Eq. C.1 and represented in Table C.1 and Fig. C.1:

$$E_\gamma(\theta) = \frac{E_\gamma^0 (1-\beta^2)^{1/2}}{1-\beta\cos\theta} \qquad \text{(C.1)}$$

Table C.1 gives values of $E_\gamma(\theta)/E_\gamma^0$ for a range of β and θ values. Tables C.2 to C.5 contain detailed calculations of the γ-ray intensities of transitions in $^{28\text{-}30}$Ne produced in different few-nucleon knockout reactions.

Table C.1 Values of $E_\gamma(\theta)/E_\gamma^\circ$ for different β (=v/c of the fragment) and θ (direction of γ-ray emission and detection, with respect to the horizontal beam axis).

Angle θ		Eγ(θ)/Eγ°					
(deg.)	(rad.)	β = 0.39	β = 0.40	β = 0.41	β = 0.42	β = 0.43	β = 0.44
0	0.00	1.5731	1.5956	1.6187	1.6425	1.6670	1.6922
20	0.35	1.5147	1.5339	1.5536	1.5738	1.5944	1.6156
37	0.65	1.3937	1.4067	1.4200	1.4335	1.4471	1.4610
60	1.05	1.1920	1.1967	1.2013	1.2059	1.2104	1.2149
90	1.57	0.9596	0.9573	0.9550	0.9526	0.9502	0.9476
100	1.75	0.8987	0.8952	0.8916	0.8879	0.8842	0.8804
120	2.09	0.8030	0.7978	0.7926	0.7873	0.7820	0.7767
160	2.79	0.7022	0.6958	0.6894	0.6831	0.6767	0.6704

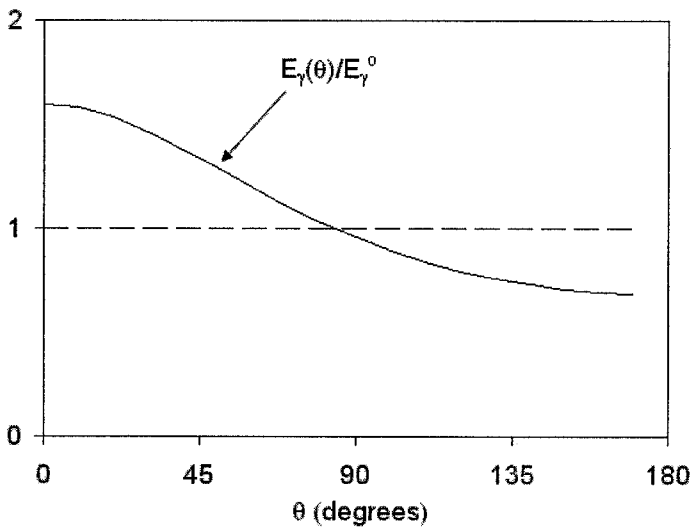

Figure C.1 Plot of $E_\gamma(\theta)/E_\gamma^\circ$ for β (=v/c of the fragment) equal to 0.40, and variable θ (direction of γ-ray emission and detection, with respect to the horizontal beam axis).

Table C.2 Energies and relative γ-ray intensities of transitions observed in ^{28}Ne produced by one-proton knockout from ^{29}Na in E03053. The energies and γ-ray intensities are measured separately in the 37°- and 90°-rings of SeGA, and then averaged out. The errors in the γ-ray energies in this table are statistical only.

^{28}Ne from ^{29}Na, 37°-ring

Doppler-corrected energy		Doppler-shifted energy	Lorentz-boosted abs. efficiency	Background-subtracted area		Peak intensity			Relative γ-ray intensity		
E_γ° (keV)	ΔE_γ° (keV)	$E_\gamma(37^\circ)$ (keV)	$\varepsilon_{37,\,2004}$	A_p	ΔA_p	I_p	ΔI_p	$\Delta I_p/I_p$	I_γ (%)	$\Delta I_\gamma/I_\gamma$	ΔI_γ (%)
897	3	1285.8	0.0226	77	28	3402	1237	0.36	8.8	0.37	3.2
1127.3	2.4	1615.9	0.0214	229	45	10689	2100	0.20	27.5	0.20	5.6
1307.8	0.8	1874.7	0.0211	820	45	38861	2133	0.05	100		
1712	3	2454.1	0.0214	155	24	7241	1121	0.15	18.6	0.16	3.1

^{28}Ne from ^{29}Na, 90°-ring

Doppler-corrected energy		Doppler-shifted energy	Lorentz-boosted abs. efficiency	Background-subtracted area		Peak intensity			Relative γ-ray intensity		
E_γ° (keV)	ΔE_γ° (keV)	$E_\gamma(90^\circ)$ (keV)	$\varepsilon_{90,\,2004}$	A_p	ΔA_p	I_p	ΔI_p	$\Delta I_p/I_p$	I_γ (%)	$\Delta I_\gamma/I_\gamma$	ΔI_γ (%)
889.4	1.4	847.3	0.0147	76	17	5162	1155	0.22	11.5	0.23	2.7
1124.9	2.4	1071.6	0.0130	84	23	6460	1769	0.27	14.4	0.28	4.1
1305.0	0.6	1243.2	0.0123	548	35	44715	2856	0.06	100		
1701.2	1.8	1620.6	0.0115	135	18	11774	1570	0.13	26.3	0.15	3.9

^{28}Ne from ^{29}Na, averaged 37°- and 90°-rings

Doppler-corrected energy			Peak intensity			Relative γ-ray intensity		
E_γ° (keV)	ΔE_γ° (keV)		I_p	ΔI_p	$\Delta I_p/I_p$	I_γ (%)	$\Delta I_\gamma/I_\gamma$	ΔI_γ (%)
891.4	1.6	Avg. I_{37} and I_{90}	4282	846	0.20	10.2	0.20	2.1
1127.0	1.8	Avg. I_{37} and I_{90}	8575	1373	0.16	20.5	0.17	3.4
1306.4	0.5	Avg. I_{37} and I_{90}	41788	1782	0.04	100		
1706.8	1.7	Avg. I_{37} and I_{90}	9508	965	0.10	22.8	0.11	2.5

Table C.3 Energies and relative γ-ray intensities of transitions observed in ^{28}Ne produced by two-proton knockout from ^{30}Mg in E03053. The energies and γ-ray intensities are measured separately in the 37°- and 90°-rings of SeGA, and then averaged out. The errors in the γ-ray energies in this table are statistical only.

^{28}Ne from ^{30}Mg, 37°-ring

Doppler-corrected energy		Doppler-shifted energy	Lorentz-boosted abs. efficiency	Background-subtracted area		Peak intensity			Relative γ-ray intensity		
E_γ° (keV)	ΔE_γ° (keV)	$E_\gamma(37^\circ)$ (keV)	$\varepsilon_{37,\,2004}$	A_p	ΔA_p	I_p	ΔI_p	$\Delta I_p/I_p$	I_γ (%)	$\Delta I_\gamma/I_\gamma$	ΔI_γ (%)
894	5	1294	0.0229	63	25	2751	1092	0.40	19.7	0.41	8.1
1116	7	1615	0.0217	44	27	2025	1243	0.61	14.5	0.62	9.1
1301.2	2.0	1883.0	0.0214	298	32	13932	1496	0.11	100		
1711	8	2476	0.0217	116	37	5338	1703	0.32	38	0.34	13

^{28}Ne from ^{30}Mg, 90°-ring

Doppler-corrected energy		Doppler-shifted energy	Lorentz-boosted abs. efficiency	Background-subtracted area		Peak intensity			Relative γ-ray intensity		
E_γ° (keV)	ΔE_γ° (keV)	$E_\gamma(90^\circ)$ (keV)	$\varepsilon_{90,\,2004}$	A_p	ΔA_p	I_p	ΔI_p	$\Delta I_p/I_p$	I_γ (%)	$\Delta I_\gamma/I_\gamma$	ΔI_γ (%)
894	4	849	0.0145	46	16	3162	1100	0.35	25.6	0.37	9.6
1115	5	1059	0.0129	18	12	1392	928	0.67	11.3	0.68	7.7
1307.2	1.7	1242.1	0.0121	150	21	12363	1731	0.14	100		
1701	4	1616	0.0114	104	17	9161	1497	0.16	74	0.22	16

^{28}Ne from ^{30}Mg, averaged 37°- and 90°-rings

Doppler-corrected energy			Peak intensity			Relative γ-ray intensity		
E_γ° (keV)	ΔE_γ° (keV)		I_p	ΔI_p	$\Delta I_p/I_p$	I_γ (%)	$\Delta I_\gamma/I_\gamma$	ΔI_γ (%)
895.0	3.0	Avg. I_{37} and I_{90}	2956	775	0.26	22	0.28	6.2
1117.0	6.0	Avg. I_{37} and I_{90}	1709	775	0.45	13	0.46	6.0
1304.2	1.4	Avg. I_{37} and I_{90}	13148	1144	0.09	100		
1704.0	4.0	Avg. I_{37} and I_{90}	7249	1134	0.16	55	0.18	10

Table C.4 Energies and relative γ-ray intensities of transitions observed in ^{29}Ne produced by knockout of ^{32}Mg in E03053 and E05122. The energies and γ-ray intensities are measured separately in the 37°- and 90°-rings of SeGA, and then averaged out. The errors in the γ-ray energies in this table are statistical only.

	Doppler-corrected energy		Doppler-shifted energy	Lorentz-boosted abs. efficiency	Background-subtracted area		Peak intensity	ΔI_p	$\Delta I_p/I_p$	Relative γ-ray intensity		
	E_γ° (keV)	ΔE_γ° (keV)	$E_\gamma(\theta)$ (keV)	$\varepsilon_{\theta,\,exp.}$	A_p	ΔA_p	I_p	ΔI_p	$\Delta I_p/I_p$	I_γ (%)	$\Delta I_\gamma/I_\gamma$	ΔI_γ (%)
^{29}Ne, 37°, β = 0.40	225	13	317	0.0616	8	4	130	65	0.50	31	0.62	19
(E03053)	626	7	881	0.0261	11	4	421	153	0.36	100		
^{29}Ne, 90°, β = 0.40	233	7	223	0.0473	5	3	106	63	0.60	40	1.00	40
(E03053)	636	19	609	0.0190	5	4	264	211	0.80	100		
	227	5	316	0.0442	24	8	543	181	0.33	36	0.39	14
^{29}Ne, 37°, β = 0.39	620.9	1.1	865.3	0.0287	43	9	1497	313	0.21	100		
(E05122)	928	4	1293	0.0223	14	4	629	180	0.29	42	0.35	15
	235	4	226	0.0292	19	13	651	446	0.68	39	0.74	29
^{29}Ne, 90°, β = 0.39	620.6	2.1	596	0.0166	28	8	1689	482	0.29	100		
(E05122)	914	14	877	0.0130	11	4	849	309	0.36	50	0.46	23
	234	4	Avg. I_{37} and I_{90}, E03053				118	45	0.39			
	230	4	Avg. I_{37} and I_{90}, E05122				597	241	0.40			
	629	6	Avg. I_{37} and I_{90}, E03053				342	130	0.38			
	620.8	1.0	Avg. I_{37} and I_{90}, E05122				1593	288	0.18			
Averaged results	932	4	Avg. I_{37} and I_{90}, E05122				739	179	0.24			
Final results	232	4	Summed E03053 and E05122 intensities				715	245	0.34	37	0.38	14
	621.6	1.0	Summed E03053 and E05122 intensities				1935	316	0.16	100		
^{29}Ne	931	3	E05122 intensity				739	179	0.24	38	0.29	11

Table C.5 Energies and relative γ-ray intensities of transitions observed in ^{30}Ne produced by two-proton knockout of ^{32}Mg in E03053 and E05122. The energies and γ-ray intensities are measured separately in the 37°- and 90°-rings of SeGA, and then averaged out. The errors in the γ-ray energies in this table are statistical only.

	Doppler-corrected energy		Doppler-shifted energy	Lorentz-boosted abs. efficiency	Background-subtracted area		Peak intensity			Relative γ-ray intensity		
	E_γ° (keV)	ΔE_γ° (keV)	$E_\gamma(\theta)$ (keV)	$\varepsilon_{\theta,\,exp.}$	A_p	ΔA_p	I_p	ΔI_p	$\Delta I_p/I_p$	I_γ (%)	$\Delta I_\gamma/I_\gamma$	ΔI_γ (%)
^{30}Ne, 37°, β = 0.40	794.6	2.0	1117.8	0.0232	23	7	992	302	0.304	100		
(E03053)	1438	14	2023	0.0205	6	3	293	146	0.500	30	0.6	17
^{30}Ne, 90°, β = 0.40	796	5	762	0.015615	7	4	448	256	0.571	100		
(E03053)	1424	12	1363	0.012004	2.8	2.4	233	200	0.857	52	1.0	54
^{30}Ne, 37°, β = 0.40	787	3	1107.1	0.020397	33	9	1618	441	0.273	100		
(E05122)	1437	6	2021.5	0.015376	11	3	715	195	0.273	44	0.4	17
^{30}Ne, 90°, β = 0.40	794	3	760	0.014394	20	7	1389	486	0.350	100		
(E05122)	1450	14	1388	0.010213	5	3	490	294	0.600	35	0.7	24
	791.6	1.5	Avg. I_{37} and I_{90}, E03053				720	198				
	791.6	1.5	Avg. I_{37} and I_{90}, E05122				1504	328				
Averaged	1443	7	Avg. I_{37} and I_{90}, E03053				263	124				
results	1443	7	Avg. I_{37} and I_{90}, E05122				602	176				
Final results	791.6	1.5	Summed E03053 and E05122 intensities				2224	383	0.172	100		
^{30}Ne	1443	7	Summed E03053 and E05122 intensities				865	215	0.249	39	0.3	12

Bibliography

[Ale78] T. K. Alexander and J. S. Forster, Lifetime measurements of excited nuclear levels by Doppler-shift methods, In: *Advances in Nuclear Physics, Vol. 10*, Eds: M. Baranger and E. Vogt, 197-331 (1978)

[Aza02a] F. Azaiez *et al.*, Structure of neutron-rich nuclei around N=20,28 and 40 from in-beam γ-spectroscopy, Nucl. Phys. A **704**, 37c-49c, (2002)

[Aza02b] F. Azaiez *et al.*, Probing shell structure in neutron-rich nuclei with in-beam γ-spectroscopy, Eur. Phys. J. A **15**, 93-97 (2002)

[Baz02] D. Bazin *et al.*, The program LISE: a simulation of fragment separators, Nucl. Instrum. Methods Phys. Res. A **482**, 307-327 (2002)

[Baz03a] D. Bazin *et al.*, The S800 spectrograph, Nucl. Instrum. Methods Phys. Res. B **204**, 629-633 (2003)

[Baz03b] D. Bazin *et al.*, New direct reaction: two-proton knockout from neutron-rich nuclei, Phys. Rev. Lett. **91**, 012501 (2003)

[Baz04] D. Bazin *et al.*, Two-proton knockout on neutron-rich nuclei, Nucl. Phys. A **746**, 173c-177c (2004)

[Bel00] M. Belleguic *et al.*, In-beam gamma spectroscopy of very neutron-rich nuclei at GANIL, Phys. Scripta T **88**, 122-126 (2000)

[Bel05] M. Belleguic *et al.*, Search for neutron excitations across the N=20 shell gap in $^{25\text{-}29}$Ne, Phys. Rev. C **72**, 054316 (2005)

[Boh75] A. Bohr and B. R. Mottelson, *Nuclear Structure*, Advanced Book Program, W. A. Benjamin, Inc. (1975)

[Boh36] N. Bohr, Neutron capture and nuclear constitution, Nature (London) **137**, 344-351 (1936)

[Bro88] B. A. Brown *et al.*, OXBASH, MSU Cyclotron Laboratory, Report No. **524** (1988)

[Bro01] B. A. Brown, The nuclear shell model towards the drip lines, Prog. Part. Nucl. Phys. **47**, 517-599 (2001)

[Bro02] B. A. Brown *et al.*, Absolute spectroscopic factors from nuclear knockout reactions, Phys. Rev. C **65**, 061601(R) (2002)

[Bro07a] B. A. Brown, http://www.nscl.msu.edu/~brown/resources/SDE.HTM (2007)

[Bro07b] B. A. Brown, private communication (2007)

[Cas90] B. Castel and I. S. Towner, *Modern theories of nuclear moments*, Clarendon Press, Oxford (1990)

[Cas00a] R. F. Casten, *Nuclear structure from a simple perspective*, Oxford University Press, 2nd ed. (2000)

[Cas00b] R. F. Casten, The study of exotic nuclei, Prog. Part. Nuclear Phys. **45**, S171-S233 (2000)

[Din05] D.-C. Dinca, *Study of the development of shell closures at N = 32, 34 and approaches to sub-segment interaction-point determination in 32-fold segmented high-purity germanium detectors*, PhD Thesis, Michigan State University (2005)

[Dom06a] Zs. Dombrádi *et al.*, Vanishing N=20 shell gap: study of excited states in ^{27,28}Ne, Phys. Rev. Lett. **96**, 182501 (2006)

[Dom06b] Zs. Dombrádi *et al.*, Evolution of the N=20 shell gap, J. Phys: Conf. Ser. **49**, 140-145 (2006)

[Eji89] H. Ejiri and M.J.A. de Voigt, *Gamma-ray and electron spectroscopy in nuclear physics*, Oxford Science Publications, Clarendon Press, Oxford (1989)

[ENS07] ENSDF, Evaluated Nuclear Structure Data File (May 21, 2007) http://www.nndc.bnl.gov/ensdf/

[Fed77] P. Federman and S. Pittel, Towards a unified microscopic description of nuclear deformation, Phys. Lett. B **69** (4), 385-388 (1977)

[Fed79] P. Federman and S. Pittel, Unified shell-model description of nuclear deformation, Phys. Rev. C **20** (2), 820-829 (1979)

[Fir96] R. B. Firestone and V. S. Shirley, *Table of Isotopes*, 8th ed., John Wiley & Sons, Inc. (1996)

[Fuk92] N. Fukunishi *et al.*, Vanishing of the shell gap in N=20 neutron-rich nuclei, Phys. Lett. B **296**, 279-284 (1992)

[Gad04a] A. Gade *et al.*, Reduced occupancy of the deeply bound $0d_{5/2}$ neutron state in ^{32}Ar, Phys. Rev. Lett. **93** (4), 042501 (2004)

[Gad04b] A. Gade *et al.*, One-neutron knockout on proton-rich nuclei with N=16, Phys. Rev. C **69**, 034311 (2004)

[Gad05] A. Gade *et al.*, Spectroscopic factors in exotic nuclei from nucleon-knockout reactions, Eur. Phys. J. A **25**, s01, 251-253 (2005)

[Gai91] J.-J. Gaimard and K.-H. Schmidt, A reexamination of the abrasion-ablation model for the description of the nuclear fragmentation reaction, Nucl. Phys. A **531**, 709-745 (1991)

[Gla98] T. Glasmacher, Coulomb excitation at intermediate energies, Annu. Rev. Nucl. Part. Sci. **48**, 1-31 (1998)

[Gui02] D. Guillemaud-Mueller *et al.*, Spectroscopy of nuclei far from stability at GANIL: recent experiments, Eur. Phys. J. A **13**, 63-67 (2002)

[Han95] P. G. Hansen *et al.*, Nuclear halos, Annu. Rev. Nucl. Part. Sci. **45**, 591-634 (1995)

[Han03] P. G. Hansen and J. A. Tostevin, Direct reactions with exotic nuclei, Annu. Rev. Nucl. Part. Sci. **53**, 219-261 (2003)

[Har74] B. G. Harvey, The cyclotron, In: *Nuclear spectroscopy and reactions, Part A,* Ed: J. Cerny, Academic Press, 35-77 (1974)

[Hax49] O. Haxel, J. H. D. Jensen, and H. E. Suess, On the "magic numbers" in nuclear structure, Phys. Rev. **75**, 1766-1766 (1949)

[Hu02] Z. Hu *et al.*, An automatic energy-calibration method for segmented germanium detectors, Nucl. Instrum. Methods Phys.Res. A **482**, 715-719 (2002)

[Hüf75] J. Hüfner *et al.*, Abrasion-ablation in reactions between relativistic heavy ions, Phys. Rev. C **12**(6), 1888-1898 (1975)

[Hyp05] http://hyperphysics.phy-astr.gsu.edu/hbase/magnetic/cyclot.html (2005)

[Iwa05] H. Iwasaki *et al.*, Quadrupole collectivity of ^{28}Ne and the boundary of the island of inversion, Phys. Lett. B **620**, 118-124 (2005)

[Jan05] R. V. F. Janssens, Elusive magic numbers, Nature (London) **435**, 897-898 (2005)

[Kno00] G. F. Knoll, *Radiation Detection and Measurement*, John Willey & Sons, Inc., 3rd edition (2000)

[Kra88] K. S. Krane, *Introductory Nuclear Physics*, John Wiley & Sons, Inc. (1988)

[Law32] E. O. Lawrence and M. S. Livingston, The production of high speed light ions without the use of high voltages, Phys. Rev. **40**, 19-37 (1932)

[Lee03] I.-Y. Lee *et al.*, Developments in large gamma-ray detector arrays, Rep. Prog. Phys. **66**, 1095-1144 (2003)

[Mad01] V. Maddalena *et al.*, Single-neutron knockout reactions: application to the spectroscopy of ^{16,17,19}C, Phys. Rev. C **63**, 024613 (2001)

[Mar69] P. Marmier and E. Sheldon, *Physics of nuclei and particles*, Academic Press (1969)

[May49] M. G. Mayer, On closed shells in nuclei II, Phys. Rev. **75**, 1969-1970 (1949)

[May55] M. G. Mayer and J. H. D. Jensen, *Elementary theory of nuclear shell structure*, John Wiley & Sons, Inc. (1955)

[Mil02] K. L. Miller *et al.*, Automated determination of segment positions in a high-purity 32-fold segmented germanium detector, Nucl. Instrum. Methods Phys. Res. A **490**, 140-145 (2002)

[Mit02] W. Mittig *et al.*, Shape coexistence and the N=20 shell closure far from stability by inelastic scattering, Eur. Phys. J. A **15**, 157-160 (2002)

[Mor76] H. Morinaga and T. Yamazaki, *In-beam gamma-ray spectroscopy*, North-Holland Publishing Company (1976)

[Mor97] D. J. Morrissey, A new high-resolution separator for high-intensity secondary beams, Nucl. Instrum. Methods Phys. Res. B **126**, 316-319 (1997)

[Mor98] D. J. Morrissey and B. M. Sherrill, Radioactive nuclear beam facilities based on projectile fragmentation, Phil. Trans. R. Soc. A **356**, 1985-2006 (1998)

[Mor03] D. J. Morrissey *et al.*, Commissioning of the A1900 projectile fragment separator, Nucl. Instrum. Methods Phys. Res. B **204**, 90-96 (2003)

[Mot95] T. Motobayashi *et al.*, Large deformation of the very neutron-rich nucleus ^{32}Mg from intermediate-energy Coulomb excitation, Phys. Lett. B **346**, 9-14 (1995)

[MSU07] Michigan State University, NSCL, http://www.nscl.msu.edu (2007)

[Mue01] W. F. Mueller *et al.*, Thirty-two-fold segmented germanium detectors to identify γ-rays from intermediate-energy exotic beams, Nucl. Instrum. Methods Phys. Res. A **466**, 492-498 (2001)

[Nav98] A. Navin *et al.*, Spectroscopy of radioactive beams from single-nucleon knockout reactions: application to the *sd* shell nuclei ^{25}Al and ^{26,27,28}P, Phys. Rev. Lett. **81** (23), 5089-5092 (1998)

[Nav05] C. R. Nave, *HyperPhysics*, Georgia State University (2005). The cyclotron principle: http://hyperphysics.phy-astr.gsu.edu/hbase/magnetic/cyclot.html

[Ney03] G. Neyens, Nuclear magnetic and quadrupole moments for nuclear structure research on exotic nuclei, Rep. Prog. Phys. **66**, 633-689 (2003)

[Ney05] G. Neyens *et al.*, Measurement of the spin and magnetic moment of ^{31}Mg: evidence for a strongly deformed intruder ground state, Phys. Rev. Lett. **94**, 022501 (2005)

[Obe06] A. Obertelli *et al.*, Shell gap reduction in neutron-rich N=17 nuclei, Phys. Lett. B **633**, 33-37 (2006)

[Ots01a] T. Otsuka *et al.*, Magic numbers in exotic nuclei and spin-isospin properties of the NN interaction, Phys. Rev. Lett. **87** (8), 082502 (2001)

[Ots01b] T. Otsuka *et al.*, Monte Carlo shell model for atomic nuclei, Prog. Part. Nucl. Phys. **47**, 319-400 (2001)

[Ots04] T. Otsuka, Shell model results for exotic nuclei, Eur. Phys. J. A **20**, 69-73 (2004)

[Oza00] A. Ozawa *et al.*, New magic number, N=16, near the neutron drip line, Phys. Rev. Lett. **84** (24), 5493-5495 (2000)

[Pat91] S. K. Patra and C. R. Praharaj, Relativistic mean field study of "island of inversion" in neutron-rich Ne, Na, Mg nuclei, Phys. Lett. B **273**, 13-19 (1991)

[Pod06] Zs. Podoloyák *et al.*, High angular momentum states populated in fragmentation reactions, Phys. Lett. B **632**, 203-206 (2006)

[Pov87] A. Poves and J. Retamosa, The onset of deformation at the N=20 neutron shell closure far from stability, Phys. Lett. B **184** (4), 311-315 (1987)

[Pov94] A. Poves and J. Retamosa, Theoretical study of the very neutron-rich nuclei around N=20, Nucl. Phys. A **571**, 221-241 (1994)

[Pri99] B. V. Pritychenko *et al.*, Role of intruder configurations in ^{26,28}Ne and ^{30,32}Mg, Phys. Lett. B **461**, 322-328 (1999)

[Rad07] D. Radford, RadWare γ-ray spectroscopy data analysis software: gf3, http://radware.phy.ornl.gov/gf3/gf3.html (2007)

[Ree99] A. T. Reed *et al.*, Radioactivity of neutron-rich oxygen, fluorine, and neon isotopes, Phys. Rev. C **60**, 024311 (1999)

[Rod03] R. R. Rodriguez-Guzman *et al.*, Quadrupole collectivity of neutron-rich neon isotopes, Eur. Phys. J. A **17**, 37-47 (2003)

[Rut11] E. Rutherford, The scattering of alpha and beta particles by matter and the structure of the atom, Philos. Mag. **21**, 669-688 (1911)

[Sag04] H. Sagawa *et al.*, Deformations and electromagnetic moments in carbon and neon isotopes, Phys. Rev. C **70**, 054316 (2004)

[Sag05] H. Sagawa *et al.*, Deformations and electromagnetic moments of light exotic nuclei, Eur. Phys. J. A **25**, s01, 535-538 (2005)

[Sat83] G. R. Satchler, *Direct nuclear reactions*, Oxford University Press (1983)

[Sat90] G. R. Satchler, *Introduction to nuclear reactions*, Macmillan Education Ltd., 2nd ed. (1990)

[Sau00] E. Sauvan *et al.*, One-neutron removal reactions on neutron-rich psd-shell nuclei, Phys. Lett. B **491**, 1-7 (2000)

[Soh02] D. Sohler *et al.*, Shape evolution in heavy sulfur isotopes and erosion of the N=28 shell closure, Phys. Rev. C **66**, 054302 (2002)

[Spe07] SpecTcl nuclear data analysis software: http://docs.nscl.msu.edu/daq/spectcl/ (2007)

[Süm00] K. Sümmerer and B. Blank, Modified empirical parametrization of fragmentation cross sections, Phys. Rev. C **61**, 034607 (2000)

[Sym79] T. J. M. Symons *et al.*, Observation of new neutron-rich isotopes by fragmentation of 205-MeV/nucleon ^{40}Ar ions, Phys. Rev. Lett. **42**(1), 40-43 (1979)

[Tan85] I. Tanihata *et al.*, Measurements of interaction cross sections and nuclear radii in the light p-shell region, Phys. Rev. Lett. **55**, 2676-2679 (1985)

[Tar04] O. B. Tarasov and D. Bazin, LISE++: design your own spectrometer, Nucl. Phys. A **746**, 411c-414c (2004)

[Tar07] O. B. Tarasov and D. Bazin, the LISE code download page: http://groups.nscl.msu.edu/lise (2007)

[Ter04] J. R. Terry and J. L. Lecouey, Nuclear structure studies in the neutron-rich A=30 mass region by direct nucleon removal reactions, Nucl. Phys. A **734**, 469-472 (2004)

[Ter06a] J. R. Terry *et al.*, Direct evidence for the onset of intruder configurations in neutron-rich Ne isotopes, Phys. Lett. B **640**, 86-90 (2006)

[Ter06b] J. R. Terry, *Probing single-particle structure near the island of inversion by direct neutron knockout from intermediate-energy beams of* ^{26,28}*Ne and* ^{30,32}*Mg*, PhD Thesis, Michigan State University (2006)

[Thi75] C. Thibault *et al.*, Direct measurement of the masses of ^{11}Li and $^{26\text{-}32}$Na with an on-line mass spectrometer, Phys. Rev. C **12**, 644 (1975)

[Tho03] M. Thoennessen *et al.*, Single proton knock-out reactions from ^{24,25,26}F, Phys. Rev. C **68**, 044318 (2003)

[Tos99] J. A. Tostevin, Core excitation in halo nucleus break-up, J. Phys. G **25**, 735-739 (1999)

[Tos01] J. A. Tostevin, Single-nucleon knockout reactions at fragmentation beam energies, Nucl. Phys. A **682**, 320c-331c (2001)

[Tos04a] J. A. Tostevin *et al.*, Direct reaction spectroscopy of exotic nuclei, Nucl. Phys. A **746**, 166c-172c (2004)

[Tos04b] J. A. Tostevin *et al.*, Correlated two-nucleon stripping reactions, Phys. Rev. C **70**, 064602 (2004)

[Tos06a] J. A. Tostevin, Probing the shell model using nucleon knockout reactions, J. Phys.: Conf. Ser. **49**, 21-26 (2006)

[Tos06b] J. A. Tostevin and B. A. Brown, Diffraction dissociation contributions to two-nucleon knockout reactions and the suppression of shell-model strength, Phys. Rev. C **74**, 064604 (2006)

[Tos07] J. A. Tostevin, private communication (2007)

[Tri05] V. Tripathi *et al.*, ^{29}Na: defining the edge of the island of inversion for Z=11, Phys. Rev. Lett. **94**, 162501 (2005)

[Uts99] Y. Utsuno *et al.*, Varying shell gap and deformation in N~20 unstable nuclei studied by the Monte Carlo shell model, Phys. Rev. C **60**, 054315 (1999)

[Uts01] Y. Utsuno *et al.*, Extreme location of F drip line and disappearance of the N=20 magic structure, Phys. Rev. C **64**, 011301 (R) (2001)

[Uts05] Y. Utsuno *et al.*, Shape coexistence and mixing in the N~20 region, J. Phys.: Conf. Ser. **20**, 167-168 (2005)

[Uts07] Y. Utsuno, private communication (2007)

[War90] E. K. Warburton *et al.*, Mass systematics for A=29-44 nuclei: the deformed A~32 region, Phys. Rev. C **41**(3), 1147-1166 (1990)

[War03] D. Warner, It's a knockout, Nature (London) **425**, 570-571 (2003)

[War04] D. Warner, Not-so-magic numbers, Nature (London) **430**, 517-518 (2004)

[Wat81] A. Watt *et al.*, A shell-model investigation of the binding energies of some exotic isotopes of sodium and magnesium, J. Phys. G: Nucl. Phys. **7**, L145-L148 (1981)

[Wes76] G. D. Westfall *et al.*, Nuclear fireball model for proton inclusive spectra from relativistic heavy-ion collisions, Phys. Rev. Lett. **37** (18), 1202-1205 (1976)

[Wil80] B. H. Wildenthal and W. Chung, Collapse of the conventional shell-model ordering in the very-neutron-rich isotopes of Na and Mg, Phys. Rev. C **22**(5), 2260-2262 (1980)

[Wil84] B. H. Wildenthal, Empirical strengths of spin operators in nuclei, Prog. Part. Nucl. Phys. **11**, 5-51 (1984)

[Yam04] M. Yamagami and Nguyen Van Giai, Pairing effects on the collectivity of quadrupole states around ^{32}Mg, Phys. Rev. C **69**, 034301 (2004)

[Yan03] Y. Yanagisawa *et al.*, The first excited state of ^{30}Ne studied by proton inelastic scattering in reversed kinematics, Phys. Lett. B **566**, 84-89 (2003)

[Yan04] Y. Yanagisawa *et al.*, The first excited state of ^{30}Ne studied by proton inelastic scattering in reversed kinematics, Nucl. Phys. A **734**, 374-377 (2004)

[Yon01] K. Yoneda *et al.*, Deformation of ^{34}Mg studied via in-beam γ-ray spectroscopy using radioactive-ion projectile fragmentation, Phys. Lett. B **499**, 233-237 (2001)

[Yon06] K. Yoneda *et al.*, Two-neutron knockout from neutron-deficient ^{34}Ar, ^{30}S, and ^{26}Si, Phys. Rev. C **74**, 021303(R) (2006)

[Yur99] J. Yurkon et al., Focal plane detector for the S800 high-resolution spectrometer, Nucl. Instrum. Methods Phys. Res. A 422, 291 (1999)